

NAVIER-STOKES PREDICTION OF THE THREE DIMENSIONAL FLOWFIELD
OF
JETS IN A CROSSFLOW USING THE FINITE ELEMENT METHOD

by

Tae Shik Oh

Dissertation submitted to the Faculty of the
Virginia Polytechnic Institute and State University
in partial fulfillment of the requirements for the degree of

DOCTOR OF PHILOSOPHY

in

Aerospace Engineering

APPROVED:

J. A. Schetz, Chairman

B. Grossman

A. K. Jakubowski

W. L. Neu

J. N. Reddy

March, 1988

Blacksburg, Virginia

**NAVIER-STOKES PREDICTION OF THE THREE DIMENSIONAL FLOWFIELD
OF
JETS IN A CROSSFLOW USING THE FINITE ELEMENT METHOD**

by

Tae Shik Oh

J. A. Schetz, Chairman

Aerospace Engineering

(ABSTRACT)

A Prandtl-type eddy viscosity model including the first-order effect of turbulence structure has been developed to deal with curved free-shear flows. The model is generalized to account for the effect of arbitrary cross-section of the jets injected from a various nozzle configurations into a uniform crossflow. The model is implemented as a module of a general purpose finite-element computer code. The finite-element procedures used here follow from a Galerkin type variational formulation with the penalty approximation for pressure in a consistent manner, with which a significant savings in computational time and storage are achieved. In order to simulate complicated 3-D turbulent flow with a restricted computational space and modest mesh, a slip condition is employed to model the wall flow and stress-free conditions are used for the farfield and outflow boundaries. Numerical predictions are performed for three problems: a single circular jet in a crossflow, a single streamwise aligned rectangular (aspect ratio 4) jet in a crossflow, and dual side-by-side rectangular jets in a crossflow, all at a jet-to-crossflow velocity ratio 4, which is important for V/STOL and other applications. The prediction of the mean velocity components of the circular jet case is in excellent agreement with the measured data except for the near wall region. The surface pressure comparison is very good except for the viscous wake region right behind

the nozzle due to flow separation. The current pressure prediction is as good as any inviscid solution given by singularity or panel method with empirically tuned jet properties. No mean flowfield comparison is made for the single rectangular jet case due to the lack of available measured data. Surface pressure comparison is consistently very good, especially for the region near the front corners of the nozzle where the large negative peaks appear. The agreement for this case seems to be even better than the circular jet case, and the reason is, as observed in the surface velocity vector plot, the different vortex structure and mixing in the vicinity of the nozzle. For the dual jets case, the surface pressure prediction is still in a very good agreement, and the mean velocity comparison shows better agreement as the mesh is refined. The flowfield is found to be more complicated than the circular jet case due to the jet interaction, and further mesh refinement is needed for the complete resolution of the jet/wake flowfield. However, if the surface pressure prediction is the major concern, as in the V/STOL applications, the current size of computational space along with numerical strategies adopted here can serve that purpose effectively. Finally, the mean velocity and the pressure prediction obtained here for rectangular jet(s) are the first known to this author, and will provide useful information for the 3-D, complex, turbulent, free shear flow computations.

ACKNOWLEDGEMENTS

The author wishes to express his deep gratitude to Dr. Schetz who, as the chairman of the advisory committee, directed and fully supported this research work. It would be a difficult task without his encouragement and guidance to complete this study. To be with him always enlightened the author not only on the academic aspects but the life in general.

Dr. J.N. Reddy is thanked for stimulating the author's interests in the variational method and the finite element method, and also for many helpful suggestions throughout the course of this work.

Dr. B. Grossman is thanked for his comprehensive guidance in the high speed aerodynamics and computational fluid dynamics, and also for the careful review on this dissertation.

The other members of the advisory committee, Dr. A.K. Jakubowski and W.L. Neu are thanked for their continued interest and constructive comments on this work.

Thanks are due to the Virginia Tech Computing Center for their timely update of the system and for arranging very large out-of-core storage.

Special thanks go to Dr. M.S. Engelman in Fluid Dynamics International for helpful discussions on the computational matters.

In addition, all graduate students in AOE department are thanked for their friendship, and the secretaries in this department are thanked for their help in administrative matters.

Finally, the author would like to express his gratitude to his family for moral support, especially to his wife, Kyung-Jai.

Table of Contents

INTRODUCTION	1
1.1 GENERAL	1
1.2 PHYSICAL ASPECTS OF THE FLOW	3
1.3 HIERACHY OF THE ANALYTICAL MODELS	5
1.4 CURRENT ISSUES OF RESEARCHII	11
1.5 FEM IN TURBULENT FLOWS	12
1.6 OBJECTIVES OF THIS WORK	14
TURBULENCE MODEL	16
2.1 BACKGROUND	16
2.2 EDDY VISCOSITY MODEL FOR A CURVED, 3-D JET	17
2.2.1 CHARACTERISTIC SHEAR LAYER WIDTH	18
2.2.2 POTENTIAL CORE CORRECTION	21
2.2.3 MODEL FORM	22
2.2.4 PROPORTIONALITY CONSTANT	23
FINITE ELEMENT PROCEDURES	26

3.1 OVERVIEW	26
3.2 GOVERNING EQUATIONS	29
3.3 VARIATIONAL FORMULATION	30
3.4 MIXED FINITE ELEMENT METHOD	32
3.5 PENALTY FUNCTION FINITE ELEMENT METHODS	35
3.5.1 REDUCED INTEGRATION PENALTY (RIP) METHOD	35
3.5.2 CONSISTENT PENALTY METHOD	38
3.6 APPROXIMATION FUNCTIONS	39
COMPUTATIONAL DETAILS	41
4.1 NONDIMENSIONALIZATION	41
4.2 COMPUTATION DOMAIN AND MESH DISTRIBUTION	42
4.3 BOUNDARY CONDITIONS	44
4.4 SOLUTION STRATEGY	46
RESULTS AND DISCUSSION	50
5.1 PRESENTAION OF RESULTS	50
5.2 SINGLE CIRCULAR JET IN A CROSSFLOW AT $R=4$	51
5.3 SINGLE RECTANGULAR JET IN A CROSSFLOW AT $R=4$	54
5.4 DUAL RECTANGULAR JETS IN A CROSSFLOW AT $R=4$	55
CONCLUSIONS AND SUGGESTIONS	59
6.1 SUMMARY OF CONCLUSIONS	59
6.2 SUGGESTIONS FOR FUTURE WORK	62
REFERENCES	64
FIGURES	71

VITA 165

List of Illustrations

Figure 1. Description of the Flowfield (Ref. 2)	72
Figure 2. Definition Sketch of a Circular Jet in a Crossflow for Analysis	73
Figure 3. Length of Potential Core (Ref. 6)	74
Figure 4. Turbulent Intensity along the Transverse jet (Ref. 7)	75
Figure 5. Single circular Jet in a Crossflow at $R = 4$: Finite Element Mesh vs. Surface Pressure Tap Locations	76
Figure 6. Single Circular Jet in a Crossflow at $R = 4$: Comparison of Jet Trajectory	77
Figure 7. Single Circular Jet in a Crossflow at $R = 4$: Comparison of Vortex Curve	78
Figure 8. Single Circular Jet in a Crossflow at $R = 4$: Comparison of Jet Shape ..	79
Figure 9. Single Circular Jet in a Crossflow at $R = 4$: Comparison of Axial Velocity Decay	80
Figure 10. Single Circular Jet in a Crossflow at $R = 4$: Variation of Averaged Half-Width along the Jet Axis	81
Figure 11. Single Circular Jet in a Crossflow at $R = 4$: Variation of Eddy Viscosity along the Jet Axis	82
Figure 12. Single Circular Jet in a Crossflow at $R = 4$: Comparison of Surface Pressure Coefficient	83
Figure 13. Single Circular Jet in a Crossflow at $R = 4$: Comparison of Velocity Vector Plots on the Plane of Symmetry ($y/D = 0.0$)	84
Figure 14. Single Circular Jet in a Crossflow at $R = 4$: Comparison of Streamwise Velocity Profiles at $x/D = 0.5$ and $y/D = 0.0$	85
Figure 15. Single Circular Jet in a Crossflow at $R = 4$: Comparison of Streamwise Velocity Profiles at $x/D = 1.0$ and $y/D = 0.0$	86

Figure 16. Single Circular Jet in a Crossflow at $R = 4$: Comparison of Streamwise Velocity Profiles at $x/D = 2.0$ and $y/D = 0.0$	87
Figure 17. Single Circular Jet in a Crossflow at $R = 4$: Comparison of Streamwise Velocity Profiles at $x/D = 3.0$ and $y/D = 0.0$	88
Figure 18. Single Circular Jet in a Crossflow at $R = 4$: Comparison of Streamwise Velocity Profiles at $x/D = 4.0$ and $y/D = 0.0$	89
Figure 19. Single Circular Jet in a Crossflow at $R = 4$: Comparison of Streamwise Velocity Profiles at $x/D = 5.0$ and $y/D = 0.0$	90
Figure 20. Single Circular Jet in a Crossflow at $R = 4$: Comparison of Normal Velocity Profiles at $x/D = 0.5$ and $y/D = 0.0$	91
Figure 21. Single Circular Jet in a Crossflow at $R = 4$: Comparison of Normal Velocity Profiles at $x/D = 1.0$ and $y/D = 0.0$	92
Figure 22. Single Circular Jet in a Crossflow at $R = 4$: Comparison of Normal Velocity Profiles at $x/D = 2.0$ and $y/D = 0.0$	93
Figure 23. Single Circular Jet in a Crossflow at $R = 4$: Comparison of Normal Velocity Profiles at $x/D = 3.0$ and $y/D = 0.0$	94
Figure 24. Single Circular Jet in a Crossflow at $R = 4$: Comparison of Normal Velocity Profiles at $x/D = 4.0$ and $y/D = 0.0$	95
Figure 25. Single Circular Jet in a Crossflow at $R = 4$: Comparison of Normal Velocity Profiles at $x/D = 5.0$ and $y/D = 0.0$	96
Figure 26. Single Circular Jet in a Crossflow at $R = 4$: Comparison of Velocity Vector Plots on the Crossflow Plane ($x/D = 0.0$)	97
Figure 27. Single Circular Jet in a Crossflow at $R = 4$: Comparison of Transverse Velocity Profiles at $x/D = 1.0$ and $y/D = 0.5$	98
Figure 28. Single Circular Jet in a Crossflow at $R = 4$: Comparison of Transverse Velocity Profiles at $x/D = 1.0$ and $y/D = 1.0$	99
Figure 29. Single Circular Jet in a Crossflow at $R = 4$: Comparison of Normal Velocity Profiles at $x/D = 1.0$ and $y/D = 0.5$	100
Figure 30. Single Circular Jet in a Crossflow at $R = 4$: Comparison of Normal Velocity Profiles at $x/D = 1.0$ and $y/D = 1.0$	101
Figure 31. Single Circular Jet in a Crossflow at $R = 4$: Display of Velocity Vectors on the Plane $z/D = 0.0, 0.25, 0.5, 1.0$ from above	102
Figure 32. Single Circular Jet in a Crossflow at $R = 4$: Display of Velocity Vectors on the Plane $z/D = 1.5, 2.0, 2.5, 3.0$ from above	103

Figure 33. Single Rectangular Jet in a Crossflow at $R = 4$: Finite Element Mesh vs. Surface Pressure Tap Locations	104
Figure 34. Single Rectangular Jet in a Crossflow at $R = 4$: Comparison of Surface Pressure coefficient	105
Figure 35. Single Rectangular Jet in a Crossflow at $R = 4$: Display of Velocity Vectors on the Plane $z/D = 0.0, 0.25, 0.5$ from above	106
Figure 36. Single Rectangular Jet in a Crossflow at $R = 4$: Display of Velocity Vectors on the Plane $z/D = 1.0, 2.0, 3.0$ from above	107
Figure 37. Dual Rectangular Jets in a Crossflow at $R = 4$: Finite Element Mesh vs. Surface Pressure Tap Locations	108
Figure 38. Dual Rectangular Jets in a Crossflow at $R = 4$: Comparison of Jet Trajectory	109
Figure 39. Dual Rectangular Jets in a Crossflow at $R = 4$: Comparison of Axial Velocity Decay	110
Figure 40. Dual Rectangular Jets in a Crossflow at $R = 4$: Comparison of Surface Pressure coefficient	111
Figure 41. Dual Rectangular Jets in a Crossflow at $R = 4$: Comparison of Velocity Vector Plots on the Plane of Nozzle Symmetry ($y/D = 0.0$)	113
Figure 42. Dual Rectangular Jets in a Crossflow at $R = 4$: Comparison of Streamwise Velocity Profiles at $x/D = 1.0$ and $y/D = 0.0$	114
Figure 43. Dual Rectangular Jets in a Crossflow at $R = 4$: Comparison of Streamwise Velocity Profiles at $x/D = 2.0$ and $y/D = 0.0$	115
Figure 44. Dual Rectangular Jets in a Crossflow at $R = 4$: Comparison of Streamwise Velocity Profiles at $x/D = 3.0$ and $y/D = 0.0$	116
Figure 45. Dual Rectangular Jets in a Crossflow at $R = 4$: Comparison of Streamwise Velocity Profiles at $x/D = 4.0$ and $y/D = 0.0$	117
Figure 46. Dual Rectangular Jets in a Crossflow at $R = 4$: Comparison of Streamwise Velocity Profiles at $x/D = 5.0$ and $y/D = 0.0$	118
Figure 47. Dual Rectangular Jets in a Crossflow at $R = 4$: Comparison of Normal Velocity Profiles at $x/D = 1.0$ and $y/D = 0.0$	119
Figure 48. Dual Rectangular Jets in a Crossflow at $R = 4$: Comparison of Normal Velocity Profiles at $x/D = 2.0$ and $y/D = 0.0$	120
Figure 49. Dual Rectangular Jets in a Crossflow at $R = 4$: Comparison of Normal Velocity Profiles at $x/D = 3.0$ and $y/D = 0.0$	121

Figure 50. Dual Rectangular Jets in a Crossflow at $R=4$: Comparison of Normal Velocity Profiles at $x/D=4.0$ and $y/D=0.0$	122
Figure 51. Dual Rectangular Jets in a Crossflow at $R=4$: Comparison of Normal Velocity Profiles at $x/D=5.0$ and $y/D=0.0$	123
Figure 52. Dual Rectangular Jets in a Crossflow at $R=4$: Comparison of Velocity Vector Plots on the Plane of Flow Symmetry ($y/D=-1.0$)	124
Figure 53. Dual Rectangular Jets in a Crossflow at $R=4$: Comparison of Streamwise Velocity Profiles at $x/D=-1.0$ and $y/D=-1.0$	125
Figure 54. Dual Rectangular Jets in a Crossflow at $R=4$: Comparison of Streamwise Velocity Profiles at $x/D=0.0$ and $y/D=-1.0$	126
Figure 55. Dual Rectangular Jets in a Crossflow at $R=4$: Comparison of Streamwise Velocity Profiles at $x/D=1.0$ and $y/D=-1.0$	127
Figure 56. Dual Rectangular Jets in a Crossflow at $R=4$: Comparison of Streamwise Velocity Profiles at $x/D=2.0$ and $y/D=-1.0$	128
Figure 57. Dual Rectangular Jets in a Crossflow at $R=4$: Comparison of Streamwise Velocity Profiles at $x/D=3.0$ and $y/D=-1.0$	129
Figure 58. Dual Rectangular Jets in a Crossflow at $R=4$: Comparison of Streamwise Velocity Profiles at $x/D=4.0$ and $y/D=-1.0$	130
Figure 59. Dual Rectangular Jets in a Crossflow at $R=4$: Comparison of Normal Velocity Profiles at $x/D=-1.0$ and $y/D=-1.0$	131
Figure 60. Dual Rectangular Jets in a Crossflow at $R=4$: Comparison of Normal Velocity Profiles at $x/D=0.0$ and $y/D=-1.0$	132
Figure 61. Dual Rectangular Jets in a Crossflow at $R=4$: Comparison of Normal Velocity Profiles at $x/D=1.0$ and $y/D=-1.0$	133
Figure 62. Dual Rectangular Jets in a Crossflow at $R=4$: Comparison of Normal Velocity Profiles at $x/D=2.0$ and $y/D=-1.0$	134
Figure 63. Dual Rectangular Jets in a Crossflow at $R=4$: Comparison of Normal Velocity Profiles at $x/D=3.0$ and $y/D=-1.0$	135
Figure 64. Dual Rectangular Jets in a Crossflow at $R=4$: Comparison of Normal Velocity Profiles at $x/D=4.0$ and $y/D=-1.0$	136
Figure 65. Dual Rectangular Jets in a Crossflow at $R=4$: Comparison of Velocity Vector Plots on the Crossflow Plane ($x/D=0.0$)	137
Figure 66. Dual Rectangular Jets in a Crossflow at $R=4$: Comparison of Transverse Velocity Profiles at $x/D=0.0$ and $y/D=-0.75$	138

Figure 67. Dual Rectangular Jets in a Crossflow at $R = 4$: Comparison of Transverse Velocity Profiles at $x/D = 0.0$ and $y/D = -0.5$	139
Figure 68. Dual Rectangular Jets in a Crossflow at $R = 4$: Comparison of Transverse Velocity Profiles at $x/D = 0.0$ and $y/D = -0.25$	140
Figure 69. Dual Rectangular Jets in a Crossflow at $R = 4$: Comparison of Transverse Velocity Profiles at $x/D = 0.0$ and $y/D = 0.25$	141
Figure 70. Dual Rectangular Jets in a Crossflow at $R = 4$: Comparison of Transverse Velocity Profiles at $x/D = 0.0$ and $y/D = 0.5$	142
Figure 71. Dual Rectangular Jets in a Crossflow at $R = 4$: Comparison of Transverse Velocity Profiles at $x/D = 0.0$ and $y/D = 0.75$	143
Figure 72. Dual Rectangular Jets in a Crossflow at $R = 4$: Comparison of Normal Velocity Profiles at $x/D = 0.0$ and $y/D = -0.75$	144
Figure 73. Dual Rectangular Jets in a Crossflow at $R = 4$: Comparison of Normal Velocity Profiles at $x/D = 0.0$ and $y/D = -0.5$	145
Figure 74. Dual Rectangular Jets in a Crossflow at $R = 4$: Comparison of Normal Velocity Profiles at $x/D = 0.0$ and $y/D = -0.25$	146
Figure 75. Dual Rectangular Jets in a Crossflow at $R = 4$: Comparison of Normal Velocity Profiles at $x/D = 0.0$ and $y/D = 0.25$	147
Figure 76. Dual Rectangular Jets in a Crossflow at $R = 4$: Comparison of Normal Velocity Profiles at $x/D = 0.0$ and $y/D = 0.5$	148
Figure 77. Dual Rectangular Jets in a Crossflow at $R = 4$: Comparison of Normal Velocity Profiles at $x/D = 0.0$ and $y/D = 0.75$	149
Figure 78. Dual Rectangular Jets in a Crossflow at $R = 4$: Comparison of Velocity Vector Plots on the Crossflow Plane ($x/D = 1.0$)	150
Figure 79. Dual Rectangular Jets in a Crossflow at $R = 4$: Comparison of Transverse Velocity Profiles at $x/D = 1.0$ and $y/D = -0.75$	151
Figure 80. Dual Rectangular Jets in a Crossflow at $R = 4$: Comparison of Transverse Velocity Profiles at $x/D = 1.0$ and $y/D = -0.5$	152
Figure 81. Dual Rectangular Jets in a Crossflow at $R = 4$: Comparison of Transverse Velocity Profiles at $x/D = 1.0$ and $y/D = -0.25$	153
Figure 82. Dual Rectangular Jets in a Crossflow at $R = 4$: Comparison of Transverse Velocity Profiles at $x/D = 1.0$ and $y/D = 0.25$	154
Figure 83. Dual Rectangular Jets in a Crossflow at $R = 4$: Comparison of Transverse Velocity Profiles at $x/D = 1.0$ and $y/D = 0.5$	155

Figure 84. Dual Rectangular Jets in a Crossflow at $R=4$: Comparison of Transverse Velocity Profiles at $x/D=1.0$ and $y/D=0.75$	156
Figure 85. Dual Rectangular Jets in a Crossflow at $R=4$: Comparison of Normal Velocity Profiles at $x/D=1.0$ and $y/D=-0.75$	157
Figure 86. Dual Rectangular Jets in a Crossflow at $R=4$: Comparison of Normal Velocity Profiles at $x/D=1.0$ and $y/D=-0.5$	158
Figure 87. Dual Rectangular Jets in a Crossflow at $R=4$: Comparison of Normal Velocity Profiles at $x/D=1.0$ and $y/D=-0.25$	159
Figure 88. Dual Rectangular Jets in a Crossflow at $R=4$: Comparison of Normal Velocity Profiles at $x/D=1.0$ and $y/D=0.25$	160
Figure 89. Dual Rectangular Jets in a Crossflow at $R=4$: Comparison of Normal Velocity Profiles at $x/D=1.0$ and $y/D=0.5$	161
Figure 90. Dual Rectangular Jets in a Crossflow at $R=4$: Comparison of Normal Velocity Profiles at $x/D=1.0$ and $y/D=0.75$	162
Figure 91. Dual Rectangular Jets in a Crossflow at $R=4$: Display of Velocity Vectors on the Plane $z/D=0.0, 0.25, 0.5$ from above	163
Figure 92. Dual Rectangular Jets in a Crossflow at $R=4$: Display of Velocity Vectors on the Plane $z/D=1.0, 2.0, 3.0$ from above	164

List of Tables

Table 1.	Display of Computational Statistics	49
----------	---	----

NOMENCLATURE

a	Sforza's constant ($= 1/.53$)
b	shear layer width
$b_{1/2}$	averaged jet half-width
C	constant
C_p	pressure coefficient
D	diameter ($= D_j = D_{eq}$)
D_{eq}	diameter of an equal area circle
D_j	diameter of a circular nozzle
f	proportionality factor for eddy viscosity
f_i	vector of body forces
$G(.)$	penalty functional
$I(.)$	a functional
J	jet-to-freestream momentum ratio
K	turbulent kinetic energy
L	streamwise length of the rectangular nozzle
L_{PC}	length of the potential core
n	direction normal to the boundary
P	static pressure
P	nodal value of the pressure
q	dynamic pressure
R	jet-to-crossflow velocity ratio
Re	Reynolds number

S	nozzle center-to-center spacing
t_i	vector of surface traction
U, V, W or U_i	mean velocity components
U_i	nodal values of the velocity components
U_{\max}	maximum velocity
u', v', w'	fluctuating velocity components
$\overline{\rho u' v'}$	Reynolds shear stress in xy plane
W	width of the rectangular nozzle
x, y, z or x_i	Cartesian coordinates

Greek Symbols

α, β, γ	coefficients of jet trajectory correlation
Γ	boundary of the computational domain
δ	variational symbol
δ_{ij}	Kronecker delta
ε	penalty parameter
μ	dynamic viscosity
ν	kinematic viscosity
Ω	bounded computational domain
ϕ	element interpolation function for velocity
ρ	density of the fluid
ψ	element interpolation function for pressure
θ	local angle of jet axis in xz -plane
ξ, ζ, η	intrinsic coordinates

Subscripts

<i>c</i>	jet center
<i>d</i>	downstream
<i>eq</i>	equal area circle
<i>j</i>	jet
max	maximum
∞	freestream
<i>p</i>	penalty
<i>PC</i>	potential core
<i>ref</i>	reference value
<i>T</i>	turbulent
<i>u</i>	upstream
1/2	half-velocity

Superscripts

<i>T</i>	transpose
–	upstream side
+	downstream side
–1	inverse
*	dimensionless quantity

Special Symbols

$\{P\}$	vector of pressure unknowns
$\{U\}$	vector of velocity unknowns
$[B]$	reduced integration penalty matrix
$[C]$	gradient matrix
$[K]$	stiffness matrix
$[K_a]$	advection matrix
$[K_d]$	diffusion matrix
$[M_p]$	pressure mass matrix

Chapter I

INTRODUCTION

1.1 GENERAL

The jet has long been studied in various engineering disciplines due to its wide range of applications, c.f. Refs. [1,2]. The jet interacts with surrounding flows to produce very active momentum and energy exchange processes. The utilization of jet flow in aerospace field can be found in many areas relating to the propulsion of aircraft. A large portion of the studies in this area have been concentrated upon co-flowing jets, but with the advent of V/STOL (Vertical and Short Take-Off and Landing) aircraft and other practical applications, the jets injected with a large angle to the crossflow have received special attention. Major applications in the V/STOL aerodynamics area may be listed as:

1. Jets interacting with ground surface during hover or landing:

Lift loss, ground erosion, recirculation, and dust ingestion.

2. Jets out of ground effect during transitional flight regime:

Transition from hover to forward flight, and vice versa,

Combat aircraft with vectored thrust capabilities

Upper surface blowing/injection resulting in increase of pitching moment.

Non-V/STOL applications of jets in a crossflow are even more numerous, and can be briefly summarized as:

1. Combustion engine applications:

Dilution air jets in combustion chambers of gas turbine engines,

Internal cooling of turbine blades by air jets,

Film cooling of turbine blades,

Supersonic fuel injection in a supersonic combustion ramjet (SCRJ) engines.

2. Industrial applications:

Action of crossflow on effluents from cooling towers or chimney stacks,

Use of air curtains to prevent cold air from entering industrial buildings.

3. Environmental applications:

Discharge of sewage or waste heat into rivers or oceans,

Atmospheric situations when thermal plumes meet crosswind at high altitude.

The major concerns of the present study are the surface pressure distribution and flowfield induced by jets in a crossflow out of ground effect with the V/STOL applications primarily in mind. V/STOL practitioners are mainly interested in the

surface pressure rather than the flowfield, so they have used inviscid panel methods to include full scale aircraft with the aid of an empirically tuned jet model [3-7]. However, the flowfield directly characterizes the pressure distribution, and vice versa, and these two should not be separated to deal with entirely new situations or parametric studies for optimum design. Due to the complicated physical nature of the problem, it seems to be a natural choice to employ the full, Reynolds-averaged, Navier-Stokes equations to simulate the flow phenomena. The objective of this theoretical study is to understand and quantify the flowfield around the jet and surface pressure distribution with the least amount of empirical information.

1.2 PHYSICAL ASPECTS OF THE FLOW

The momentum, heat and mass transfer concerning jets in a crossflow have long been studied by experimental and analytic methods in the past, and numerical methods are now extensively employed. However, although the numerical methods show a great deal of promise for universality, none of them has yet been proven to be successful in this problem due to the lack of adequate knowledge of the governing physics, such as turbulence mixing. Direct integration of the essentially exact governing equation, unsteady, Navier-Stokes equation with no turbulence modeling, requires mesh spacing of the size of the smallest eddies [8], and the computational load for 3-D, complex flow calculations is far beyond the present supercomputer's capability. Thus, it is crucial to investigate the physics of the flow to develop more cost-effective and robust prediction techniques using soundly-based turbulence models.

The model problem taken here is an unconfined single round jet in crossflow, and the flow field is sketched in Fig. 1. This shows the evolution of a round jet issuing from a pipe into a nearly uniform cross flow. Prior experimental works [2,10-14] now permit a complete physical picture to be described. The upstream is obstructed by the jet in a way similar to that of a flow past a circular cylinder, but the boundaries of the jet are compliant and entraining. The crossflow is accelerated along the jet boundaries, and the boundary interaction of the two flows leads to a periodic shedding of vortices behind the jet as in the von Karman-Bernard street. Different from the co-axial jet case, the strong pressure gradient induced across the jet by the upstream causes a large deflection of the jet. The vorticity issuing from the pipe is tilted and stretched by the flow, and forms a paired, counter-rotating, bound vortex system at the lee side of the jet. Thus, the jet cross-section has the well-known “kidney-shape”. The oncoming boundary layer due to the presence of the wall forms a so-called “horseshoe” vortex just in front of the jet exit, and this is entrained and stretched by the bound vortex along the helical path. Usually, this process is a very small scale motion, and the horseshoe vortices are absorbed by the bound vortices rapidly. The wake region is highly turbulent, and an appreciable amount of surrounding fluid is mixed and entrained into the bound vortices, which are convected by the crossflow stream. There is experimental evidence in Ref. [10] that even far downstream, say $x \cong 1000D_j$, the jet axis is aligned with the crossflow direction and little velocity excess is detected, but the pair of counter-rotating vortices and the kidney shape are still found.

At this stage, it may be informative to define terminologies which will be used throughout. The geometry and intrinsic coordinate system for analysis are given in Fig. 2. The axis of the jet (or jet trajectory) is usually defined as the locus of the maximum velocity or total pressure in the plane of symmetry [15]. Generally, the centerline which is defined as mid-way between the inner and outer boundaries of the jet in the plane of

symmetry, does not coincide with the trajectory. The jet boundary may be defined as the location where $(U-U_\infty)/(U_{\max}-U_\infty)=0.1$ at a given cross-section [11]. The vortex curve is defined as the projection of the vortex trajectories, which is the locus of the vortex center, onto the plane of symmetry [16]. The structure of the curved jet has been frequently classified in the following three distinctive zones: region 1 - Potential core region, region 2 - Zone of maximum deflection, and region 3 - Vortex zone. The details of the physical phenomena occurring in each zone can be found in any of Refs. [1,2,15,17,18].

1.3 HIERARCHY OF THE ANALYTICAL MODELS

There have been numerous efforts to analyze the problem, and the models for prediction (or correlation) may be classified in the following four categories.

EMPIRICAL MODEL - This is the oldest and simplest one, whose main concern is to correlate the jet trajectory or centerline in terms of velocity ratio or momentum ratio into a single algebraic equation using measured data. The basic structure of these correlations takes the following form for normal injection [1,2,9,10,12,13,15]:

$$\frac{z}{D_j} = \alpha R^\beta \left(\frac{x}{D_j} \right)^\gamma \quad (1.1)$$

where α , β , and γ are empirical coefficients which have following variations according to the experimental condition.

$$0.75 \leq \alpha \leq 1.31, \quad 0.74 \leq \beta \leq 1.0, \quad 0.33 \leq \gamma \leq 0.39$$

In cases where the density of the jet is different from that of the crossflow, the above relation is also valid if the velocity ratio, R , is replaced by the square root of the momentum ratio, $J^{1/2}$. Also, the effect of an injection angle other than 90° can be included. The vortex curves have been correlated in a similar fashion [16].

For the single, round jet case, these correlations may be used to predict jet trajectory, especially for the far-field. The main disadvantage is that their application is limited to the range of available data and that only qualitative checks of results produced by more elaborate methods can be made.

ANALYTICAL MODEL - This was mainly done by Russian scientists, and can be described as a momentum integral approach over a control volume across the jet. The major assumptions are given in Ref. [2]:

1. The momentum of the jet in the direction normal to the crossflow is preserved and the pressure difference across the jet is balanced by the centrifugal force due to the curvature.
2. The aerodynamic drag force acting on the jet surface can be simulated using an arrow wing analogy with curved axis.
3. The kidney shaped cross section of the jet is assumed as an ellipse and its width increases approximately proportional to the distance from the nozzle. Furthermore, it is assumed that the rate of expansion of the cross section is the same as that in a jet of rectangular cross-sectional shape:

$$\Delta y = 2.25D_j + 0.22\xi \cong 2.25D_j + 0.22x \quad (1.2)$$

The resulting governing equations were reduced to an ordinary differential equation (ODE) which could be solved analytically or by the method of successive approximation. Even though these approaches were simple, some of these ideas and assumptions have been utilized in many later analytical works.

INTEGRAL MODEL - This is often called the semi-analytic model, and it uses integral equations derived either by considering a balance of momentum and energy acting on the control volume or by integrating in two special dimensions or full three dimensions, resulting in a set of ordinary differential equations which can be solved analytically or numerically. Since more physics were included in these models, the predictions are fairly realistic and inexpensive, but these models still rely on experimental information in large part.

A versatile model was suggested in Refs. [19,20], which took into account the drag, entrainment, buoyancy, axial pressure gradient, turbulence mixing, and heat transfer. The integral momentum equations were derived on the basis of the intrinsic coordinate system, and various other effects were included from similar empirical relations. Comparisons of the predicted results with existing measured data showed relatively good agreement and a wide range of applicability. The model was extended in Ref. [21] to predict trajectories of double jets arranged in a row or in tandem. The interactions between the jets were accounted for by modifying the drag coefficient based on experimental data for the interaction between circular cylinders.

A quasi-3D model was developed in Ref. [22], whose relative merit over the other integral models was to predict the development of the jet cross section shape from a circle to a horseshoe configuration. Also, the internal jet velocity profiles were obtained from a solution of Poisson's equation within the jet cross section combined with the empirical parameters.

For the V/STOL application, the prediction of surface pressure induced by a jet is of prime importance [23]. Using the panel method, the surface pressure can be determined without solving for the entire flowfield. Thus, the above mentioned integral representation of the jet could effectively be incorporated into the inviscid flow calculation. For example, the windward side of the jet is paneled as a solid surface, and the leeward side of the jet is composed of panels with prescribed normal velocity representing the entrainment [7]. Even though this method relies heavily on experimental information, it may be a practical way to take into account the effect of jets into the potential flow calculation for a full-scale aircraft.

NUMERICAL MODEL - With the advent of the high speed digital computers, numerical methods become the most promising tool to analyze the problem. Earlier studies used the finite difference method to solve the full Navier-Stokes equations for jet flow fields with zero-equation [24] and two-equation [25] turbulence models. The study of Ref. [24] used the velocity-vorticity-temperature formulation to get the steady-state solution with application to the channel flow and a buoyant jet in a crossflow at $R = 4$. High velocity ratio cases ($R = 2$ to 10) were studied in Ref. [25], and according to Ref. [8], the agreement with experiment was enhanced in spite of the relatively coarse mesh ($15 \times 15 \times 10$) by treating the location of the numerical boundaries and the top and farfield boundary conditions in the same ways as in an experiment.

Further, due to the huge work space and CPU time required for a full elliptic treatment, parabolized approximations have been tried by several workers. A fully parabolic calculation was presented in Ref. [26] where downstream marching in the direction of the crossflow was used, and the result was poor even for very low velocity ratio. A partially parabolic approach (only pressure is elliptic) was used in Ref. [27], where repeated downstream marching was used, and it was found to be more expensive than a parabolic Navier-Stokes (PNS) approach and at the same time not applicable for

the high velocity ratio cases. Similar techniques with slight modification, a locally elliptic (a combination of parabolic, partially parabolic and elliptic) approach, were applied to the low velocity ratio case in Ref. [28]. It required adaptive refinement of the locally elliptic region. Some advantage of this approach was reduced storage requirement comparable to that of the partially parabolic method, while the CPU time approached that of fully elliptic one. The above three studies used a two-equation turbulence model to simulate confined jet(s) flows at low R for combustor applications.

For a very high velocity ratio case, PNS calculation using the finite element method was reported in Ref. [29] where the space marching direction was not the crossflow direction but the jet axis, more exactly the z axis. A two-equation model was employed along with an algebraic stress model which was originally developed for the juncture flow. Major difficulties of this approach were specification of the initial condition at the wall and farfield boundary conditions. The former was supplied by the measured data in Ref. [30], and the latter was determined by solving a pressure Poisson equation using the same measured data.

Returning to the full, Navier-Stokes approach, the work of Ref. [31] may be the first which includes the effect of a nozzle hole calculation whose significance has been stressed by many experimental studies [32,33]. This study also used a two-equation model and performed a separate hole calculation to determine the jet exit boundary conditions and showed fairly good results for $J = 0.0576$ and 4.

The high resolution vorticity field was simulated in Ref. [34], whose approach used centered differencing in space and explicit (leapfrog) time integration with a variable time step. A one-equation model was used with a simple length scale taken as linearly proportional to the distance from the nozzle.

General observations on the previous numerical simulations for this problem are that the finite difference (or volume) technique was used for discretization and

two-equation turbulence model was employed in most cases. The following observations on these two issues can be drawn as:

Numerics: It is well known that the use of a centered-difference scheme for the approximation of the advection terms in high-Reynolds-number flow may result in a “wiggly” solution, if the cell Reynolds number is greater than 2. On the other hand, the use of hybrid (mixed central and upwind) differencing scheme to suppress these wiggles is known to introduce numerical diffusion. Thus, the modeling of the advection terms should be viewed as the art of compromise between oscillatory and diffusive errors under the grid-dependence of the solution. However, the observation given here is not necessarily applied to all the upwind methods because the diffusion due to upwinding may be made to be same order as the truncation error according to the scheme used. A recent calculation with three grid distributions for a circular jet in a crossflow in a combustor [35] reports that, even with the finest grid (90x22x40), the solution still showed grid-dependence and the velocity peaks were controlled by the numerical diffusion, even though slight improvement was observed at each refinement level. The magnitude of this false diffusion was often much higher than the turbulent diffusion, and this could cause excessive spread. The use of higher order scheme, such as QUICK (Quadratic Upstream Interpolation for Convective Kinematics [36]), to suppress the false diffusion has been tried in Ref. [37]. But, according to this study, the use of the QUICK scheme was found to be about two times more expensive than the use of the hybrid differencing for the same problem. Recently, PISO (Pressure Implicit Split Operator) algorithm [38] was developed and found to be several times faster than the original Patankar-Spalding technique [39]. Much research is going on in many groups to try to improve the situation.

Turbulence model: Among various two-equation models, the $k\epsilon$ model has been most widely used and its advantages are the straightforward nature of the numerical procedures whether the equation is parabolic or elliptic and its comprehensive mathematical treatment of the production, convection, diffusion and dissipation of the turbulent kinetic energy. Two-equation models applied to this problem used the “standard” coefficients developed in simple two-dimensional flows. Since the flowfield, at least in the near jet nozzle, is mainly controlled by pressure forces with comparatively small differences between laminar- and turbulent-flow results, the influence of the turbulence model should be relatively small [8]. All the calculations with the two-equation model and pressure-corrector (SIMPLE, Semi-Implicit Method for Pressure-Linked Equations) algorithm [39] showed significant differences which were most likely due to boundary conditions or numerical assumptions for the turbulence quantities.

1.4 CURRENT ISSUES OF RESEARCH

Most of the earlier studies of jets in a crossflow are limited to a single- or a row of circular jets. Recent experimental studies have included various other parameters: rectangular nozzles [41,45], dual jet configurations [42-45], nonuniformity of the exit velocity profile [44], and injection from a body of revolution [40,42], among others. Streamwise aligned rectangular jets have received a special attention due to the convenience of installation on the side of the V/STOL aircraft and less blockage effect against the crossflow for the same jet exit area than the circular ones. Nonuniform exit conditions are also very important for jets issued by a fan or exhausted from an engine.

As for the analytical approaches, most of the recent studies have used inviscid flow techniques to determine the surface pressure economically with the aid of empirically tuned jet trajectory or entrainment rate. The study in Ref. [6] used a combination of the lifting surface code and empirically tuned jet properties [42] to determine the surface pressure distribution over a wing or a body of revolution. Some other studies [4,5] have tried to include the viscous effects in the separated flow region by superposing the empirically correlated viscous pressure correction term to the inviscid surface pressure.

1.5 FEM IN TURBULENT FLOWS

The use of the finite element method for turbulent flows can be found in the recent literature [48-56]. Reference [54] summarizes the research activities from various groups in detail. Taylor and co-workers at Swansea, U.K., have used the mixing length, one-equation, and two-equation models to solve simple turbulent flow problems [48-51]. They used the standard Galerkin method to discretize the Reynolds-averaged, Navier-Stokes equations, where the mean flow variables (velocity and pressure) and the turbulent quantities were fully coupled. Numerical examples included the fully-developed pipe flow, planar free-shear flow, and planar backward facing step problems. Due to the steep velocity gradient near the wall, special treatments are employed for the wall region, e.g. law of the wall. Furthermore, to deal with flow separation in the last example, *a priori* knowledge of the reattachment point was required to model the shear stress on the wall. The system of algebraic equations was solved using an unsymmetric frontal solver at each iteration, and a number of iterations was required to reach convergence. In most cases, successive substitution with

under-relaxation was employed, and the Newton method could not be used. Even with that method, a very slow rate of convergence was observed. The mean flow field was predicted well, but the turbulence quantities did not compare well with measured data. Also, careful *ad hoc* treatment for the turbulence quantities had to be included during iterations, otherwise these quantities had unrealistic values and the solution diverged at once.

Larock and Schamber [52,53] have reported finite-element discretization for two-equation and Reynolds stress models along with the Reynolds-averaged, Navier-Stokes equations. In the study of Ref. [52], a decoupled formulation of the global equation system into a mean flow equation set and a turbulence model equation set was proposed. Thus, the iterations proceeded by solving the two sets of equations alternatively, and this strategy may offer some advantages, such as, easy initialization and a reduced core storage requirement, but it required more computation cycles. The calculation of a sedimentation basin problem using two-equation model was about 10 times more costly than the constant viscosity calculation.

A half-equation turbulence model was used in Ref. [54] to solve 3-D flow around the propeller, where an integrated turbulent kinetic energy equation was reduced to a ordinary differential equation which can be integrated along the primary direction of flow. The propeller was modeled as an actuator disk, and the surface traction components were specified on the disk using the measured data. Due to the absence of the wall boundary and the dominance of the primary directional flow, a quasi-Newton method could be used after one or two successive substitutions to reach convergence. The same method was extended in Ref. [55] to calculate the propeller flowfield with a non-uniform inflow, and a similar technique was used in Ref. [56] to solve the flow over a slender, propeller-driven body with the wake from a slender, planar appendage with a simplified treatment of the near wall region.

1.6 OBJECTIVES OF THIS WORK

This study aims at the numerical prediction of the flowfield and the surface pressure distribution induced by various jet configurations appearing in V/STOL applications especially for moderate to high R . Due to the ever increasing complexities of the problem, the amount of experimental data required for the optimum design of this high lift device becomes tremendous. Thus, it is a natural direction to try to utilize well-developed, modern numerical techniques to minimize the amount of time and money involved in wind tunnel testing.

The present study employs the finite-element method to solve the incompressible, 3-D, Reynolds-averaged, Navier-Stokes equations with a penalty approximation for pressure. The FEM was chosen as a numerical tool because its robustness and flexibility in handling various engineering problems described by elliptic partial differential equations. Further, it can handle complex geometry easily and its boundary conditions are more physically relevant quantities than the pure mathematical ones.

As for the solution strategies, in case the Euler explicit method is employed, the associated stability criteria are not well known, and the use of a small time increment makes it compulsory to use the mixed (velocity-pressure) formulation which has one more unknown per node than the penalty formulation. On the other hand, for the implicit integrators, a nonlinear system of algebraic equations must be solved at each time step. Detailed comparisons and discussions on the time integrations in 2- and 3-D can be found in Ref. [77]. But the definite superiority of a specific scheme over the others in 3-D is not clearly found yet and still many new approaches are tried. In spite of the requirement of a large work space, steady-state solution techniques are employed here. LU decomposition is performed to solve the large, sparse, unsymmetric matrix

system via a compacted, skyline, out-of-core solver, and nonlinear iteration is done using successive substitution. Isoparametric trilinear-velocity, constant-pressure elements are employed to discretize the domain.

For the effects of turbulence mixing, there exists some information [11,14,46,47] only for the circular jet case, and very little is known for various other configurations or exit conditions. A 3-D, finite-element formulation of the two-equation model is straightforward, but since there exist no universal coefficients and the isotropy assumption breaks down in very important regions of the flow [46], it seems questionable to employ higher-order models with their greatly increased computational load. Furthermore, the experimental study of Ref. [46] reveals some possibility of the use of an eddy-viscosity model in this flow, even though it is not completely satisfactory. Based upon this suggestion and the observations made in Sec. 1.3, Prandtl's eddy-viscosity concept for the planar/axisymmetric jet was extended here to account for the curved jet(s) issuing from various nozzle configurations in a uniform crossflow.

The current study performed computations on three problems of different nozzle configurations all at $R = 4$: single circular jet, single rectangular jet, and dual rectangular jets in a crossflow. Cases with $R = 4$ were selected for two reasons. First, many applications including V/STOL cases involve values in this range. Second, lower or higher R values are extreme cases where either the jet or crossflow dominates. The first configuration - the circular jet, has long been studied and applied in practical situations, and it was selected here for the purpose of verification of the prediction method. The second and third configurations involve fairly recent issues as mentioned in Sec. 1.4. The flowfields for the last two cases are much different and more complicated than the first one, and only a little experimental information is available from the most recent literature [41,43,45]. These cases provide a stringent test for any prediction method.

Chapter II

TURBULENCE MODEL

2.1 BACKGROUND

One of the main issues in any high Reynolds number, viscous flow calculation procedure is turbulence modeling. Thus, that issue is addressed in detail first.

As can be seen in the Introduction, most of the prior computational studies have used the $k\varepsilon$ turbulence model or its variants except for the study of Ref. [24], where an eddy viscosity model taken from axisymmetric jet flows [57] was used. It may be informative to estimate the global level of turbulence mixing for a circular jet in a crossflow using experimental observations. For circular jets in a stagnant or coflowing stream, the maximum velocity or velocity defect at any section decreases inversely with axial distance [1,2,57]. According to Ref. [58], the above concept is valid for a jet in a crossflow up to some limiting value of ξ/D , and this limiting value decreases with decreasing value of R . The study of Ref. [11] reported that, for $R= 4, 6$ and 8 , a single

functional behavior of the axial jet velocity exists, and the lateral velocity profiles show a similarity when scaled by appropriate lengths and velocities, but true self-preservation is not attained. The lateral spread of the jet determined at the half velocity point increases linearly with the axial distance ξ' from the virtual origin, located about $1.87D_j$ for $R = 4$ behind the nozzle, as:

$$b = 0.215\xi' \quad (2.1)$$

Similarity was also observed in Ref. [59], for $R = 4.5 \sim 23$, and the velocity distribution in any radial direction in the $\eta - \zeta$ plane was found to be similar. Thus, taking the velocity scale proportional to $1/\xi$ and length scale proportional to ξ , the kinematic eddy viscosity may be written as:

$$v_T \propto \text{velocity} \times \text{length} = \text{constant} \quad (2.2)$$

along the jet axis ξ . This result returns to the model used in Ref. [24] and may be used for the initialization of eddy viscosity field at high R .

2.2 EDDY VISCOSITY MODEL FOR A CURVED, 3-D JET

It is well known that the basic eddy viscosity concept can be successfully applied to a wide range of free shear flow problems [60]. The main idea of the present approach is to develop a robust turbulence model which can deal with the jet injected from an arbitrarily shaped nozzle in a crossflow. Since the cross section of the jet varies due to

the action of the crosswind, the main emphasis was given to the identification of the 3-D jet shape to determine reasonable turbulence length and velocity scales. The potential core, whose length here is much shorter than that in free jet, was included to avoid unrealistic mixing near the nozzle exit. The eddy viscosity expression applicable to a jet of arbitrary cross section in the coflowing stream was obtained and finally refined to include the first-order effect of turbulence structure using the hypothesis given in Ref. [61]. First, consider the specification of a suitable length scale related to a characteristic shear layer width.

2.2.1 CHARACTERISTIC SHEAR LAYER WIDTH

Since the computation domain considered here encompasses the potential core region and the zone of maximum deflection, the velocity profile cannot be regarded as being self-similar. Therefore, it was required to define a characteristic shear layer width to represent the growth and spread of the jet in each zone separately. A definition sketch for the analysis of a jet in a crossflow is given in Fig. 2. Probably the most important feature of this flow is the curved path due to the strong pressure gradient acting across the jet. Since the curvature of the jet varies rapidly in this region, simple experimental correlations for the jet shape, such as given in Ref. [10], were found to be inadequate for the present situation. In free shear flows, it is generally accepted that a mixing length increases along the length of the flow while the variation across the flow is so little that this can often be ignored [62]. Furthermore, it is not necessary to modify it for the wall effect [1] in free shear flows. The definition of the jet width is not quite clear, because the fluctuating nature of the turbulent portion makes it difficult to precisely measure the location where turbulent mixing disappears. Various definitions

have been tried by many reseachers and their common method of judgement is based upon the ratio of flow velocity defect to the maximum velocity difference across the layer [62]. Another problem is how to define the geometry of the curved jet using Cartesian coordinates instead of the intrinsic coordinate system. Even in the experimental studies, the traverse of a probe in the exact ζ direction has hardly ever been reported. In Ref. [12], a hot wire anemometer was aligned with the y axis, and traversed in the xy plane, and a series of data reduction steps was followed to interpret the results in the intrinsic coordinate system. In Ref. [13], velocity was measured along the z axis at given x locations, and jet width was defined using the location of the half-velocity whose slope is parallel to the jet axis. In the present investigation, the plane of symmetry of the nozzle was taken as the reference plane, and the jet shape was determined by the following procedures:

1. At a given z location, the point of maximum velocity, U_{\max} defined by $(U^2 + V^2 + W^2)^{1/2}$ is found by scanning along the x direction.
2. The local slope of the jet axis is taken as tangent of the maximum velocity vector. This slope is assumed to be constant across the jet, i.e. both in x or ζ direction.
3. Searching for the jet mixing boundaries across the jet in the xz plane is performed. Since the profile across the jet is asymmetric, the width is decomposed into upstream and downstream parts denoted by superscript $-$ and $+$, respectively. Here, every velocity is decomposed into ξ and ζ components using the slope of the jet axis, and a convenient notation is introduced to define the location, ζ_{\pm}^* , where the following relation is satisfied at a given cross section, ξ , as:

$$\frac{U_{\xi} - U_{\infty}}{U_{\max} - U_{\infty}} = \lambda \quad (2.3)$$

where U_{ξ} means the ξ component of the velocity.

Actual identification of the jet mixing boundaries was performed by finding half-velocity points, $x_{1/2}^{\pm}$ at a given z .

4. Searching for the jet mixing boundaries in the yz plane was followed in the same manner. Starting from the given maximum velocity point, scanning in the y direction is continued until $\eta_{1/2}^{\pm}$ is reached. If the profile is symmetric with respect to the xz plane, only one half-width is required.
5. The characteristic shear layer width for the jet was defined as the half jet width in an averaged sense, and a convenient expression was obtained by generalizing 3-D rectangular free jet model suggested in Ref. [63] as:

$$b_{1/2}(\xi) = \left[\frac{\zeta_{1/2}^a \eta_{1/2}^a}{\zeta_{1/2}^a + \eta_{1/2}^a} \right]^{1/a} \quad (2.4)$$

where

$$\zeta_{1/2} \equiv \frac{(\zeta_{1/2}^- + \zeta_{1/2}^+)}{2} \cong \frac{(x_{1/2}^- + x_{1/2}^+)}{2} \sin \theta \quad (2.5)$$

$$\eta_{1/2} \equiv \frac{(\eta_{1/2}^- + \eta_{1/2}^+)}{2} = \frac{(y_{1/2}^- + y_{1/2}^+)}{2} \quad (2.6)$$

Here, θ is the angle between x axis and the jet axis, and $\alpha^{-1} = 0.53$.

2.2.2 POTENTIAL CORE CORRECTION

Near the jet exit, there exists a potential core region where turbulent mixing is not so active. According to the measurements of Ref. [10], the length of this region is about two jet diameter for small R and approaches that of a free jet, about six jet diameters, as R goes to infinity (Fig. 3). An attempt was made in Ref. [12] to extend the linear relation for a free jet mixing layer including the effect of crossflow in the form of additional tangential stress. Therefore, the core length was estimated by the following:

$$\frac{L_{PC}}{D_j} = \frac{1}{D_j/L_0 + 0.72/R} \quad (2.7)$$

where L_0 is the core length for free jet and a value of $6.4D_j$ was used. This relation compared well with the data of Ref. [6]. In the present study, a linear relation for the coflowing planar jet given in Ref. [2] was used to determine the growth of the mixing layer in the potential core region as:

$$\frac{db_{PC}}{d\xi} = \frac{0.27}{2} \frac{(1-m)}{(1+m)} \quad (2.8)$$

where $m = 1/R$.

Integrating the above equation from the nozzle exit,

$$b_{PC} = \frac{0.27}{2} \frac{(1-m)}{(1+m)} \xi + b_{PC}(0) \quad (2.9)$$

where $b_{PC}(0)$ was introduced to avoid a zero length scale at the nozzle exit, and the displacement thickness of the boundary layer was used to represent this initial value. The width b_{PC} can only be used as a reference length scale until it becomes greater than

or equal to $b_{1/2}$. The resulting core length for $R = 4$ was about 3 jet diameters, which is in good agreement with the estimation by the method of Ref. [12] or data given in Ref. [10].

In the rectangular jet problem, there exist three distinctive regions [63]; potential core, characteristic decay, and axisymmetric decay region. Thus, the above scheme was extended to include these regions as:

1. In the potential core region, where $b_{PC} \leq \eta_{1/2} \leq \zeta_{1/2}$, b_{PC} was used instead of $\eta_{1/2}$ and $\zeta_{1/2}$.
2. In the characteristic decay region, where $\eta_{1/2} \leq b_{PC} \leq \zeta_{1/2}$, b_{PC} was used instead of $\zeta_{1/2}$.
3. In the axisymmetric decay region, where $\eta_{1/2} \leq \zeta_{1/2} \leq b_{PC}$, b_{PC} was not used.

Some mention should be made about the use of half-velocity point instead of using 1% or 10% point as in Ref. [62] to define the jet shape. Our experience with the latter definitions is that the appearance of double peaks in the velocity field at the downstream locations resulted in large uncertainties and unrealistic values of jet width.

2.2.3 MODEL FORM

The velocity scale chosen here is given by:

$$\Delta U_c(\xi) = U_{\max} - U_{\infty} \quad (2.10)$$

similar to the usual free shear flow cases.

Thus, the eddy viscosity for the jet at a given ξ location may be determined as:

$$\mu_T = 0.037\rho b_{1/2}\Delta U_c \quad (2.11)$$

The above model may be viewed as a generalized expression of the Prandtl's "difference" model for a jet of arbitrary cross section in a coflowing stream. Examining this model carefully, one can see that it returns to co-axial circular jet form when $\zeta_{1/2} \rightarrow \eta_{1/2}$, and planar jet form when $\zeta_{1/2}$ or $\eta_{1/2}$ becomes very large or very small compared to the other [63].

2.2.4 PROPORTIONALITY CONSTANT

The above expression is a kind of mean flow model which does not directly reflect the fluctating nature of the turbulent flow [1]. The eddy viscosity models that have been successfully applied to jet or wake cases often do not perform adequately when applied to the other case, and this is so even when the functional forms of both kinds of models are essentially identical [1]. The primary controlling factor for this discrepancy is believed to be the proportionality constant, and the connection between this constant and the turbulence quantities was investigated in Ref. [61]. Using the unified eddy viscosity model [1] developed by the same author, the turbulent shear stress for the planar free shear flow may be given as:

$$-\overline{u'v'} = C\left(\frac{\Delta U_c}{b}\right) \int_0^\infty \Delta U \, dy \cong C \times C_1(\Delta U_c)^2 \quad (2.12)$$

where C_1 is a constant which depends on the specific profile shape, and typical shapes yield a value of roughly one-half. On the other hand, one may write [57]

$$-\overline{u'v'} = C_2 \sqrt{\overline{u'^2}} \sqrt{\overline{v'^2}} \quad (2.13)$$

where C_2 is also a constant of about one-half. Also, generally in shear flows [57]

$$u' \cong -v' \quad (2.14)$$

Thus, the final result may be written as:

$$\frac{\overline{u'^2}}{(\Delta U_c)^2} \cong C \quad (2.15)$$

since C_1/C_2 is expected to be near unity. The same author also demonstrated that the same eddy viscosity model can predict both jet and wake flows by adjusting the proportionality factor with the aid of axial turbulence intensity data.

This approach, named an “algebraic turbulence function model” [1], can crudely reflect the first-order influence of turbulence structure into an eddy viscosity model if axial turbulence intensity data are provided. Such data are given in Ref. [11] for the circular jet in a crossflow case (Fig. 4), and it indicates more intensive entrainment processes compared to the free jet case in the near jet field. Thus, the eddy viscosity model developed up to now can be refined to include the above mentioned effect according to the hypothesis of algebraic turbulence function model. Introducing a notation:

$$f(\xi) = \frac{\overline{u'^2}}{\Delta U_c^2} \quad (2.16)$$

f may be correlated from [11] as:

$$f(\xi) = \begin{cases} 2 & \text{for } \xi \leq \xi_{PC} \\ 1 + e^{-c(\xi - \xi_{PC})} & \text{for } \xi \geq \xi_{PC} \end{cases} \quad (2.17)$$

where $c = 1.134$.

The final form of eddy viscosity model adopted here is given by:

$$\mu_T = 0.037 f \rho b_{1/2} \Delta U_c \quad (2.18)$$

Chapter III

FINITE ELEMENT PROCEDURES

3.1 OVERVIEW

A partial differential equation describing a physical phenomenon can be formulated either as a differential problem or equivalently as a variational problem. A differential formulation finds a function which satisfies a relation between the function itself and its derivatives subject to the given boundary conditions. A variational formulation seeks a function that minimizes, maximizes or makes stationary a functional subject to given boundary conditions. The two formulations are equivalent if both admit the same unique solution. The variational formulation often has advantages over the differential one from the numerical point of view [64-67]: Firstly, the functional contains derivatives of lower order than the differential problem, which enables one to find an approximate solution in a large class of functions. Secondly, the variational formulation treats complicated boundary conditions in a simple way in non-rectangular regions. The

classical variational methods of approximation were found to be less competitive with finite difference method due to the difficulty encountered in selecting the approximation functions when the domain is geometrically complex or boundary conditions are complicated. The main idea of the finite element method is to circumvent these difficulties by discretizing the entire domain into a set of geometrically simple shapes called elements for which the construction of the approximation function is independent of boundary conditions. The governing partial differential equation can be formulated using any variational method, and the resulting integrals are evaluated at the element level with the aid of those approximation functions. Assembly to a global system is done via connectivity of the elements to construct an algebraic matrix system which can be solved after imposition of boundary conditions. Since the whole procedure is systematic, and the formulation is independent of the shape of the domain and boundary conditions, the finite element method has become quite popular for the efficient implementation on the digital computer [64,65,66,67].

It may be helpful here to discuss the choice of the mathematical formulation for the incompressible Navier-Stokes equations. At the early stages of finite element applications in fluid dynamics, the stream function-vorticity formulation [68] was frequently employed. The main advantage of this approach is deletion of the continuity equation and, thereby, a reduced number of unknowns and elimination of the pressure. The critical drawback of the application of this method is that it is essentially limited to 2-D/axisymmetric cases due to the definition of stream function which is simple only in 2-D. In many cases, the boundary conditions for the stream function are available, but the same is not true for vorticity. This means that the boundary conditions for the vorticity should be solved with the governing equations simultaneously, which is undesirable from the numerical point of view. Experience with this method has shown that the computed stream function is accurate, but the vorticity is inaccurate [67].

Furthermore, the velocity components extracted from the stream function by numerical differentiation are less accurate than those from a primitive variable (velocity and pressure) formulation. In the course of a pressure computation, this behavior is even more strongly reflected, since higher order derivatives of the stream function are required. Thus, the primitive variable approach has been employed in most cases, and its main advantages are that the variables are more physically relevant quantities and the extension to 3-D is straightforward. The only difficulty is the mathematical and physical treatment of pressure. In contrast to compressible flow cases, pressure is not related to any thermodynamic equation of state. Furthermore, it does not appear explicitly in the continuity equation even though its behavior is strongly dependent upon the satisfaction of continuity equation [67].

In the present study, the mathematical formulation is based upon the steady, incompressible, Navier-Stokes equations in a primitive variable form along with the continuity equation. The variational formulation is obtained through the weighted residual method using the generalized Galerkin technique. Earlier finite element discretizations employ mixed formulation with continuous pressure approximations [69-71]. Recent studies [72-74] utilize penalty function formulations with a discontinuous pressure approximation, which leads to a better conditioning of the final system matrix and a reduced number of unknowns containing only the velocity components.

It is well known that in the finite element discretization of incompressible media, the approximation for velocity and pressure should satisfy certain consistency conditions in order to obtain a stable convergent solution [65,73]. This condition is known under the name "Brezzi-Babuska" condition (or BB condition). However, the BB condition is rather abstract, and, in practice, it is very difficult to verify whether it is satisfied or not.

A simple method is suggested in Ref. [75] to check the BB condition for a number of new and old elements.

3.2 GOVERNING EQUATIONS

One method of describing three-dimensional, steady-state, isothermal, incompressible, turbulent flow, in a Cartesian coordinate system (x,y,z) is to utilize the Reynolds-averaged, Navier-Stokes equations [57] in tensor form:

$$\rho U_j \frac{\partial U_i}{\partial x_j} = - \frac{\partial P}{\partial x_i} + \frac{\partial}{\partial x_j} \left[\mu \left(\frac{\partial U_i}{\partial x_j} + \frac{\partial U_j}{\partial x_i} \right) - \overline{\rho u_i' u_j'} \right] + \rho f_i \quad (3.1)$$

together with the continuity equation:

$$\frac{\partial U_i}{\partial x_i} = 0 \quad (3.2)$$

It should be noted that the momentum equation is written in the stress-divergence form resulting in natural boundary conditions which can be interpreted physically as the components of stress acting on the fluid at the boundary. In case usual Navier-Stokes form (where the viscous diffusion term is reduced to a Laplacian after applying the continuity equation) is used, the resulting natural boundary condition is a pure Neuman type with no corresponding direct physical interpretation. Even though the two forms result in only a slight difference for laminar flow calculations, the stress-divergence form is strongly recommended for turbulent flow computation [77-79,82].

Using the Boussinesq hypothesis [57] which assumes that, in analogy to the viscous stresses in laminar flow, the components of the Reynolds stress tensor are linearly proportional to the mean velocity gradients, the turbulent shear stress is expressed as:

$$-\overline{\rho u_i' u_j'} = \mu_T \left(\frac{\partial U_i}{\partial x_j} + \frac{\partial U_j}{\partial x_i} \right) - \frac{2}{3} \delta_{ij} K \quad (3.3)$$

where μ_T is the turbulent eddy viscosity and K is the turbulent kinetic energy. In free shear flows there is no wall region and the laminar viscosity is negligible compared to the turbulent viscosity, so the momentum equations can be rewritten as:

$$\rho U_j \frac{\partial U_i}{\partial x_j} = -\frac{\partial P}{\partial x_i} + \frac{\partial}{\partial x_j} \left[\mu_T \left(\frac{\partial U_i}{\partial x_j} + \frac{\partial U_j}{\partial x_i} \right) \right] + \rho f_i \quad (3.4)$$

where the pressure was redefined to include the effects of the turbulence normal stresses.

3.3 VARIATIONAL FORMULATION

The finite element method has been introduced as a particular case of the Ritz method which is applicable to extremal formulation of partial differential equations [67]. Unfortunately, there exists no such functional in the classical sense for the Navier-Stokes equations [76]. But, the Galerkin method, a generalization of the Ritz method, can be applied to the boundary value problems irrespective of the existence of an equivalent extremal formulation, which enables one to construct a variational (weak) form of the Navier-Stokes equations. Indeed, the Galerkin technique is one of the methods of weighted residuals (MWR) which seek a linearly independent set of weighting functions

orthogonal to the residual by making the integral of the weighted residual zero. In the Galerkin method, the weighting function becomes the approximation function itself.

Using the definition of the Galerkin procedure [66], variational forms for the field equations are obtained. The first step is to multiply the residual by a variation, and the next step is to perform integration by parts, i.e. the Green-Gauss theorem is used to reduce the second-order diffusion terms and the pressure (or penalty) term to a surface integral.

$$\int_{\Omega} \delta U_i \left\{ \rho U_j \frac{\partial U_i}{\partial x_j} + \frac{\partial P}{\partial x_i} - \frac{\partial}{\partial x_j} \left[\mu_T \left(\frac{\partial U_i}{\partial x_j} + \frac{\partial U_j}{\partial x_i} \right) \right] - \rho f_i \right\} d\Omega = 0 \quad (3.5)$$

$$\int_{\Omega} \left\{ \delta U_i \rho U_j \frac{\partial U_i}{\partial x_j} - \frac{\partial \delta U_i}{\partial x_j} P + \mu_T \frac{\partial \delta U_i}{\partial x_j} \left(\frac{\partial U_i}{\partial x_j} + \frac{\partial U_j}{\partial x_i} \right) - \delta U_i \rho f_i \right\} d\Omega = \int_{\Gamma} \delta U_i t_i d\Gamma \quad (3.6)$$

Even though the pressure terms are first order, they are also integrated by parts to obtain physically meaningful boundary conditions and the symmetry of the finite element equations [66]. Thus, $t_i = [-P\delta_{ij} + \mu_T(U_{i,j} + U_{j,i})]n_j$ represents the applied surface stress (traction) in the i direction. It should be noted that boundary conditions for pressure are not defined explicitly, and pressure is determined within a constant. Specification of pressure on the boundary is available only implicitly through the imposition of stress (traction) conditions [77].

The variational formulation for the continuity equation is given by

$$\int_{\Omega} \delta P \frac{\partial U_i}{\partial x_i} d\Omega = 0 \quad (3.7)$$

According to the way of enforcement of the mass continuity constraint, the approximation of pressure varies. In a primitive variable approach, two common ways are mixed (velocity-pressure or Lagrange multiplier) and penalty function method. The mixed formulation enforces the incompressibility constraint in the exact sense, while the penalty formulation enforces it in a least square approximation sense [66]. However, the penalty method is equivalent to the perturbed Lagrangian method [65], and this becomes equivalent to the appropriate mixed counterpart when implemented in a consistent manner [78].

3.4 MIXED FINITE ELEMENT METHOD

Approximation functions for velocity and pressure within each element are introduced as:

$$U_i = \phi^T U_i \equiv \sum_{k=1}^N \phi_k U_{i,k} \quad (3.8)$$

$$P = \psi^T P \equiv \sum_{k=1}^M \psi_k P_k \quad (3.9)$$

where ϕ and ψ are the elemental approximation function of degree N and M , respectively, and U_i and P denote the nodal values of velocity components and pressure which are independent of the coordinates. Neglecting the body force term, substitution of eqs. (3.8) and (3.9) into eq. (3.6) results in the following integral equations:

$$\int_{\Omega} \left\{ \rho \phi U_j \frac{\partial \phi^T}{\partial x_j} + \mu_T \frac{\partial \phi}{\partial x_j} \left(\frac{\partial \phi^T}{\partial x_i} + \frac{\partial \phi^T}{\partial x_j} \right) \right\} d\Omega U_i - \int_{\Omega} \frac{\partial \phi}{\partial x_i} \psi^T d\Omega P = \int_{\Gamma} t_i \phi d\Gamma \quad (3.10)$$

$$\int_{\Omega} \psi \frac{\partial \phi^T}{\partial x_i} d\Omega U_i = 0 \quad (3.11)$$

The integrals are evaluated within each element using Gaussian quadrature. Thus, the coefficient matrices and right-hand-side vectors are constructed at the elemental level and assembled into a global system matrix and a force vector with the aid of the connectivity matrix. For convenience, representing the system of matrix equation in a partitioned form at the elemental level (this process is not always possible for conforming mixed methods until assembly to a global system [65])

$$\begin{bmatrix} [K] & -[C] \\ -[C]^T & [0] \end{bmatrix} \begin{bmatrix} \{U\} \\ \{P\} \end{bmatrix} = \begin{bmatrix} \{F\} \\ \{0\} \end{bmatrix} \quad (3.12)$$

The stiffness matrix is composed of advection and diffusion matrices, and can be evaluated as:

$$[K] = [K_A(U_i)] + [K_D]$$

$$[K_A(U_i)] = \begin{bmatrix} \sum A_{ii} & 0 & 0 \\ 0 & \sum A_{ii} & 0 \\ 0 & 0 & \sum A_{ii} \end{bmatrix}$$

where $A_{ij} = \int_{\Omega} \rho \phi U_j \frac{\partial \phi^T}{\partial x_i} d\Omega$, and

$$[K_D] = \begin{bmatrix} 2D_{11} + D_{22} + D_{33} & 0 & 0 \\ 0 & D_{11} + 2D_{22} + D_{33} & 0 \\ 0 & 0 & D_{11} + D_{22} + 2D_{33} \end{bmatrix}$$

where $D_{ij} = \int_{\Omega} \mu_T \frac{\partial \phi}{\partial x_j} \frac{\partial \phi^T}{\partial x_i} d\Omega$.

The gradient matrix is given by:

$$[C] = \begin{bmatrix} C_1 \\ C_2 \\ C_3 \end{bmatrix}$$

where $C_i = \int_{\Omega} \frac{\partial \phi}{\partial x_i} \psi^T d\Omega$.

The main advantage of the mixed method is that the velocity and pressure are computed in a coupled manner without any numerical differentiation. But, the matrix system becomes very large and requires a lot of CPU time when Gaussian elimination is employed. Furthermore, the partial pivoting strategy should be used due to the presence of the zeros in the main diagonal, which also necessitates extra workspace and makes implementation inefficient, especially on a vector machine. It is believed that the mixed method is not suitable for large scale problems.

3.5 PENALTY FUNCTION FINITE ELEMENT METHODS

3.5.1 REDUCED INTEGRATION PENALTY (RIP) METHOD

Originally, the penalty function method was formulated on the basis of a minimization problem. For the Navier-Stokes equations, there exists no corresponding functional in a classical sense. Considering first the linear Stokes flow, one may construct a quadratic functional corresponding to the variational eqs. (3.6) and (3.7) as [65,66]:

$$I(U_i, P) = \frac{1}{2} \int_{\Omega} \mu \tau \left(\frac{\partial U_i}{\partial x_j} + \frac{\partial U_j}{\partial x_i} \right) \frac{\partial U_i}{\partial x_j} d\Omega - \int_{\Omega} P \frac{\partial U_i}{\partial x_i} d\Omega - \int_{\Gamma} U_i t_i d\Gamma \quad (3.13)$$

Thus it can be easily recognized that if the continuity equation is treated as a constraint, the negative of the pressure turns out to be a Lagrangian multiplier associated with the constraint. The incompressibility constraint can be alternatively included into the above functional in a least-squares approximation sense [66] using the penalty function method. Introducing a penalty functional corresponding to the constraint as:

$$G(U_i) = \frac{1}{2} \frac{1}{\varepsilon} \int_{\Omega} \left(\frac{\partial U_i}{\partial x_i} \right)^2 d\Omega \quad (3.14)$$

and replacement of the pressure term in eq. (3.13) by this penalty functional results in a modified functional as:

$$I_p(U_i) = \frac{1}{2} \int_{\Omega} [\mu_T (\frac{\partial U_i}{\partial x_j} + \frac{\partial U_j}{\partial x_i}) \frac{\partial U_i}{\partial x_j} + \frac{1}{\varepsilon} (\frac{\partial U_i}{\partial x_i})^2] d\Omega - \int_{\Gamma} U_i t_i d\Gamma \quad (3.15)$$

Thus, the solution to the Stokes equations is recast into the minimization of the modified functional, $I_p(U_i)$, by taking its first variation and setting it to zero:

$$\delta I_p(U_i) = 0 \quad (3.16)$$

Including now the convective term, the weak form for the Navier-Stokes equation can be given by:

$$\int_{\Omega} \{ \delta U_i \rho U_j \frac{\partial U_i}{\partial x_j} + \frac{1}{\varepsilon} \frac{\partial \delta U_i}{\partial x_i} \frac{\partial U_i}{\partial x_i} + \mu_T \frac{\partial \delta U_i}{\partial x_j} (\frac{\partial U_i}{\partial x_j} + \frac{\partial U_j}{\partial x_i}) \} d\Omega = \int_{\Gamma} \delta U_i t_i d\Gamma \quad (3.17)$$

Evaluating integrals within each element, the finite element equation can be written as:

$$([K] + \frac{1}{\varepsilon} [B]) \{U\} = \{F\} \quad (3.18)$$

where $[B] = \int_{\Omega} \frac{\partial \phi^T}{\partial x_i} \frac{\partial \phi}{\partial x_i} d\Omega$.

The choice of penalty parameter, ε , requires special attention. Clearly, ε must be small enough to satisfy incompressibility but it should not cause matrix ill-conditioning due to round-off errors which could lead to a trivial solution. It is recommended [66,72] that the values of penalty parameter be chosen that

$$\frac{1}{\varepsilon} = c\mu \quad (3.19)$$

where c is a constant which depends only on the computer word length and is known to be independent of the mesh parameter [72]. The suggested value of c is 10^6 for floating-point word length of 60 to 64 bits.

Even with a sufficiently small value of ε , the penalty term dominates the nonpenalty terms, and this leads to a trivial solution. To circumvent this difficulty, so-called “reduced integration” was introduced [64,65,74] in the evaluation of the penalty matrices. The ingredient of this trick is to make penalty matrices singular, so that they are not invertible but make the total matrix invertible [65,66]. As a simple example, when the linear rectangular element is used, 2×2 Gaussian quadrature rule is used for evaluation of nonpenalty terms with 1×1 Gaussian quadrature for penalty terms.

Note that the pressure is eliminated without the discretization of the continuity equation. The only unknowns are the velocity components, which results in tremendous computational savings, especially in 3-D cases. Furthermore, no partial pivoting is necessary, which makes the direct application of the active column (profile, or envelope) solver possible. Once the velocity field is obtained by solving eq. (3.18), the pressure may be recovered by [65,66]:

$$-P = \frac{1}{\varepsilon} \frac{\partial U_i}{\partial x_i} \quad (3.20)$$

which is evaluated at the Gauss points in each element. Indeed, there is no introduction of interpolation functions for pressure in the RIP method, and this results in piecewise constant or piecewise discontinuous pressure approximations. The pressure computed by eq. (3.20) may suffer from spurious modes or checkerboard modes [78,79]. These spurious modes indicate that the system is overdetermined. Also, the reduced integration can sometimes generate inaccurate results when using distorted isoparametric elements [73]. This last point is critical because most of the realistic

engineering computations inevitably employ highly distorted elements to describe the complex geometry.

3.5.2 CONSISTENT PENALTY METHOD

One penalty method which circumvented the above mentioned difficulty was suggested in Refs. [65,73,78,79], whose main idea is to introduce interpolation functions for pressure explicitly and discretize the continuity equation before the pressure is eliminated. This method is called the consistent construction of the penalty matrix, and the weak form of the continuity equation is given by:

$$\int_{\Omega} \delta P \frac{\partial U_i}{\partial x_i} d\Omega = -\varepsilon \int_{\Omega} (\delta P) P d\Omega \quad (3.21)$$

And the finite element formulation is given by:

$$\int_{\Omega} \psi \frac{\partial \phi^T}{\partial x_i} d\Omega U_i = -\varepsilon \int_{\Omega} \psi \psi^T d\Omega P \quad (3.22)$$

Thus, the discretized momentum equation and the incompressibility condition can be written at the elemental level as:

$$[K]\{U\} - [C]\{P\} = \{F\} \quad (3.23)$$

$$[M_p]\{P\} = -\frac{1}{\varepsilon} [C]^T \{U\} \quad (3.24)$$

where $[M_p] = \int_{\Omega} \psi \psi^T d\Omega$.

Using eq. (3.24), the pressure can be eliminated from eq. (3.23) by static condensation, and the resulting matrix system has the following form:

$$([K] + \frac{1}{\epsilon} [K_p])\{U\} = \{F\} \quad (3.25)$$

where $[K_p] = [C][M_p]^{-1}[C]^T$.

It should be noted that the elimination of pressure at the elemental level is not possible with the standard conforming mixed method [65]. Again, the computation of the velocity and pressure is decoupled, and the consistent penalty method enjoys all the advantages of RIP method over its mixed counterpart while its formulations are equivalent to the latter. Comparing eqs. (3.18) and (3.25), both expressions are identical when $[M_p]$ is a diagonal matrix with a constant diagonal. Since the pressure approximations are explicitly introduced, full quadrature is used to evaluate the penalty matrices.

3.6 APPROXIMATION FUNCTIONS

As indicated in section 3.1, the choice of approximation functions for velocity and pressure is important for the stable and convergent solution in both mixed and penalty methods. In 2-D problems, a 9-noded biquadratic velocity-linear pressure ($Q_2^9 - P_1$) element is second-order accurate and is known to be optimal [65]. Recently, a restricted 8-noded biquadratic velocity-constant pressure ($R_2^8 - P_0$) element was suggested in Ref. [75]. This element also satisfies the BB condition, and it is found to be a reliable element free from spurious pressure modes on a regular mesh. In 3-D problems, the 27 noded

full, triquadratic velocity-linear pressure ($Q_2^{(27)} - P_1$) element is also second-order accurate and, probably the most accurate one free of pressure modes. But, due to its high cost, several new 3-D elements are suggested in Ref. [75]. Among them, the most cost-effective one which satisfies the BB condition may be the enriched trilinear velocity-constant pressure ($Q_1^+ - P_0$) element which is first-order accurate. However, this element has 14 nodal points, and the total number of degrees of freedom is approximately double with respect to the simplest 8-noded trilinear velocity-constant pressure ($Q_1^{(8)} - P_0$) element. Even though this element does not satisfy the BB condition and may sometimes suffer from spurious pressure modes, these can be all filterable, at least when pure, on the regular mesh [78,79]. Thus, the isoparametric ($Q_1^{(8)} - P_0$) elements are employed in the present study to minimize the work space. The pressure is computed only at the centroid point, which achieved filtered pressures [73,79]. No other pressure mode was observed in the present computations.

Chapter IV

COMPUTATIONAL DETAILS

4.1 NONDIMENSIONALIZATION

Since the Navier-Stokes equation in a dimensionless form facilitates generalization to a large range of problems [57], the following nondimensionalization is performed before computation.

Let L_{ref} , U_{∞} , and ρU_{∞}^2 denote the characteristic reference magnitudes,

$$x_i^* = \frac{x_i}{L_{ref}}, \quad i = 1,2,3 \quad (4.1)$$

$$U_i^* = \frac{U_i}{U_{ref}}, \quad i = 1,2,3 \quad (4.2)$$

$$P^* = \frac{(P - P_{ref})}{\rho_{ref} U_{ref}^2} \quad (4.3)$$

$$\mu_T^* = \frac{\mu_T}{\rho_{ref} U_{ref}} \quad (4.4)$$

$$\rho^* = \frac{\rho}{\rho_{ref}} = 1 \quad (4.5)$$

The nondimensionalization is important especially from the numerical point of view. The proper choice of reference values can avoid matrix ill-conditioning. The velocity U_∞ was taken as U_{ref} in all cases. The diameter D_j was taken as L_{ref} for a circular jet case, and the streamwise length of the nozzle, L , was taken as L_{ref} for rectangular jet(s) cases. It should be noted that both circular and rectangular nozzles have the same area so that the diameter of the same area circle, D_{eq} , of the rectangular nozzle is equal to D_j . Such values are consistent with those in the measurements of Ref. [80] where $0.6 \times L = D_j = D_{eq} = 2 \text{ inch}$, and this choice is believed to provide meaningful comparison of the flow injected from circular- and rectangular- nozzle(s).

4.2 COMPUTATION DOMAIN AND MESH DISTRIBUTION

Since the flow is symmetric with respect to the xz plane passing through the jet nozzle, only half of the flowfield was considered for single jet cases. For the dual jet case, the center of the nozzle spacing served as the plane of flow symmetry. All the origins of the reference frame were taken at the center of the jet nozzle, and the whole computation domain comprises a box shape.

The determination of the size of the computation domain and the preparation of mesh need very special care, since the flow is unbounded and there exist very steep velocity- and pressure-gradient near the nozzle. Due to the limitation of the computer resources, the following trial-and-error steps were used to determine the final domain and mesh with the aid of the previous computational studies [24,25,34] and experimental studies [11,12,13,14,45], as:

1. The upstream, downstream, and farfield boundaries are taken at the estimated locations where $|C_{p, measured}| \leq 0.2$. For multiple and/or non-circular jet cases without any prior information, single, circular jet data can be used for a crude first guess.
2. The top boundary is taken near the estimated jet penetration corresponding to the downstream boundary location. For the circular jet case, there exist numerous empirical relations for the trajectory [10,11,12], as given in eq. (1.1). For the rectangular jet(s) there exists little information on the jet properties including trajectory, but, from the measured velocity vectors in Ref. [45], the location where the jet velocity starts to decay rapidly is taken as the top boundary.
3. In order to check the adequacy of the size of computation domain, a pseudo-laminar calculation with eddy viscosity value obtained with eq. (2.2) is performed on a coarse mesh. Since this value is high, and the resulting turbulent Reynolds number is less than 100, it requires less than 10 successive substitutions to reach relative changes in velocity less than 1%. The steps 1 to 3 are repeated until the result is reasonable compared to the other data.

4. Using the coarse mesh result and empirical information, the finite element mesh is re-arranged. Usually, the mesh is mostly clustered near the locations of steep gradients near the jet nozzle and the zone of maximum deflection.
5. Another pseudo-laminar calculation but with refined mesh is performed in the same way as in step 3. This calculation is costly and need not continue to reach full convergence. The present author's experience is that three or four iterations are enough to check the surface pressure distribution. Also, steps 4 to 5 can be repeated until a satisfactory result is obtained.

The details of the final size of domain along with mesh distribution are given in Table 1.

Since the circular jet case has long been studied and the flowfield is fairly well known, there were little difficulties to reach the final mesh. However, the experimental studies on the rectangular jet(s) [41,45] reveal that its flowfield is more complicated, and the negative pressure peaks occur at the front corners and negative pressure zone occupies a wider area. Since the main concern of this study is the surface pressure, more nodal points were distributed in the transverse (y) direction than the normal (z) direction.

4.3 BOUNDARY CONDITIONS

Specification of the boundary conditions are closely related to the domain and mesh. After careful examination of the various conditions, the following sets of conditions were

found to be adequate for the purposes of the present study. The same types of boundary conditions were used in all cases:

1. Upstream boundary at $x' = X_u$:

$$U^* = 1, \quad V^* = W^* = 0$$

2. Downstream boundary at $x' = X_d$:

$$t_x^* = t_y^* = t_z^* = 0$$

3. Bottom boundary at $z' = 0$:

- a. Bottom wall except for the jet nozzle:

$$t_x^* = t_y^* = W^* = 0$$

- b. Nozzle exit:

$$U^* = V^* = 0, \quad W^* = R$$

- c. Nozzle edge:

$$U^* = V^* = W^* = 0$$

4. Top boundary at $z' = Z$:

$$t_x^* = t_y^* = t_z^* = 0$$

5. Plane of symmetry at $y' = 0$:

$$t_x^* = V^* = t_z^* = 0$$

6. Side boundary at $y^* = Y$:

$$t_x^* = t_y^* = t_z^* = 0$$

The downstream boundary was regarded as an outflow boundary, and the traction-free condition [77] was used. The far field boundaries, i.e. top surface and side surface, were not so far from the injection nozzle as to specify uniform freestream velocity [25] or zero normal velocity and zero tangential velocity gradients [34]. Physically, these surfaces should allow mass entrainment across the boundary, and the specification of traction-free conditions on the far-field boundaries was found to be effective for this purpose.

The bottom wall was modeled as a slip surface which was similar to the approach used in Ref. [34]. This will not produce an accurate picture of the flow in the near wall region, but may be a useful approximation when the details of the boundary layer are not the major concern [81]. That is the case here when the main jet flowfield and the wall pressure distribution are the desired outcome. Recall that $\partial p / \partial n \cong 0$ across a boundary layer [57].

4.4 SOLUTION STRATEGY

The final system of algebraic equation resulting from the penalty FEM has the following nonlinear form:

$$[K(U)]\{U\} = \{F\} \quad (4.6)$$

where $[K(U)]$ is the global stiffness matrix, $\{U\}$ is the unknown velocity vector, and $\{F\}$ is the global vector of body force and the boundary conditions. Due to the highly complicated flow pattern, direct iteration (successive substitution) with under-relaxation was employed starting from a pseudo-laminar solution. Nonlinear iterations were continued until the relative changes in the velocity and force become less than 1%. The eddy viscosity distribution was updated at every iteration using the current meanflow field. The resulting system of equations was unsymmetric, sparse, and very large, but no pivoting was necessary and direct application of the profile solver was possible. The computation was done using a modified version of the general purpose finite element code FIDAP [82] on the Virginia Tech IBM 3090 machine with vector facility. The program was compiled with a FORTVS2 compiler with optimization level(3) and vector level(2) supported by IBM Engineering and Scientific Subroutine Library (ESSL). Details of the statistics of computation are given in Table 1.

It may be informative to investigate the computational savings from the use of the vector processor. Since most of CPU time for the steady-state finite element calculation is exhausted at the Gaussian elimination stage, comparison of this quantity is helpful. It is well known that the number of operations for the Gaussian elimination process is approximately proportional to the cube of the number of equations when this becomes very large. This may be applied to the sparse, banded matrix case with skyline storage mode, and an empirical relation for the CPU sec in 1 LU process given in [54] as:

$$T - LU = constant \times MINB^2 \times NEQN \quad CPU \text{ sec} \quad (4.7)$$

where the *constant* was 2.6×10^{-6} when NEQN was 10,557 and the FORTRAN-H extended compiler with optimization level (1) was used on Virginia Tech IBM-3081

machine in Ref. [54]. For the present computation, the *constant* corresponding to NEQN of 11,807 is found to be 9.02×10^{-8} , which is 1/29 of the previous one. The saving achieved here is an accumulative result due to the change of machine from IBM-3081 to 3090, and the change of compiler from FORTHX to FORTVS2. A small benchmark test (NEQN of 9,757) reveals that the scalar-to-vector CPU ratio is about 2.84, where the FORTVS2 compiler with optimization level (2) was used for the scalar computation.

Table 1. Display of Computational Statistics

	Single Circ.	Single Rect.	Dual Rect. coarse mesh	Dual Rect. fine mesh
Reference Length	D_j	L	L	L
Upstream X_u	-2.5	-1.5	-1.5	-1.5
Downstream X_d	8.0	3.0	3.5	3.0
Side boundary Y	4.0	2.5	2.0	2.0
Top boundary Z	6.0	2.0	3.0	3.0
FE mesh NXxNYxNZ	30x12x12	25x15x12	25x20x12	30x20x15
No. of node points NNOD	4,320	4,500	6,000	9,000
No. of elements NELM	3,509	3,696	5,016	7,714
No. of active eqs. NEQN	11,807	12,267	16,458	24,975
Matrix elements NMAT	10,144,411	13,117,355	22,860,528	43,825,147
Half-bandwidth MINB (Mean)	430	535	695	877
Half-bandwidth MAXB (Max.)	449	563	729	915
CPU sec for 1 LU T-LU	197	292	657	1,673

Chapter V

RESULTS AND DISCUSSION

5.1 PRESENTAION OF RESULTS

The current study performed computations on the following three problems.

Problem 1: Single Circular Jet in a Crossflow at $R = 4$

Problem 2: Single Rectangular Jet in a Crossflow at $R = 4$

Problem 3: Dual (Side-by-Side) Rectangular Jets in a Crossflow at $R = 4$ with a coarse and a fine mesh

Various jet properties computed for problem 1 are compared to a number of available experimental data. Trajectory and axial velocity decay predictions for problem 3 are compared to the measured data of Ref. [80].

The predicted mean flowfield (velocity components) and contours of the surface pressure coefficient defined by $C_p \equiv (P - P_\infty) / (\frac{1}{2} \rho U_\infty^2)$ for problems 1 and 3, are compared with the measurements of Ref. [80], since that experimental study covered a wide region and used highly dense wall pressure instrumentation in the vicinity of the jet nozzles. This can be recognized from Figs. 5, 33, and 37 where comparisons of the finite element mesh used here and the pressure tap locations from Ref. [80] are given. In the wall C_p isobar plots, the range covers from -2.0 (-3.0 for dual jets) to 1.0 by 0.2, but this does not mean that the maximum and minimum levels are limited to these values. No mean flow data is available for problem 2, and the surface pressure is compared with that reported in Ref. [80].

As stated before, the surface pressure prediction has been hardly reported in previous Navier-Stokes analyses. Recently, Ref. [83] quoted a comparison of computed and measured surface pressure contours at $R = 2.3$ given by J.J. McGuirk in an unpublished note. The agreement was similar to those achieved by the well correlated inviscid flow calculations. This is the only prior viscous pressure prediction for the circular jet in a crossflow problem known to this author.

5.2 SINGLE CIRCULAR JET IN A CROSSFLOW AT

$$***R = 4***$$

A comparison between the finite element mesh used here and the pressure tap locations used in Ref. [80] for this problem is given in Fig. 5.

The computed trajectory is compared with previous experimental results [9,12,13,80] with satisfactory agreement in Fig. 6. It should be noted that even the measured trajectories show appreciable differences according to the experimental conditions, such as jet exit velocity profile, turbulence level, or crossflow properties. The data of Ref. [13] indicates a somewhat higher trajectory, while the high turbulence case in Ref. [80] shows lower trajectory.

The vortex curve prediction is compared with the data of Ref. [16] whose data are available from $x/D_j \cong 2$ in Fig. 7. The present computation is in better agreement far downstream, and this may be due to the approaching of the vortex axis to the crossflow direction in this region. The measurement of Ref. [16] aligned a rake of probes exactly perpendicular to the vortex axis, while the computed curve was taken in the yz plane. This may be a reason for the initial under-estimation of the vortex curve.

The predicted jet shape defined by half-velocity points is compared with data of Ref. [13] in Fig. 8. Even though the prediction shows more deflection, the overall behavior is well reproduced. The main reason for this discrepancy may be due to the way of measuring the half-velocity points, i.e. the probe in Ref. [13] was traversed along the z axis for a given x location while the present computation took the opposite sense.

The axial velocity decay along the arc length of the jet axis is compared with measured data of Ref. [11-13] in Fig. 9. The prediction shows a slightly faster decay, but it generally compares well with various data. The location of the end of the potential core seems to be near the observed beginning of rapid velocity decay, $2 \leq \xi/D_j \leq 3$.

The calculated length scale in Fig. 10 is found to increase monotonically from a very small value in the core region to about half a nozzle diameter at the beginning of vortex zone. The predicted eddy viscosity distribution in Fig. 11 shows a peak at $\xi/D_j \cong 2.5$.

Surface pressure contours are compared with the measured data of Ref. [80] in Fig. 12, and the current calculation is shown to predict the important features of the overall

pressure pattern quite well, except for the wake region right behind the nozzle. The agreement here is comparable to that achieved by well-tuned, empirical/inviscid flow solutions [6], and both failed to predict the accurate picture in the wake region. This may be due to the existence of a large separated region downstream of the jet.

Figure 13 illustrates the comparison of predicted and measured velocity vector plots on the plane of symmetry passing through the jet nozzle. Detailed comparison of velocity profiles along the normal coordinate at successive downstream locations are given in Figs. 14 to 25.

Figures 14 to 19 present streamwise velocity profile comparisons, and the overall observation is that the use of slip condition on the wall affected the profiles within one or two jet diameter above the wall, but is not critical to simulation of the main jet flow field. Importantly, the computation predicts well the location and magnitude of the velocity peaks in spite of the complicated flow structure.

Figures 20 to 25 present normal velocity profile comparisons, and at the first two locations near the nozzle the agreement is not so good, but the agreement at the rest of the stations is excellent. The double peaks of the profile are predicted quite accurately, and the near wall region is well simulated.

Figure 26 illustrates the comparison of predicted and measured velocity vector plots on the transverse plane at one jet diameter downstream from the jet nozzle. Detailed comparison of velocity profiles along the normal coordinate at the two transverse locations are given in Figs. 27 to 30.

Figures 27 to 28 present transverse velocity profile comparisons, and even though the velocity peaks are slightly under-estimated, good agreement is achieved. Figures 29 to 30 show normal velocity profile comparisons, and the prediction is not so good for the first location, but shows better agreement with a lesser peak velocity at the next location.

Figures 31 to 32 give the predicted velocity vectors on horizontal planes starting from the wall to three jet diameter above the wall. According to these plots, it can be observed that the vortices are generated right behind the circular nozzle and grow due to the entrainment from the crossflow. At some distance from the nozzle ($z/D \cong 1.5$), the vortices start to tilt and are convected with the crossflow.

5.3 SINGLE RECTANGULAR JET IN A CROSSFLOW AT $R = 4$

A comparison between the finite element mesh used here and the pressure tap locations used in Ref. [80] is given in Fig. 33. Since no measured mean flow data are available for this case, only the predicted pressure coefficient is compared with the data of Ref. [80] in Fig. 34. The overall pattern is well predicted. The appearance of the negative peaks near the front corner of the nozzle is apparent. The agreement for this presumably more complicated case seems even better than that for the circular jet case, and this may be due to a lessened blockage effect and, thereby, a reduced wake zone.

Figures 35 to 36 present the predicted velocity vectors on horizontal planes starting from the wall to three equivalent jet diameters above the wall. Unlike the circular jet case, the vortices are found to be created at the front corner of the nozzle. Also, several small vortices appear downstream of the front vortex pair on the nozzle plane, but they seem to interact mutually to agglomerate into a larger one downstream.

5.4 DUAL RECTANGULAR JETS IN A CROSSFLOW

AT $R = 4$

A comparison between the finite element mesh (fine mesh) used here and the pressure tap locations used in Ref. [80] is given in Fig. 37.

The trajectory comparison in Fig. 38 reveals that both coarse- and fine-mesh calculations show a drift in the initial region and higher penetration in the zone of deflection, even though the fine mesh case provides a fairly good prediction. The main reasons for the higher penetration may be due to the relatively lower location of the top boundary and the associated traction-free conditions. Also, further refinement of the mesh will improve the situation, although that would be costly.

The axial velocity decay along the arc length of the jet axis is compared in Fig. 39, where the fine mesh calculation shows slightly better agreement. Experimental result for square free jet given in Ref. [63] is also illustrated together for a qualitative comparison, and the present flow shows much faster decay due to the action of the crosswind as in the circular jet case.

Surface pressure contours are compared with measured data of Ref. [80] in Fig. 40 (a) and (b), and the agreement looks excellent for both cases. The coarse mesh solution shows slightly better prediction at the far downstream region and the fine mesh solution provides better resolution near the nozzle. The computed results clearly predict not only the negative peaks at the front corner, but the second negative zone at the rear which does not appear at the single rectangular jet case. This difference may be due to the jet interaction which locally isolate the region between the nozzles and does not allow high

transverse entrainment velocity. Further study should be followed on this matter, however, the surface pressure pattern between the nozzles is well reproduced.

Figure 41 illustrates the comparison of predicted and measured velocity vector plots on the plane of nozzle symmetry. Wiggles in the velocity occur upstream near wall regions, and these are believed to be due to the locally high Reynolds number and very steep velocity gradient in front of the jet nozzle. This phenomenon is a natural consequence of using standard Galerkin technique which leads to a centered-difference-like treatment of the convective terms [84]. As discussed in Sec. 1.3, upwind-like method may be useful to suppress these wiggles, but it can be accurate only on a very fine mesh where the artificial diffusion is significantly less than the physical diffusion. Further, since the wiggles occur in a limited regions of lesser importance, no special treatment to smooth out the wiggles are tried. Detailed comparison of velocity profiles along the normal coordinate at successive downstream locations are given in Figs. 42 to 51.

Figures 42 to 46 show streamwise velocity profile comparisons, and the general agreement of these results is good with the fine mesh and the velocity peaks are predicted reasonably for both meshes. Figures 47 to 51 present the predicted and measured normal velocity profiles along the normal coordinate at successive downstream locations on the plane of nozzle symmetry. It is observed that the computation slightly under-predicts in the near wall region, while it slightly over-predicts as one goes to the top boundary. The fine mesh calculation provides a slightly better prediction.

Figure 52 shows a comparison of predicted and measured velocity vector plots on the plane of flow symmetry. Recall that the plane of flow symmetry here is defined as midway between the two nozzles. Detailed comparisons of velocity profiles along the normal coordinate at successive downstream locations are given in Figs. 53 to 64. Figures 53 to 58 present the streamwise velocity profile comparisons, and the agreement

looks better than that achieved on the plane of nozzle symmetry. Also, the velocity peaks are well predicted. Figures 59 to 64 show normal velocity profile comparisons, and the agreement is good for the near wall region, while it becomes worse near the top boundary. In this plane, the effect of mesh refinement looks minimal.

Figure 65 illustrates the comparison of predicted and measured velocity vector plots on the transverse plane passing through the jet nozzle. It can be seen that the streamwise counter-rotating vortices with different strength dominate the flowfield. Detailed comparison of velocity profiles along the normal coordinate at the six transverse locations are given in Figs. 66 to 77. Figures 66 to 71 give the transverse velocity profile comparisons, and the agreement becomes better as one goes far from the nozzle. Under-prediction of velocity peaks is observed at the innermost two locations. Figures 72 to 77 present normal velocity profile comparisons, and the velocity peaks are slightly under-predicted, while the prediction of the locations of the peaks is reasonable. It is observed that the fine mesh provides better predictions.

Figure 78 displays the comparison of predicted and measured velocity vector plots on the transverse plane at one jet diameter downstream from the jet nozzle center. Comparing to the case at the previous location ($x/D = 0.0$), the inner streamwise vortex seems to remain at the similar size, while the outer one looks much bigger. As discussed earlier, the inner one looks isolated and the overall flowfield is dominated by the outer vortex. Detailed comparisons of velocity profiles along the normal coordinate at the six transverse locations are given in Figs. 79 to 90. Figures 79 to 84 present transverse velocity profile comparisons, and the overall agreement is good. Figures 85 to 90 show normal velocity profile comparisons. It is observed that the fine mesh solution is consistently in better agreement with measured data, especially for the region where the multiple peaks of the velocity profile occur.

Figures 91 to 92 give the predicted velocity vectors on horizontal planes starting from the wall to three equivalent jet diameters above the wall. The most striking feature is that the asymmetric vortices are generated at each front corner and the inner one is rapidly absorbed into the outer one of greater size, which results in a larger wake zone compared to the single jet case. The role of these front vortices seems to shield the rear part of the jet from the upstream to allow higher penetration, and resulting penetration distribution forms a right triangular shape, as can be seen in Fig. 41. Therefore, the associated entrainment rate is expected to vary along the streamwise length of the rectangular nozzle, and this process may result in much different flow field and surface pressure pattern from the circular jet case.

Chapter VI

CONCLUSIONS AND SUGGESTIONS

6.1 SUMMARY OF CONCLUSIONS

This study has tried to develop reliable and cost-effective numerical techniques to predict the mean flowfield and surface pressure induced by 3-D, turbulent jets in a crossflow at R in the range of 4, and several important results drawn from the computation of three practical problems can be summarized as:

1. Circular Jet

- a. The mean flow velocity predictions were compared with measured data in the plane of symmetry and transverse planes. The agreement is consistently very good except for the near wall region. (The latter is expected due to the purposeful choice of wall boundary conditions.)

- b. The formation of the counter-rotating vortex system was clearly delineated.
- c. The predicted surface pressure was compared with measured data, and the agreement is good in all cases except for the wake region right behind the nozzle. The agreement here is comparable to that achieved by well-correlated empirical/inviscid flow solutions. The major reason for the discrepancy seems to be the large separated zone due to the blockage of crossflow by the jet.

2. Single Rectangular Jet

No mean flow velocity comparison was made due to the lack of measured data for the single rectangular jet in a crossflow. The surface pressure prediction is in an excellent agreement with measured data. Several differences from the circular jet case were found. Previous experimental studies indicate that there is less blockage effect (since this nozzle is aligned streamwise), and, thereby a reduced separated zone. This may be a partial explanation for the enhancement of the agreement of the pressure prediction. From the computed results, it is found that the counter-rotating vortices are generated not from the rear part of the nozzle as in the circular jet case, but from the front corners of the nozzle. They are rapidly lifted up due to the action of the jet fluid injected at the rear part of the nozzle. Therefore, one may not expect a large separated zone at the downstream locations as in the circular jet case.

3. Dual Rectangular Jets

- a. The predicted mean flow velocity profiles were compared with measured data in two vertical planes and two transverse planes. The overall trends are well

predicted, even though there exists some disagreement according to the locations in the plume. The whole flow field is more complicated than that of a single circular jet case due to the interaction of the jets. However, it was found that the mesh refinement can improve the prediction of the velocity field.

- b. The pressure prediction for the same problem is in excellent agreement with the measured data, and this may be due to the same reasons proposed for the single rectangular jet case. Also, some differences at the rear part of the nozzle from the single rectangular jet case are observed, and this is believed to be due to the effect of jet interaction. Finally, the velocity and pressure predictions for rectangular jet(s) performed in this study are the first known to this author.

4. General

- a. The finite element procedures employed in this study are found to be reliable, flexible, and cost-effective for both velocity and pressure predictions. The circular jet nozzle geometry can be more accurately described using isoparametric elements. Wiggles are observed in the regions where the velocity gradient is very steep, and this seems to be a natural consequence of using conventional Galerkin type finite element methods which leads to a centered-difference-like treatment of the advection terms [84]. These are more serious for the rectangular jet(s), since the nozzle is aligned streamwise direction. Since these wiggles are not dominant at essentially all mesh locations and they occur in regions of lesser importance, the wiggle-free solution in the rest of the mesh is probably of acceptable accuracy. Upwind methods may be useful to suppress the wiggles and obtain smooth solutions. However, it should be remembered that the upwinding is accurate only if the numerical diffusion is

significantly less than the physical diffusion, so it can only be used on a very fine mesh [84].

- b. The algebraic turbulence function model is successfully applied to the jet(s) in a crossflow problem. According to the comparisons of the mean velocity profiles, the entrainment process seems to be reasonably modeled. However, for dual jets, further experimental refinement is probably needed including the effect of jet interaction.
- c. The use of a slip condition on the wall introduces measurable effects on the velocity profiles, but these are limited to the near wall region.
- d. The use of traction-free condition on the far-field boundaries is found to handle the mass entrainment or discharge across the boundary effectively, with a modest sized computational region.

6.2 SUGGESTIONS FOR FUTURE WORK

This study is regarded as a starting point towards the practical numerical simulations of complex, 3-D, turbulent flowfield arising from the low-speed jet(s) in a low-speed crossflow. Extension of the current work might include dual jets injected from a flat surface in tandem configurations and jets injected from a body of revolution. Major prior techniques in dealing with tandem jets with inviscid methods are to treat each jet as a single jet and use the jet properties correlated for injection from a flat surface case until both merge into one. Jet-to-jet spacing is another key parameter, and

the turbulence mixing will surely be different from that of single jet case or widely spaced jets. Similar techniques can be used for the body of revolution case, where the jet-to-body diameter ratio varies from a very small value [40] to about one-half [42]. Also, the change of other properties of the jet and crossflow, such as non-uniform jet exit profile, swirl, turbulence, temperature differences, injection angle, and non-uniform crossflow profiles, may be included.

In case the wall plays an important role, the slip condition should be replaced by some alternative means. First of all, the use of fine mesh to resolve the wall region may have to be rejected in 3-D situation on cost grounds. When a very fine, nonuniform mesh is used, typically, the innermost five percent of the flow absorbs about half of the total grid points [85]. For these reasons, it is a common practice to omit the innermost region and to apply artificial boundary conditions at some distance from the wall by solving an approximate momentum equation between the first nodal point and the actual wall to provide a relation between the tangential velocity and its normal derivative [62,86]. However, care should be taken when dealing with complex flows, since the use of these approaches is not valid when a strong adverse pressure gradient exists and the flow separates. Also, previous finite element experience [48-53] with similar techniques in simple, 2-D flows reported that the Newton type solver did not work, and successive substitution with relaxation should be employed to reach convergence. This is an area of controversy and at the same time abundant current research. It is hoped that the current study will serve as a basis for future progress.

REFERENCES

1. Schetz, J.A.: *Injection and Mixing in Turbulent Flow*, Progress in Astronautics and Aeronautics Volume 68, AIAA, New York, 1980.
2. Abramovich, G.N.: *The Theory of Turbulent Jets*, MIT Press, Cambridge, MA, 1960 (English Edition).
3. Shollenberger, C.A.: "Three-Dimensional Wing/Jet Interaction Analysis including Jet Distortion Influences," *Journal of Aircraft*, Vol. 12, No. 9, Sept. 1975, pp. 706-713.
4. Perkins, S.C., Jr. and Mendenhall, M.R.: "A Correlation Method to Predict the Surface Pressure distribution on an Infinite Plate or a Body of Revolution from which a Jet is Issuing," NASA CR-152,345, May 1980.
5. Perkins, S.C. Jr. and Mendenhall, M.R.: "A Study of Real Jet Effects on the Surface Pressure Distribution Induced by a Jet in a Crossflow," NASA CR-166150 (N81-23029), Mar. 1981.
6. Furlong, K.L. and Fearn, R.L.: "A Lifting surface Computer Code with Jet-in-Crossflow Interference Effects," NASA CR-166524, August 1983.
7. Kotansky, D.R.: "Jet Flowfields," AGARD-R-710, 1984.
8. Bradshaw, P., Cebeci, T., Whitelaw, J.H.: *Engineering Calculation Methods for Turbulent Flow*, Academic Press, 1981.
9. Jordinson, R.: "Flow in a Jet Directed Normal to the Wind," ARC R&M 3074, 1956.
10. Pratte, B.D. and Baines, W.D.: "Profiles of the Round Turbulent Jet in a Cross Flow," *Proceedings of ASCE, Journal of the Hydraulics Division*, Nov. 1967, pp. 56-63.

11. Keffer, J.F. and Baines, W.D.: "The Round Turbulent Jet in a Cross Wind," *Journal of Fluid Mechanics*, Vol. 15, 1963, pp. 481-497.
12. Kamotani, Y., and Greber, I.: "Experiments on a Turbulent Jet in Cross-Flow," *AIAA Journal*, Vol. 10, 1972, pp. 1425-1429.
13. Chassaing, P., George, J., Claria, A. and Sananes, F.: "Physical Characteristics of Subsonic Jets in a Cross-Stream," *Journal of Fluid Mechanics*, Vol. 62, 1974, pp. 41-64.
14. Moussa, Z.M., Trischka, J.W., and Eskinazi, S.: "The Near Field in the Mixing of a Round Jet with a Cross-Stream," *Journal of Fluid Mechanics*, Vol. 80, part 1, 1977, pp. 49-80.
15. Rajaratnam, N.: "Turbulent Jets," *Developments in Water Science 5*, Elsevier Science Publishing Company, New York, 1976.
16. Fearn, R.L., and Weston, R.P.: "Vorticity Associated with a Jet in a Cross-Flow," *AIAA Journal*, Vol. 12, 1974, pp. 1666-1671.
17. Schetz, J.A.: "Hydrodynamics of Jets in Cross Flow," *Encyclopedia of Fluid Mechanics*, Volume 2, Dynamics of Single-Fluid Flows and Mixing, Chap. 16, Gulf Publishing Company, Houston, TX, 1986, pp. 406-429.
18. Demuren, A.O.: "Modeling Jets in Cross Flow," *Encyclopedia of Fluid Mechanics*, Volume 2, Dynamics of Single-Fluid Flows and Mixing, Chap. 17, Gulf Publishing Company, Houston, TX, 1986, pp. 430-465.
19. Campbell, J.F. and Schetz, J.A.: "Analysis of the Injection of a Heated Turbulent Jet into a Cross Flow," NASA TR R-413, Dec. 1973.
20. Campbell, J.F. and Schetz, J.A.: "Flow Properties of Submerged Heated Effluents in a Waterway," *AIAA Journal*, Vol. 11, Feb. 1973, pp. 223-230.
21. Isaac, K.M. and Schetz, J.A.: "Analysis of Multiple Jets in a Cross-Flow," *ASME Journal of Fluids Engineering*, Vol. 104, Dec. 1982, pp. 489-492.
22. Adler, D. and Baron, A.: "Prediction of a Three-Dimensional Circular Turbulent Jet in Crossflow," *AIAA Journal*, Vol. 17, No. 2, Feb. 1979, pp. 168-174.
23. Margaron, R.J.: "Analytical Description of Jet-Wake Cross Sections for a Jet Normal to a Subsonic Free Stream," *Analysis of a Jet in a Subsonic Crosswind*, NASA SP 218, 1969, pp. 131-139.
24. Chien, C.J. and Schetz, J.A.: "Numerical Solution of Three-Dimensional Navier-Stokes Equations with Application to Channel Flows and a Buoyant Jet in a Cross-Flow," *Journal of Applied Mechanics*, Vol. 42, September 1975, pp. 575-579.

25. Patankar, S.V., Basu, D.K., and Alpay, S.A.: "Prediction of the Three Dimensional Velocity Field of a Deflected Turbulent Jet," *Journal of Fluids Engineering, Trans. of ASME*, Vol. 99, 1977, pp. 758-762
26. Tatchel, D.G.: "Convection Processes in Confined Three-Dimensional Boundary Layers," Ph.D. Thesis, Univ. London, 1975.
27. Bergeless, G., Gosman, A.D., and Launder, B.E.: "The Turbulent Jet in a Cross-Stream at Low Injection Rates: A Three-Dimensional Numerical Treatment," Report TF/78/3, Mech. Eng. Dept., Univ. California, Davis, 1978.
28. Rodi, W. and Srivatsa, S.K.: "A Locally Elliptic Calculation Procedure for Three-Dimensional Flows and Its Application to a Jet in a Cross Flow," *Computer Methods in Applied Mechanics and Engineering*, Vol. 23, 1980, pp. 67-83.
29. Baker, A.J., Snyder, P.K., and Orzechowski, J.A.: "Three Dimensional Nearfield Characterization of a VSTOL Jet in Turbulent Crossflow," AIAA Paper 87-0051 presented at AIAA 25th Aerospace Science Meeting, Reno, Nevada, Jan. 12-15, 1987.
30. Snyder, P. and Orloff, K.L.: "Three-Dimensional Laser Doppler Anemometer Measurements of a Jet in a Crossflow," NASA TM-85997, September 1984.
31. White, A.J.: "The Predictions of the Flow and Heat Transfer in the Vicinity of the Jet in Cross Flow," ASME Paper 80-WA/HT-26, 1980.
32. Bergeless, G., Gosman, A.D., and Launder, B.E.: "The Near-Field Character of a Jet Discharged Normal to a Main Stream," *Journal of Heat Transfer*, Aug. 1976, pp. 373-378.
33. Crabb, D., Durao, D.F.G., and Whitelaw J.H.: "A Round Jet Normal to a Crossflow," *Journal of Fluids Engineering, Trans. of ASME*, Vol. 103, 1981, pp. 142-152.
34. Sykes, R.I., Lewellen, W.S., and Parker, S.F.: "On the Vorticity Dynamics of a Turbulent Jet in a Crossflow," *Journal of Fluid Mechanics*, Vol.168, 1986, pp. 393-413.
35. Claus, R.W.: "Analytical Calculation of a Single Jet in Cross-Flow and Comparison with Experiment," AIAA-83-0238, Jan. 1983.
36. Leonard, B.P.: "A Stable and Accurate Convective Modelling Procedure Based on Quadratic Upstream Interpolation," *Computer Methods in Applied Mechanics and Engineering*, Vol. 19, pp. 59-98.
37. Demuren, A.O.: "Numerical Calculations of Steady Three-Dimensional Turbulent Jets in Crossflow," *Computer Methods in Applied Mechanics and Engineering*, Vol. 37, 1983, pp. 309-328.

38. Issa, R.: "Solution of Implicitly Discretized Fluid Flow Equations by Operator-Splitting," Report FS/82/15, Dept. of Mech. Eng., Imperial College, London, 1982.
39. Patankar, S.V. and Spalding, D.B.: "A Calculation Procedure for Heat, Mass and Momentum Transfer in Three-Dimensional Parabolic Flows," *International Journal for Heat and Mass Transfer*, Vol. 15, 1972, pp. 1787-1805.
40. Ousterhout, D.S.: "An Experimental Investigation of a Cold Jet Emitting from a Body of Revolution Into a Subsonic Free Stream," NASA CR-2089, Aug. 1972.
41. Weston, R.P. and Thames, F.C.: "Properties of Aspect Ratio 4.0 Rectangular Jets in a Subsonic Crossflow," *Journal of Aircraft*, Vol. 16, No.10, October 1979, pp. 701-707.
42. Schetz, J.A., Jakubowski, A.K., and Aoyagi, K.: "Jet Trajectories and Surface Pressures Induced on a Body of Revolution with Various Dual Jet Configurations," *AIAA Journal of Aircraft*, Vol. 20, No. 11, Nov. 1983, pp. 975-982.
43. Schetz, J.A., Jakubowski, A.K., and Aoyagi, K.: "Surface Pressures Induced on a Flat Plate with In-Line and Side-by-Side Dual Jet Configurations," *AIAA Journal of Aircraft*, Vol. 21, No. 7, Jul. 1984, pp. 484-490.
44. Moore, C.L. and Schetz, J.A.: "Effects of Nonuniform Velocity Profiles on Dual Jets in a Crossflow," AIAA-85-1674, July 1985.
45. Kavsoglu, M., Schetz, J.A., and Jakubowski, A.K.: "Dual Rectangular Jets From a Flat Plate in a Crossflow," AIAA-86-0477, January 1986.
46. Andreopoulos, J., and Rodi, W.: "Experimental Investigation of Jets in a Crossflow," *Journal of Fluid Mechanics*, 1984, Vol. 138, pp. 93-127.
47. Andreopoulos, J.: "On the Structure of Jets in a Crossflow," *Journal of Fluid Mechanics*, 1985, Vol. 157, pp. 163-197.
48. Taylor, C., Hughes, T.G., and Morgan, K.: "A Numerical Analysis of Turbulent Flow in Pipes," *Computer and Fluids*, Vol. 5, 1977.
49. Taylor, C., Hughes, T.G., and Morgan, K.: "Finite Element Solution of One-Equation Models of Turbulent Flows," *Journal of Computational Physics*, Vol. 29, 1978, pp. 163-172.
50. Taylor, C., Hughes, T.G., and Morgan, K.: "A Finite Element Model of One and Two Equation Models of Turbulent Flow," *Recent Advances in Numerical Methods in Fluids*, Chapter 10, Pineridge Press, 1980.
51. Taylor, C., Thomas, C.E., and Morgan, K.: "Analysis of Turbulent Flow with Separation Using the Finite Element Method," *Computer Techniques in Transient and Turbulent Flow*, Chapter 10, Pineridge Press, 1981.

52. Larock, B.E. and Schamber, D.R.: "Approaches to the Finite Element Solution of Two-Dimensional Turbulent Flows," *Computer Techniques in Transient and Turbulent Flow*, Chapter 9, Pineridge Press, 1981.
53. Schamber, D.R. and Larock, B.E.: "Computational Aspects of Modeling Turbulent Flows by Finite Elements," *Computer Methods in Fluids*, Morgan K. eq al. (eds.), Pentech, London, 1980, pp. 339-361.
54. Pelletier, D.H.: "Finite Element Solution of the Navier-Stokes Equations for 3-D Turbulent Shear Flows," Ph.D. Dissertation, Virginia Polytechnic Institute and State University, VA, 1984.
55. Schetz, J.A., Mallory, D.A., and Pellitier, D.: "Numerical and Experimental Investigation of a Propeller Flowfield With a 3-D Non-Uniform Inflow," AIAA-87-0767, Jan. 1987.
56. Thomas, R.H: "Finite Element Solution of 3D Turbulent Navier-Stokes Equations for Propeller-Driven Slender Bodies," Ph.D. Dissertation, Virginia Polytechnic Institute and State University, VA, 1987.
57. Schlichting, H.: *Boundary Layer Theory*, 7th edition, McGraw-Hill Book Company, 1979.
58. Patrick, M.A.: "Experimental investigation of the mixing and penetration of a round turbulent jet injected perpendicularly into a transverse stream," *Trans. Inst. Chem. Eng.*, Vol. 45, pp. 16-31, 1967.
59. Rajaratnam, N. and Gangadharaiah, T.: "Scales for Circular Jets in Cross-Flow," *Journal of the Hydraulics Division, Proceedings of the ASCE*, Vol. 107, No. HY4, April 1981, pp. 497-500.
60. Launder, B., Morse, A., Rodi, W., and Spalding, D.B.: "Prediction of Free Shear Flows - A Comparison of the Performance of Six Turbulence Models," *Free Turbulent Shear Flows*, NASA CP-321, 1973.
61. Schetz, J.A.: "Some Studies of the Turbulent Wake Problem," *Astonautica Acta*, 1971, Vol. 16, pp. 107-117.
62. Launder, B.E. and Spalding, D.B.: *Lectures in Mathematical Models of Turbulence*, Academic Press, London and New York, 1972.
63. Sforza, P.M., Steiger, M.H., and Trentacoste, N.: "Studies on Three-Dimensional Viscous Jets," *AIAA Journal*, Vol. 4, May 1966, pp. 800-806.
64. Zienkiewicz, O.C.: *The Finite Element Methods*, Third Edition, McGraw-Hill Book Company, 1977.
65. Carey, G. and Oden, S.T.: *Finite Element Methods: A Second Course*, Prentice Hall, 1983.

66. Reddy, J.N.: *An Introduction to the Finite Element Method*, McGraw-Hill Book Company, 1984.
67. Cuvelier, C., Segal, A., and Steenhoven, A.A.: *Finite Element Methods and Navier-Stokes Equations*, D. Reidel Publishing Company, 1986.
68. Olson, M.D.: "Variational-Finite Element Methods for Two-Dimensional and Axisymmetric Navier-Stokes Equations," *Finite Elements in Fluids*, John Wiley&Sons, Vol. 1, 1975, pp. 57-72.
69. Taylor, C. and Hood, P.: "A Numerical Solution of the Navier-Stokes Equation Using the Finite Element Technique," *Computer and Fluids*, Vol. 1, 1973.
70. Gartling, D.K. and Becker, E.B.: "Finite Element Analysis of Viscous Incompressible Fluid Flow, Part 1: Basic Methodology," *Computer Methods in Applied Mechanics and Engineering*, Vol. 8, 1976, pp. 51-60.
71. Gartling, D.K. and Becker, E.B.: "Finite Element Analysis of Viscous Incompressible Fluid Flow, Part 2: Applications," *Computer Methods in Applied Mechanics and Engineering*, Vol. 8, 1976, pp. 127-138.
72. Hughes, T.J.R., Liu, W.K., and Brooks, A.: "Finite Element Analysis of Incompressible Viscous Flows by the Penalty Function Formulation," *Journal of Computational Physics*, Vol. 30, 1979, pp. 1-60.
73. Engelman, M.S., Sani, R.L., Gresho, P.M., and Bercovier M.: "Consistent vs. Reduced Integration Penalty Methods for Incompressible Media Using Several Old and New Elements," *International Journal for Numerical Methods in Fluids*, Vol. 2, 1982, pp. 25-42.
74. Reddy, J.N.: "On Penalty Function Methods in the Finite Element Analysis of Flow Problems," *International Journal for Numerical Methods in Fluids*, Vol. 2, 1982, pp. 151-171.
75. Fortin, M.: "Old and New Finite Elements for Incompressible Flows," *International Journal for Numerical Methods in Fluids*, Vol. 1, 1981, pp. 347-364.
76. Finlayson, B.A.: *The Method of Weighted Residuals and Variational Principles*, Academic Press, 1972.
77. Gresho, P.M., Lee, R.L., and Sani, R.L.: "On the Time-Dependent Solution of the Incompressible Navier-Stokes Equations in Two and Three Dimensions," Lawrence Livermore Report UCRL-83282, September 1979.
78. Sani, R.L., Gresho, P.M., Lee, R.L., and Griffiths, D.F.: "The Cause and Cure (?) of the Spurious Pressures Generated by Certain FEM Solutions of the Incompressible Navier-Stokes Equations: Part 1," *International Journal for Numerical Methods in Fluids*, Vol. 1, 1981, pp. 17-43.

79. Sani, R.L., Gresho, P.M., Lee, R.L., Griffiths, D.F., and Engelman, M.: "The Cause and Cure (?) of the Spurious Pressures Generated by Certain FEM Solutions of the Incompressible Navier-Stokes Equations: Part 2," *International Journal for Numerical Methods in Fluids*, Vol. 1, 1981, pp. 171-204.
80. Kavsoglu, M.S.: "Jets in a Crossflow including the Effects of Dual Arrangements, Angle, Shape, Swirl, and High Turbulence," Ph.D. Dissertation, Virginia Polytechnic Institute and State University, VA, 1986.
81. Roache, P.J.: *Computational Fluid Dynamics*, Hermosa Publishers, 1976.
82. Engelman, M.S.: "FIDAP: A Fluid Dynamics Analysis Program," *Adv. Eng. Soft.*, Vol. 4, 1982.
83. Hancock, G.J.: "A Review of Aerodynamics of Jet in a Cross Flow," *The Aeronautical Journal*, Vol. 91, No. 905, May 1981, pp. 201-213.
84. Gresho, P.M. and Lee, R.L.: "Don't Suppress the Wiggles-They're Telling You Something," *Computer and Fluids*, Vol. 9, 1981, pp. 223-253.
85. Ferziger, J.H.: "Simulation of Incompressible Turbulent Flows," *Journal of Computational Physics*, Vol. 69, 1987, pp. 1-48.
86. Kline, S.J., Cantwell, B., and Lilly, G.M. (eds.): *Complex Turbulent Flows: Comparisons of Computation and Experiment*, Vol. I, II, and III, Stanford University Press, Stanford, CA, 1982.

FIGURES

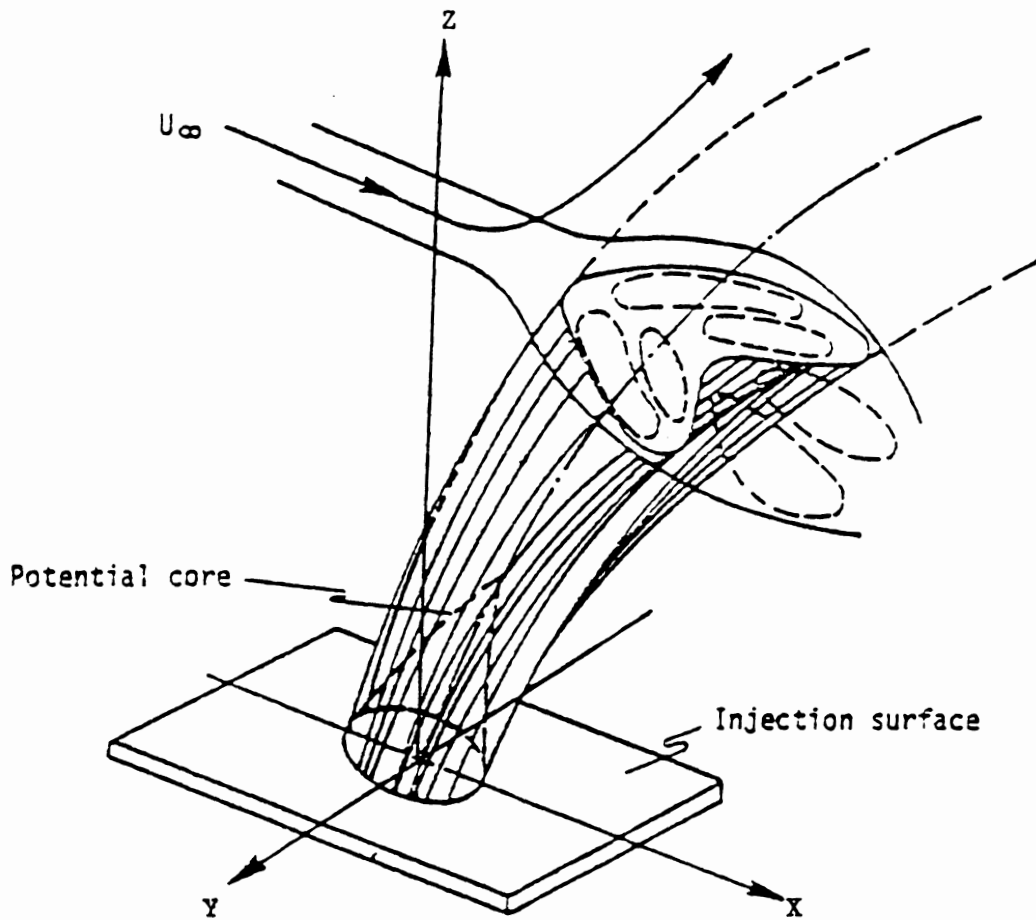


Figure 1. Description of the Flowfield (Ref. 2)

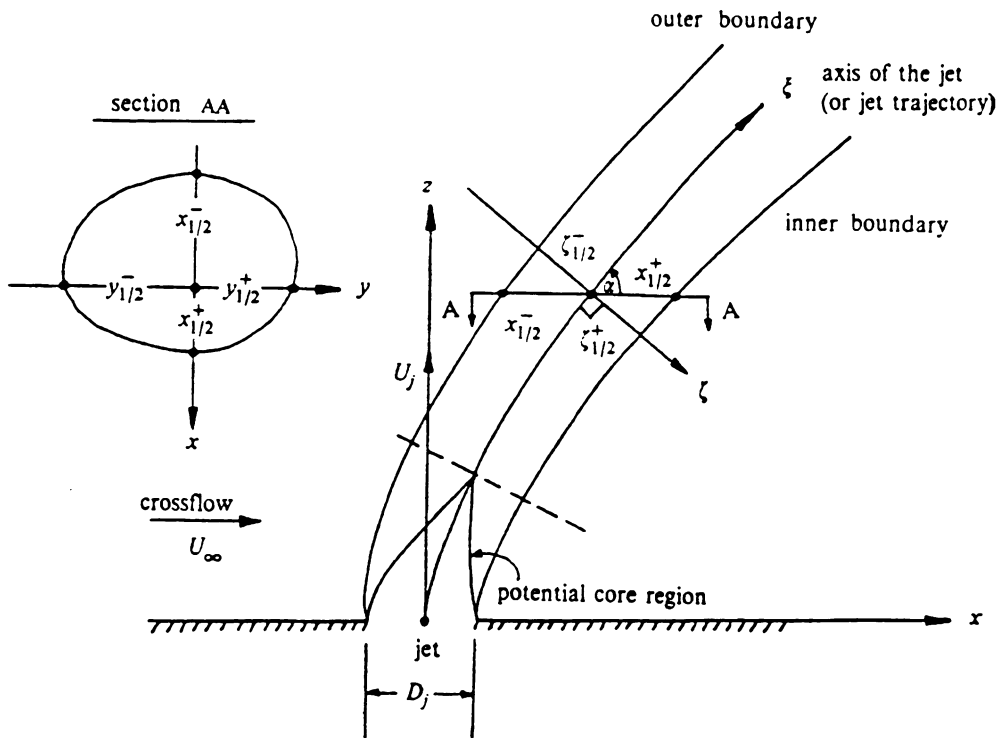


Figure 2. Definition Sketch of a Circular Jet in a Crossflow for Analysis

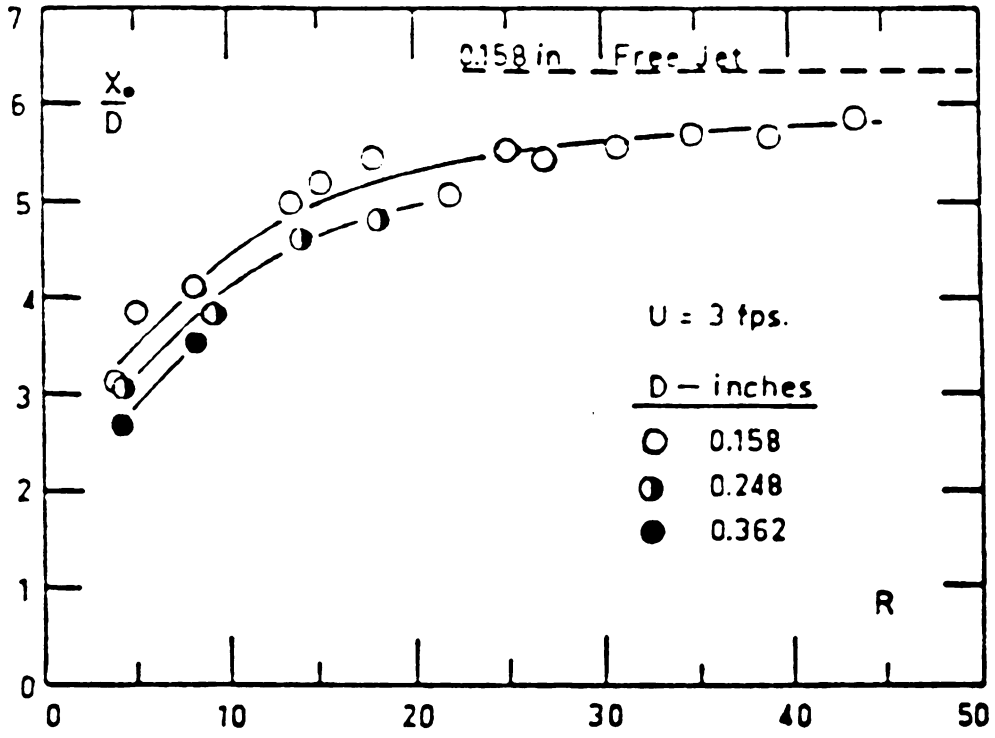


Figure 3. Length of Potential Core (Ref. 6)

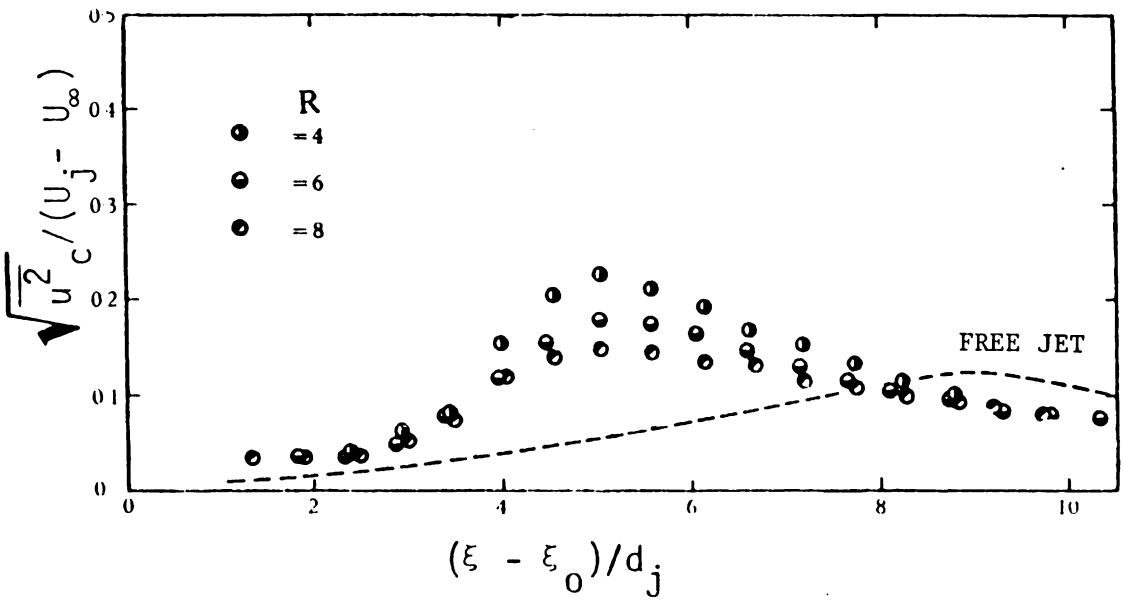


Figure 4. Turbulent Intensity along the Transverse jet (Ref. 7)

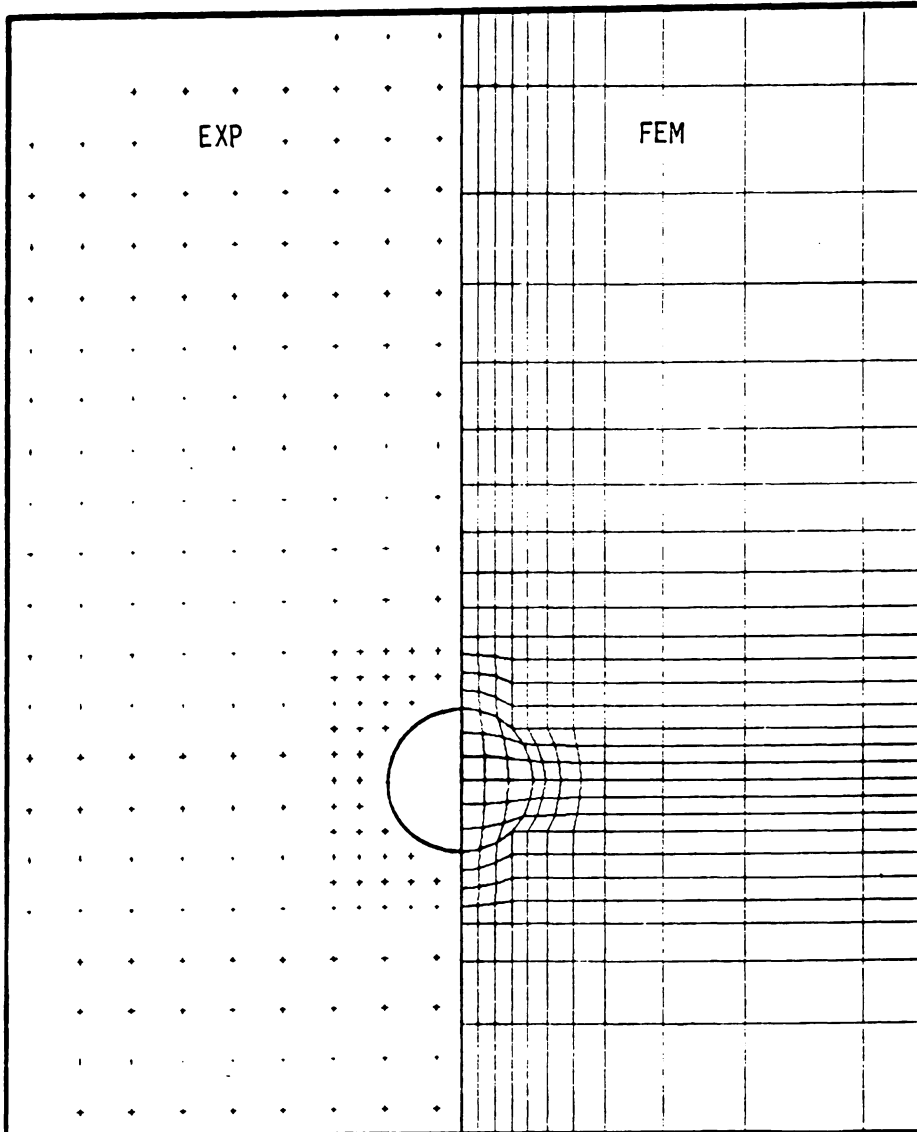


Figure 5. Single circular Jet in a Crossflow at $R=4$: Finite Element Mesh vs. Surface Pressure Tap Locations

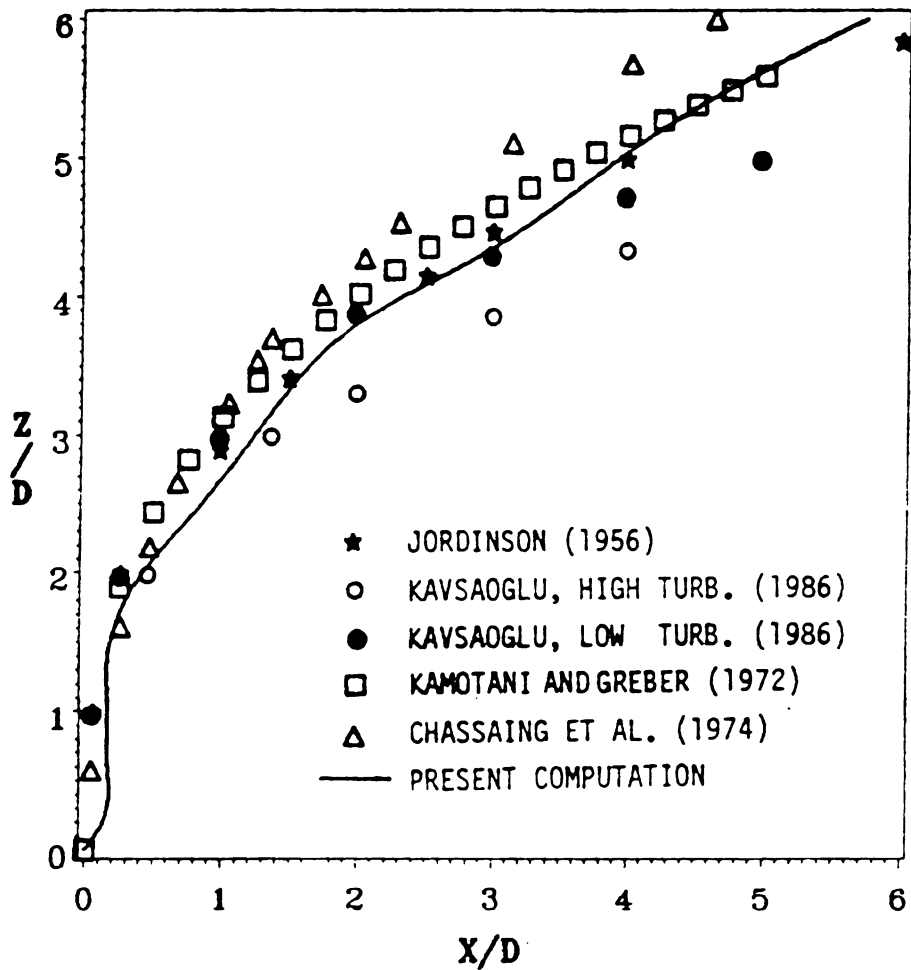


Figure 6. Single Circular Jet in a Crossflow at $R = 4$: Comparison of Jet Trajectory

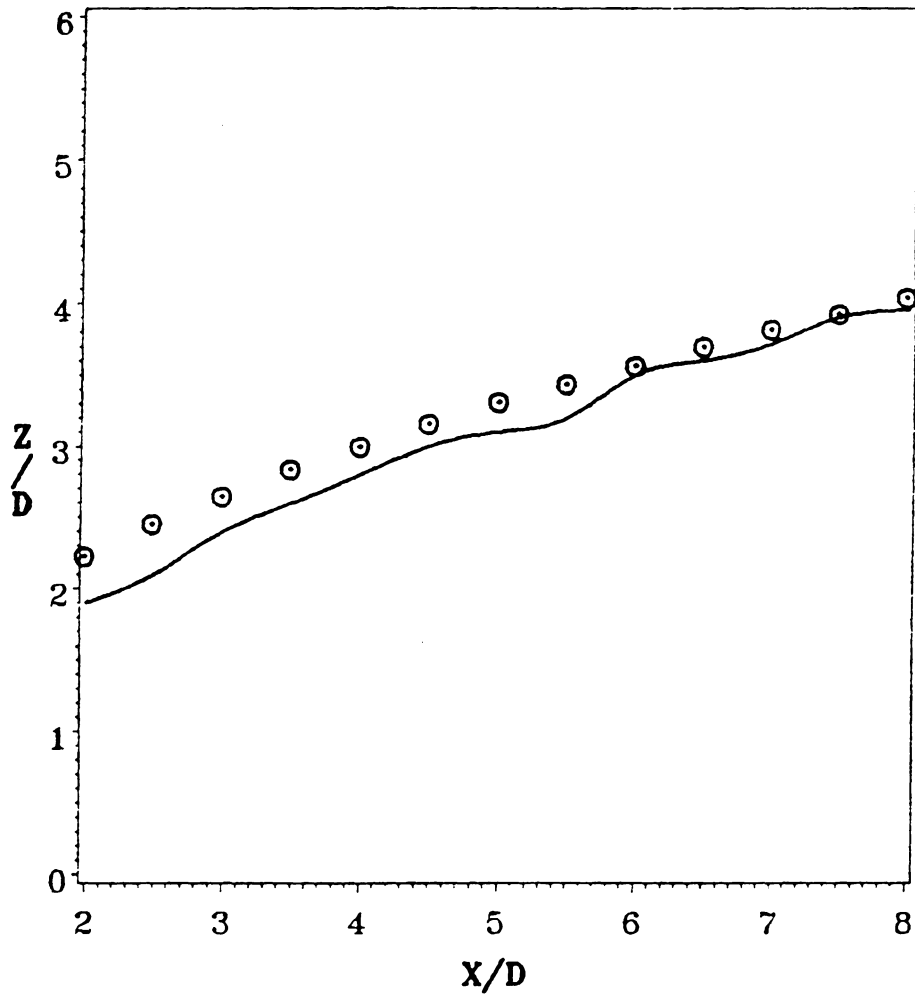


Figure 7. Single Circular Jet in a Crossflow at $R = 4$: Comparison of Vortex Curve

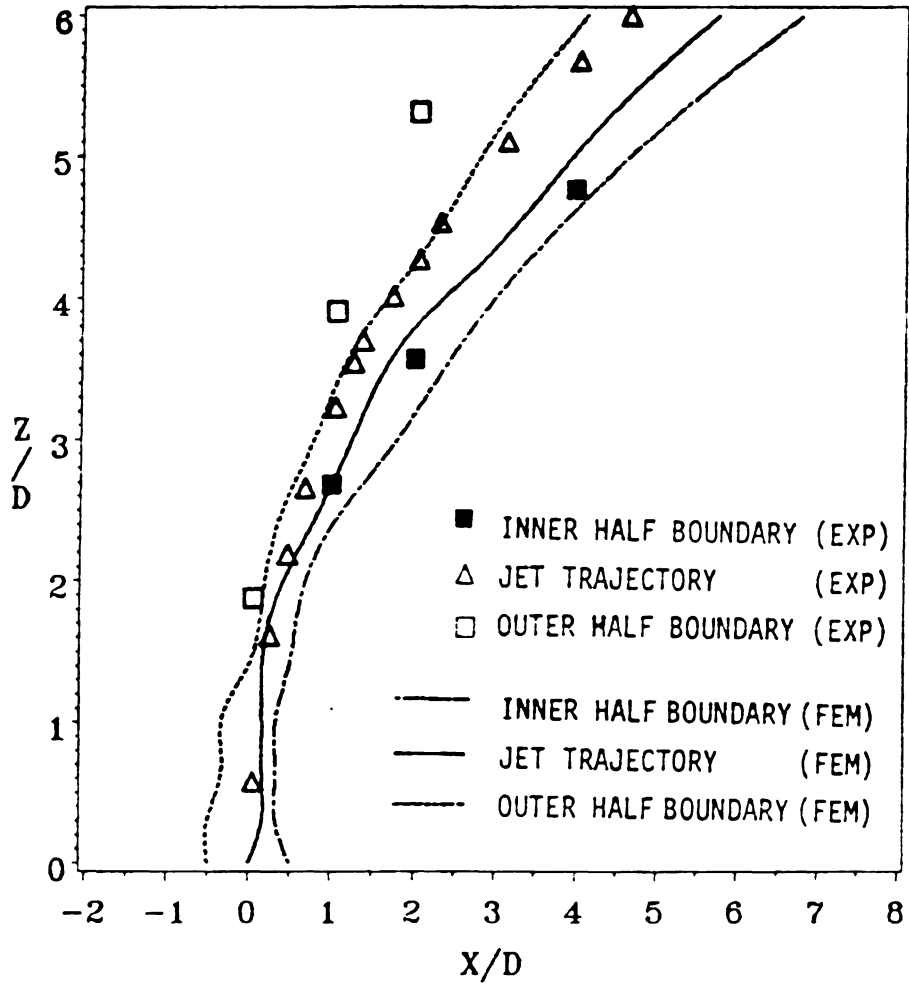


Figure 8. Single Circular Jet in a Crossflow at $R=4$: Comparison of Jet Shape

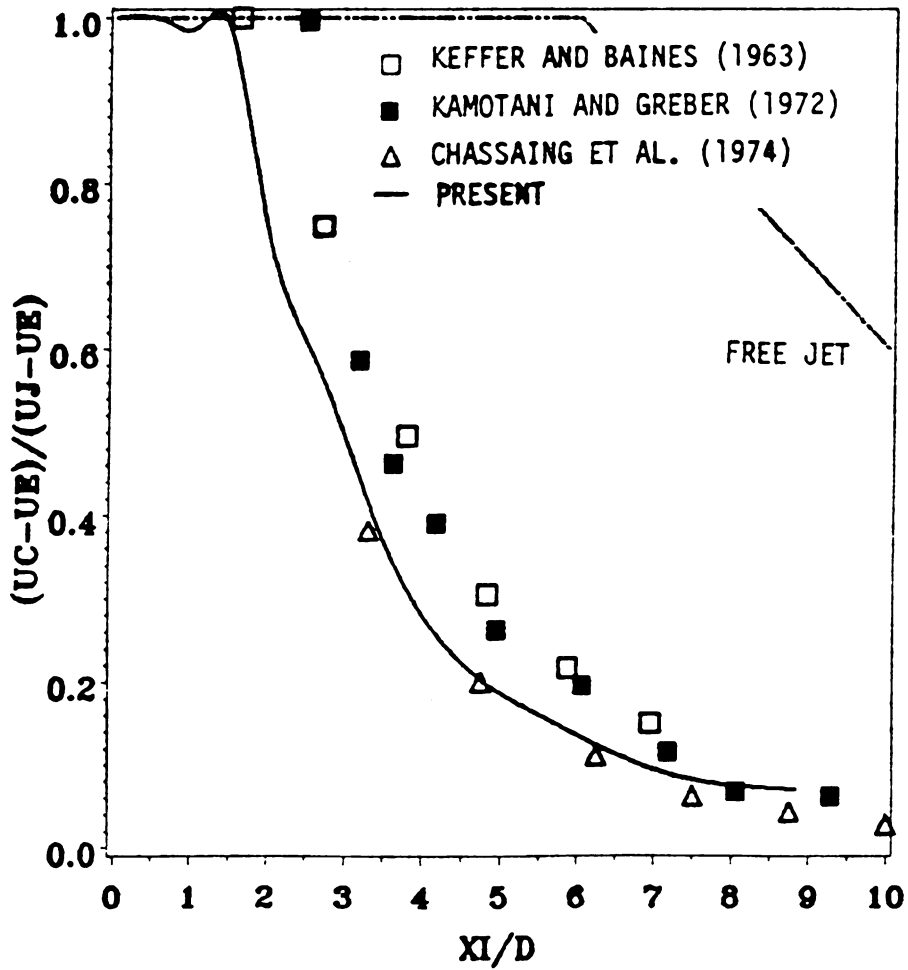


Figure 9. Single Circular Jet in a Crossflow at $R=4$: Comparison of Axial Velocity Decay

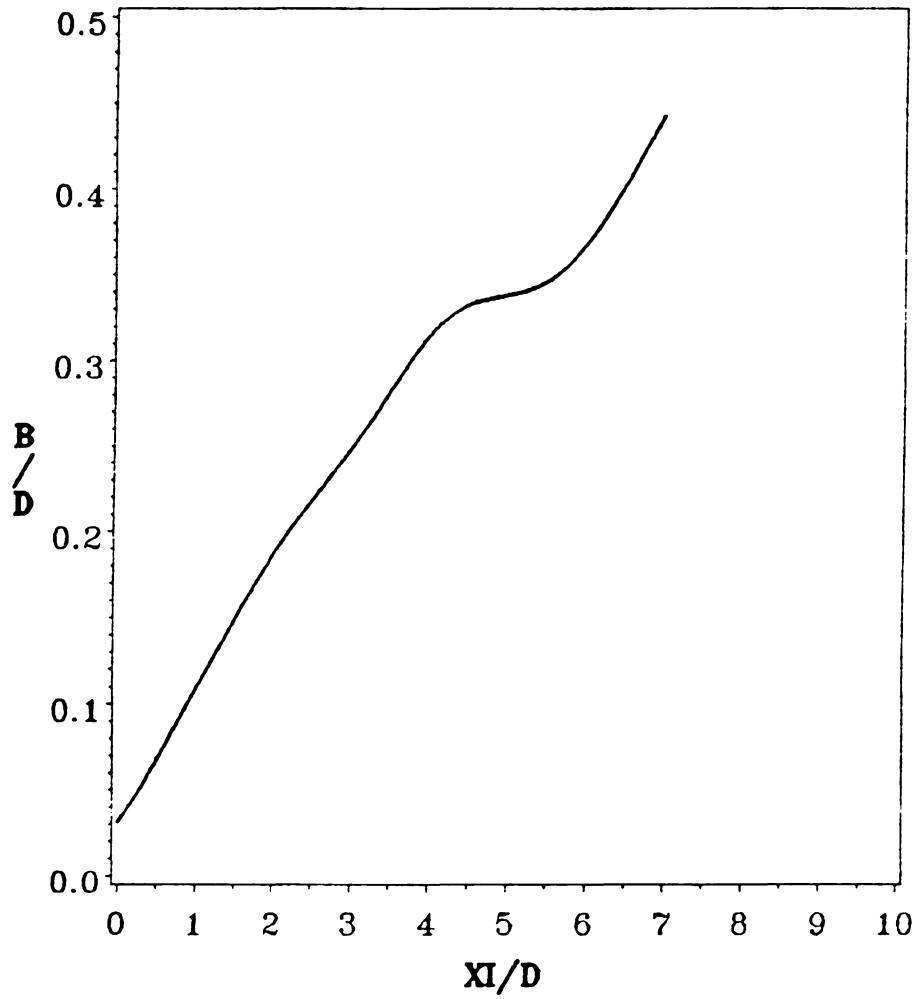


Figure 10. Single Circular Jet in a Crossflow at $R=4$: Variation of Averaged Half-Width along the Jet Axis

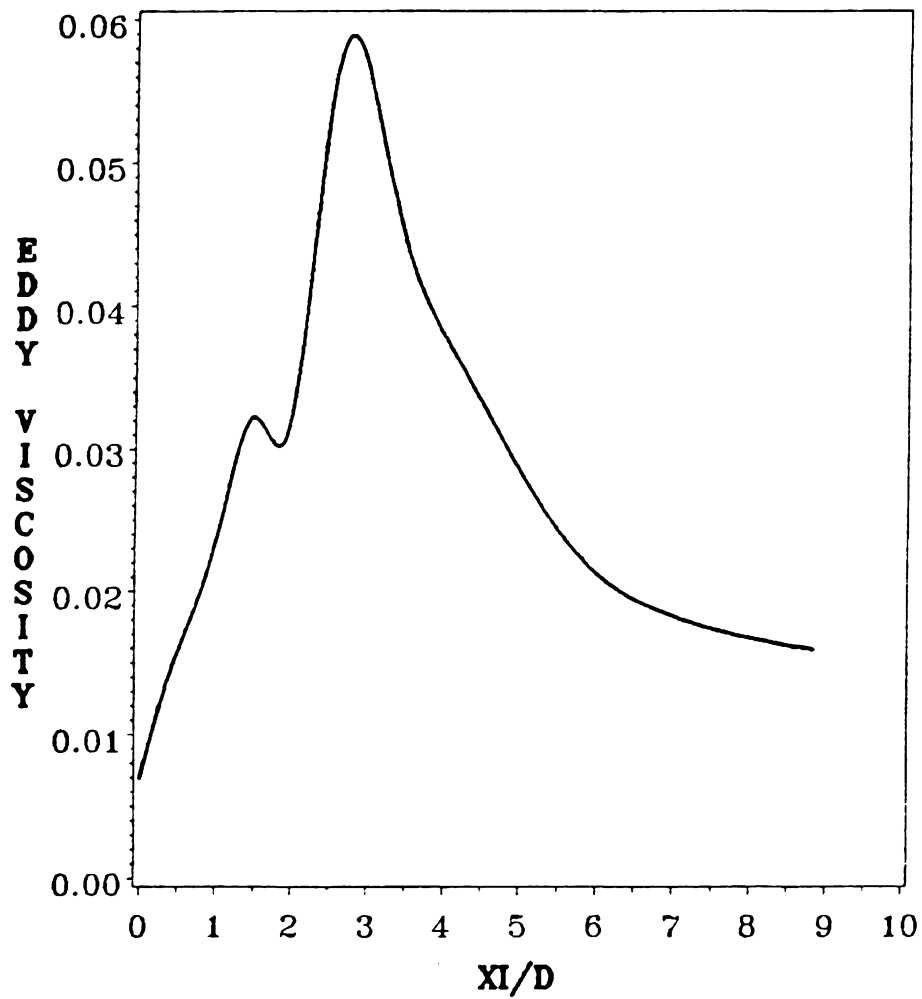


Figure 11. Single Circular Jet in a Crossflow at $R = 4$: Variation of Eddy Viscosity along the Jet Axis

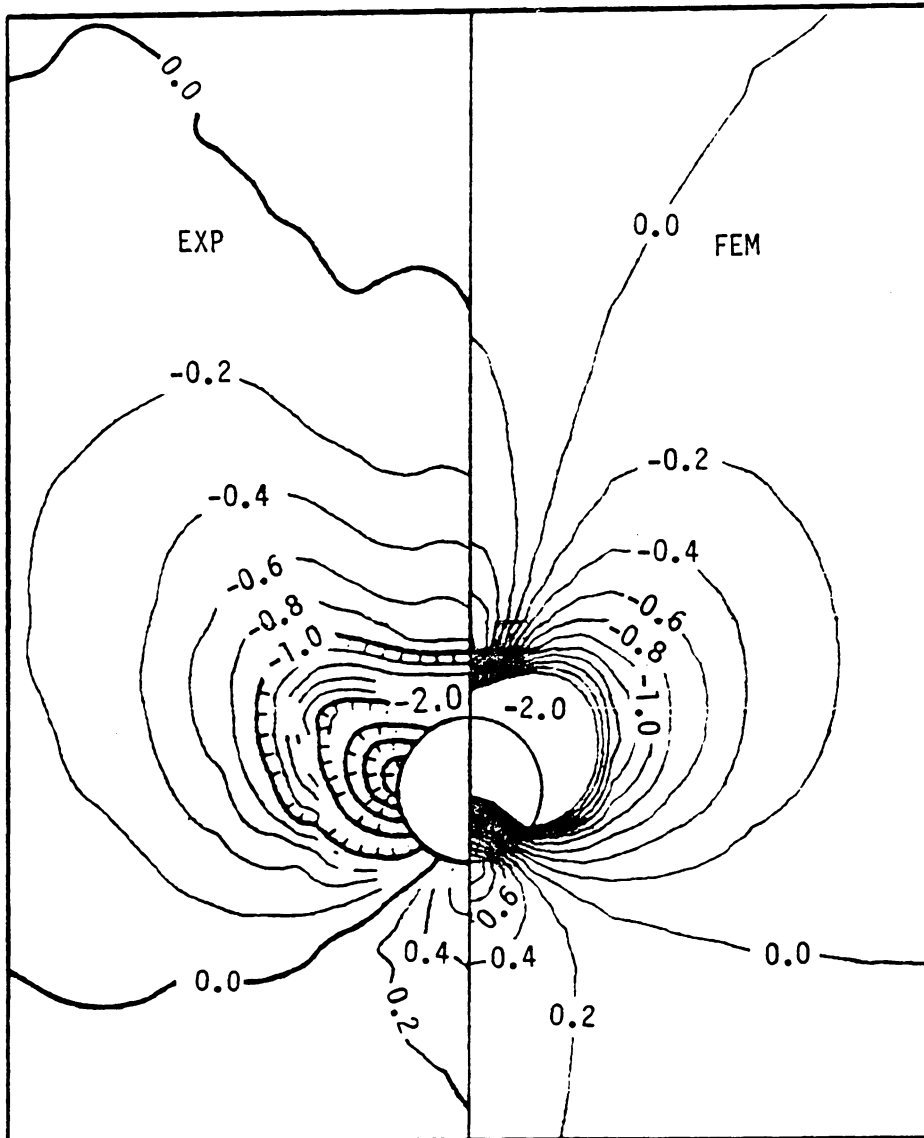


Figure 12. Single Circular Jet in a Crossflow at $R=4$: Comparison of Surface Pressure Coefficient

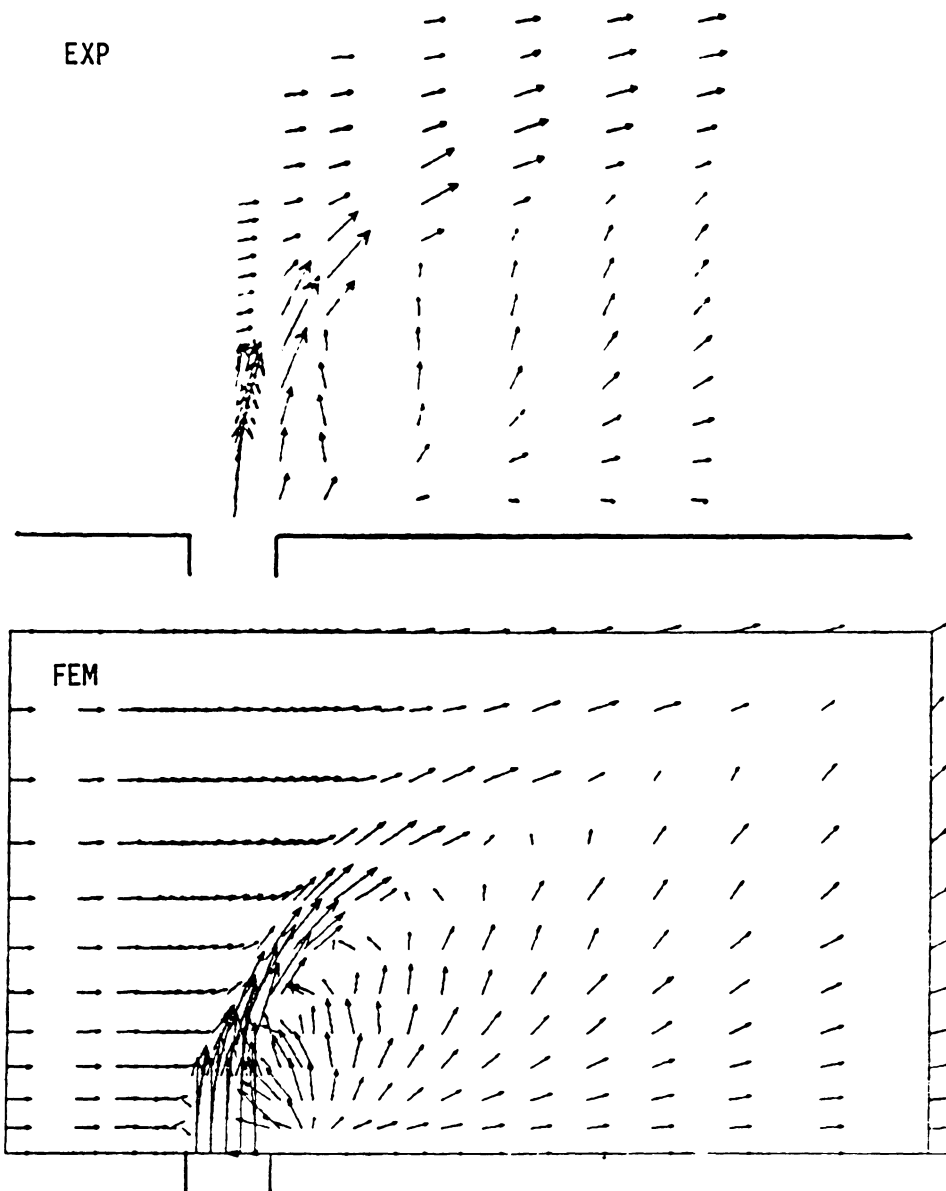


Figure 13. Single Circular Jet in a Crossflow at $R=4$: Comparison of Velocity Vector Plots on the Plane of Symmetry ($y/D=0.0$)

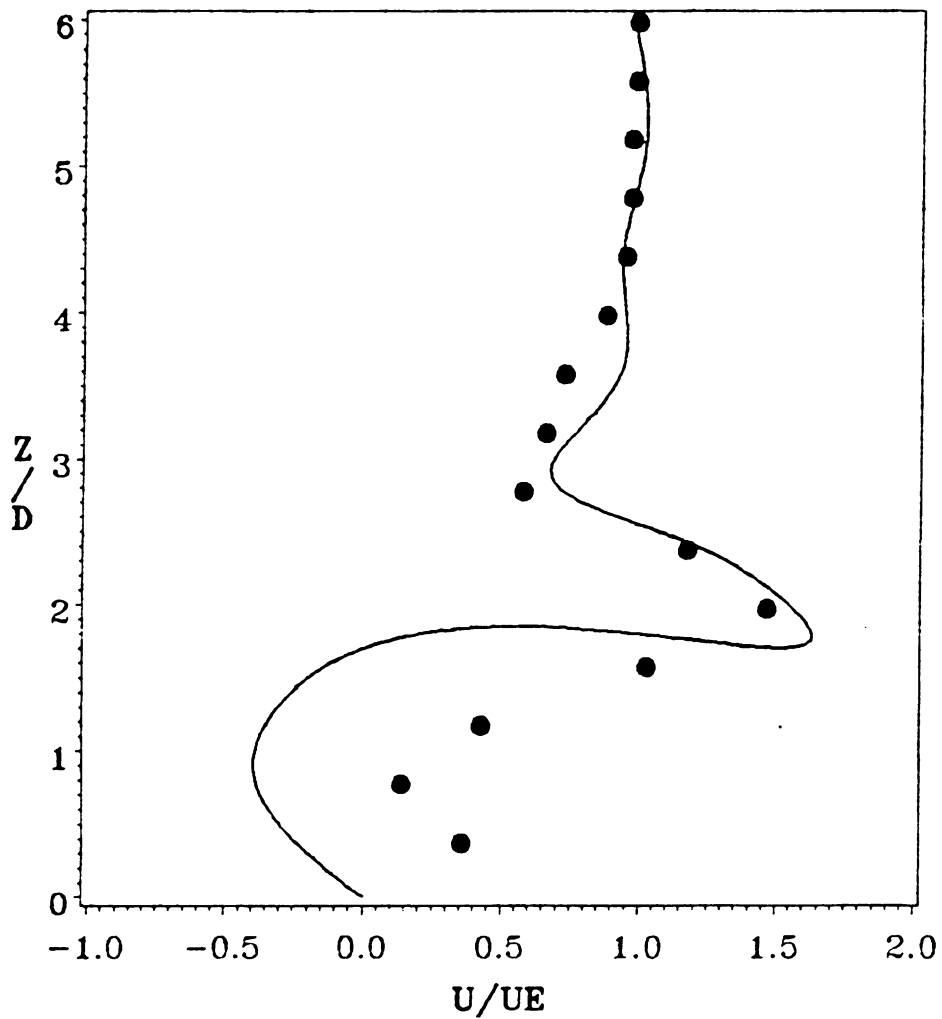


Figure 14. Single Circular Jet in a Crossflow at $R = 4$: Comparison of Streamwise Velocity Profiles at $x/D = 0.5$ and $y/D = 0.0$: circle - measured data [80], solid line - computed result

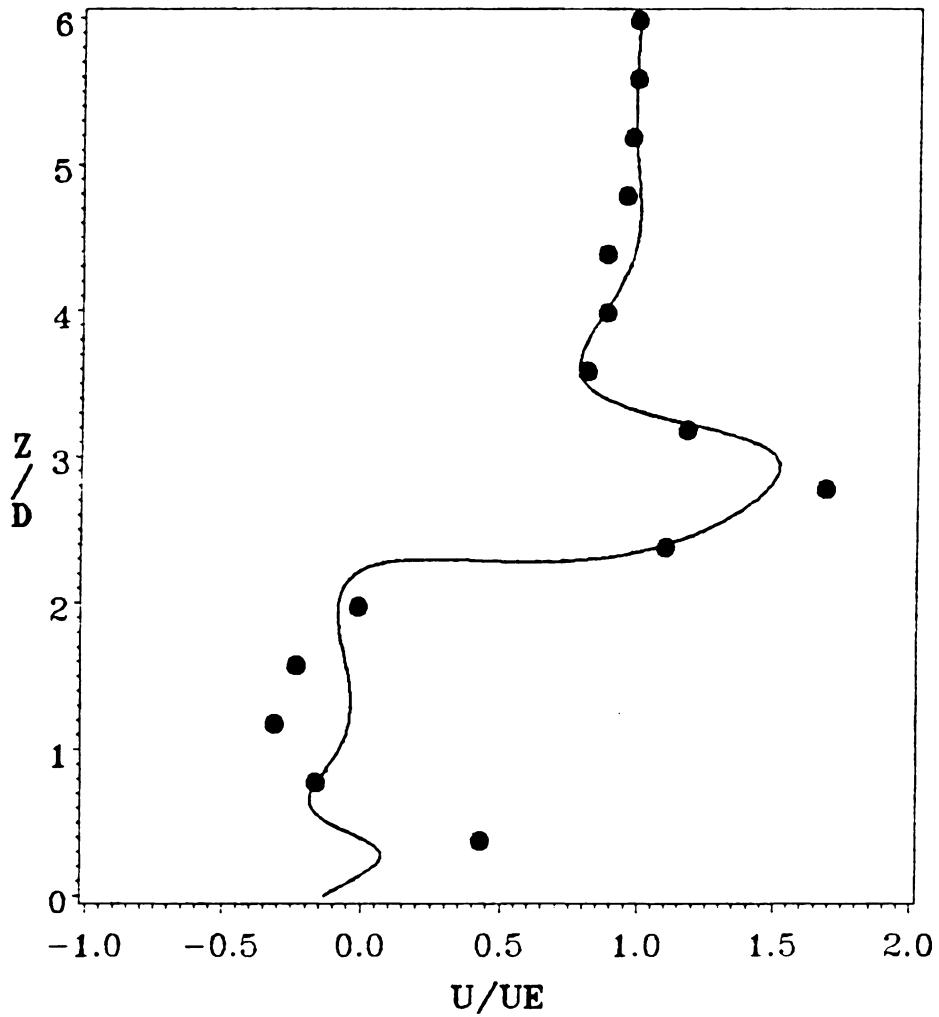


Figure 15. Single Circular Jet in a Crossflow at $R=4$: Comparison of Streamwise Velocity Profiles at $x/D=1.0$ and $y/D=0.0$: circle - measured data [80], solid line - computed result

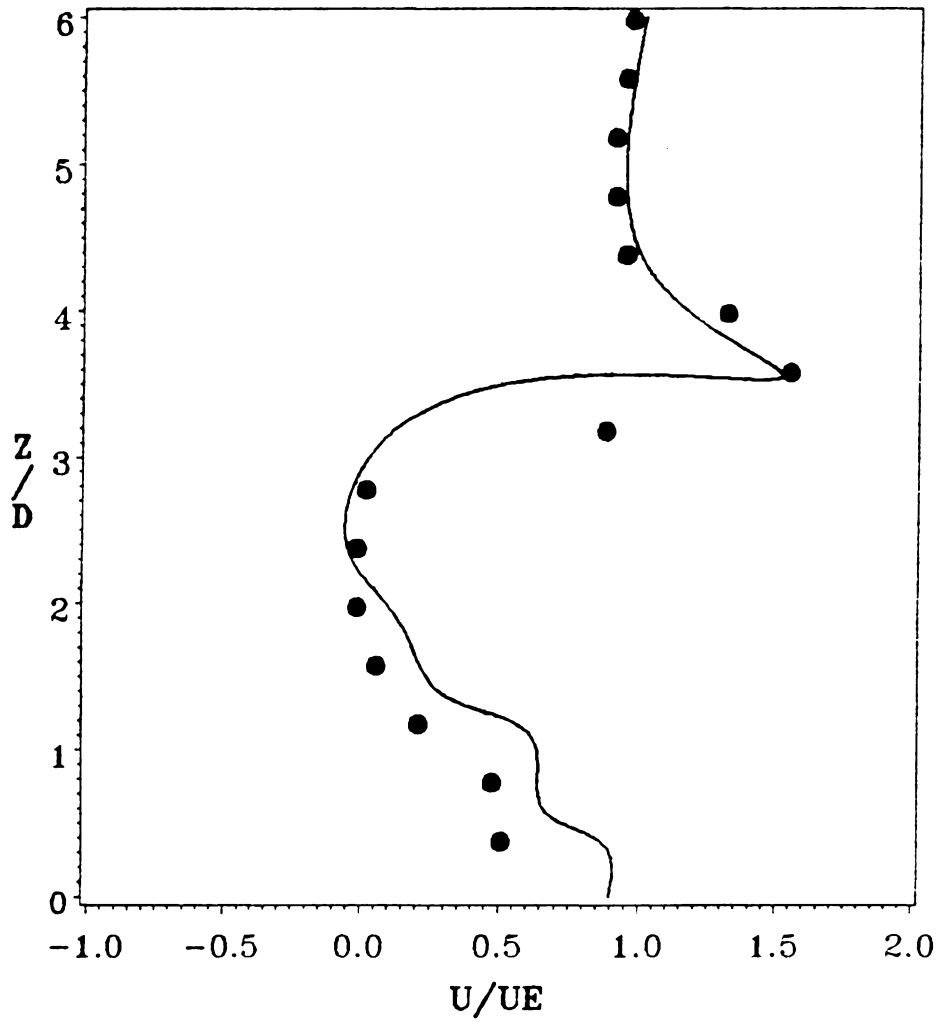


Figure 16. Single Circular Jet in a Crossflow at $R=4$: Comparison of Streamwise Velocity Profiles at $x/D=2.0$ and $y/D=0.0$: circle - measured data [80], solid line - computed result

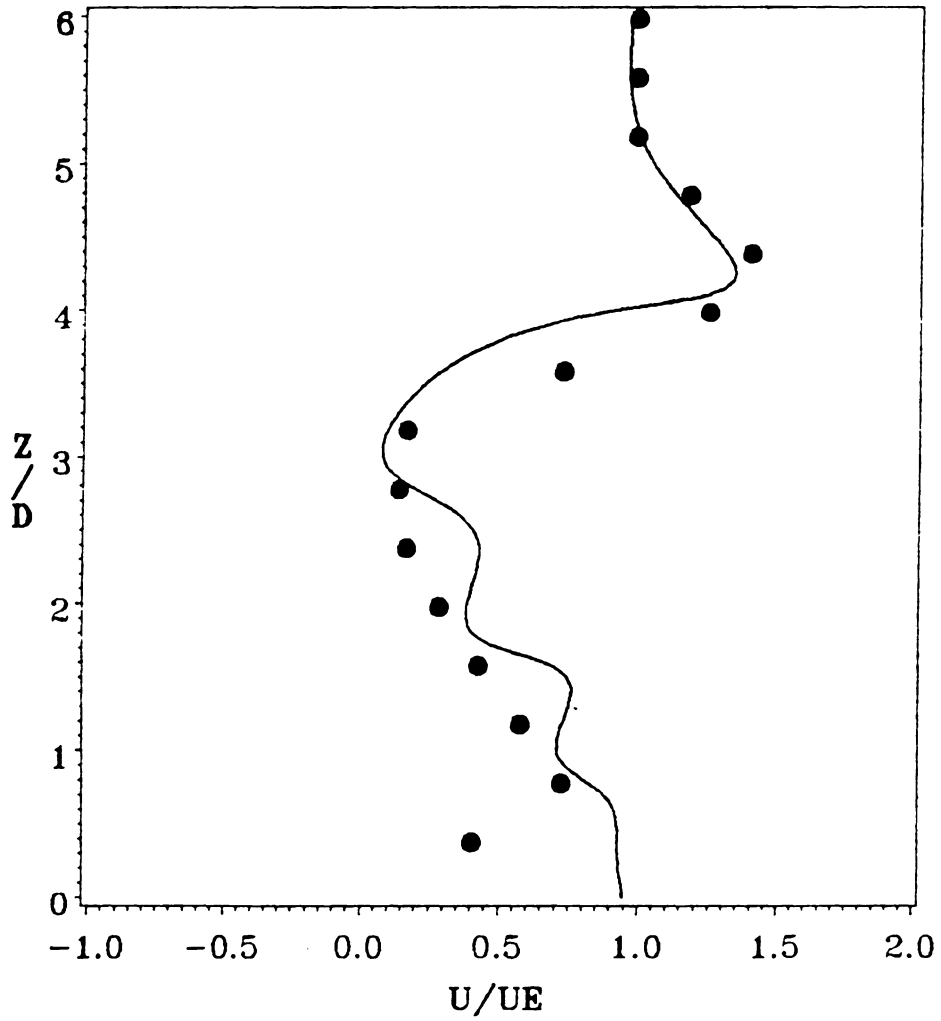


Figure 17. Single Circular Jet in a Crossflow at $R=4$: Comparison of Streamwise Velocity Profiles at $x/D=3.0$ and $y/D=0.0$: circle - measured data [80], solid line - computed result

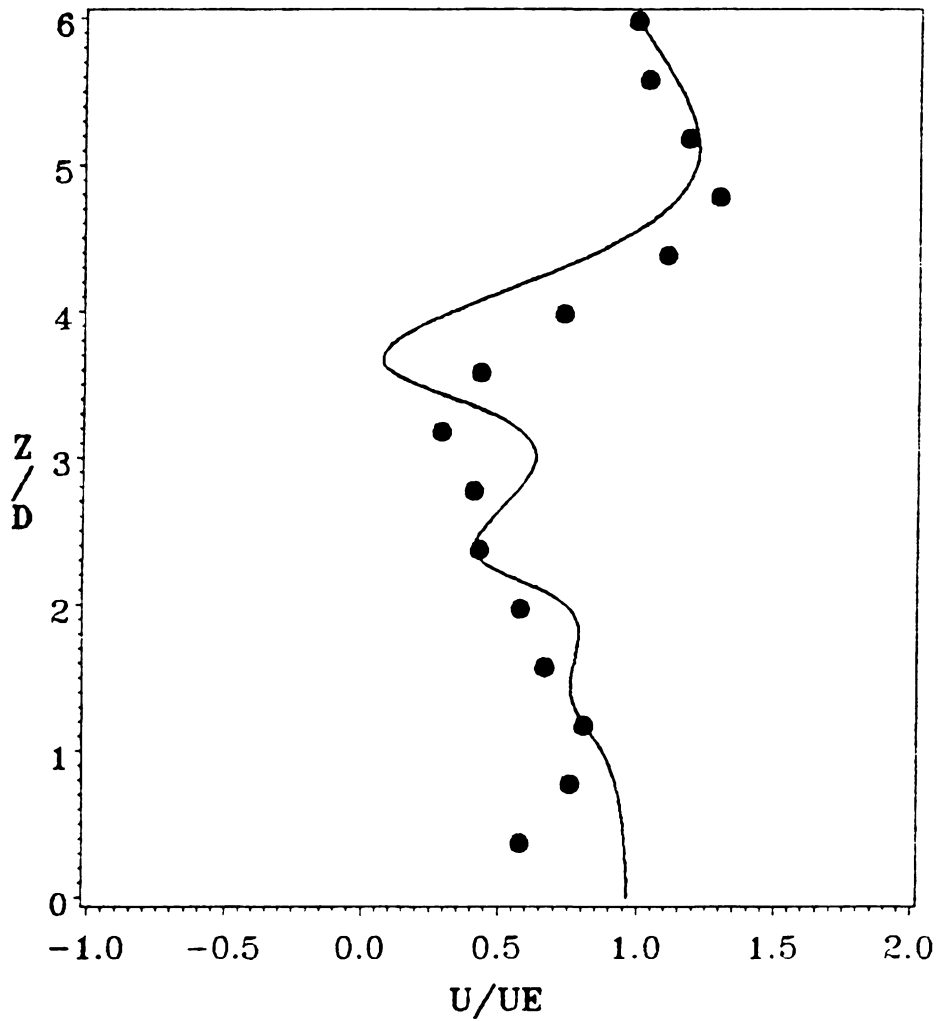


Figure 18. Single Circular Jet in a Crossflow at $R = 4$: Comparison of Streamwise Velocity Profiles at $x/D = 4.0$ and $y/D = 0.0$: circle - measured data [80], solid line - computed result

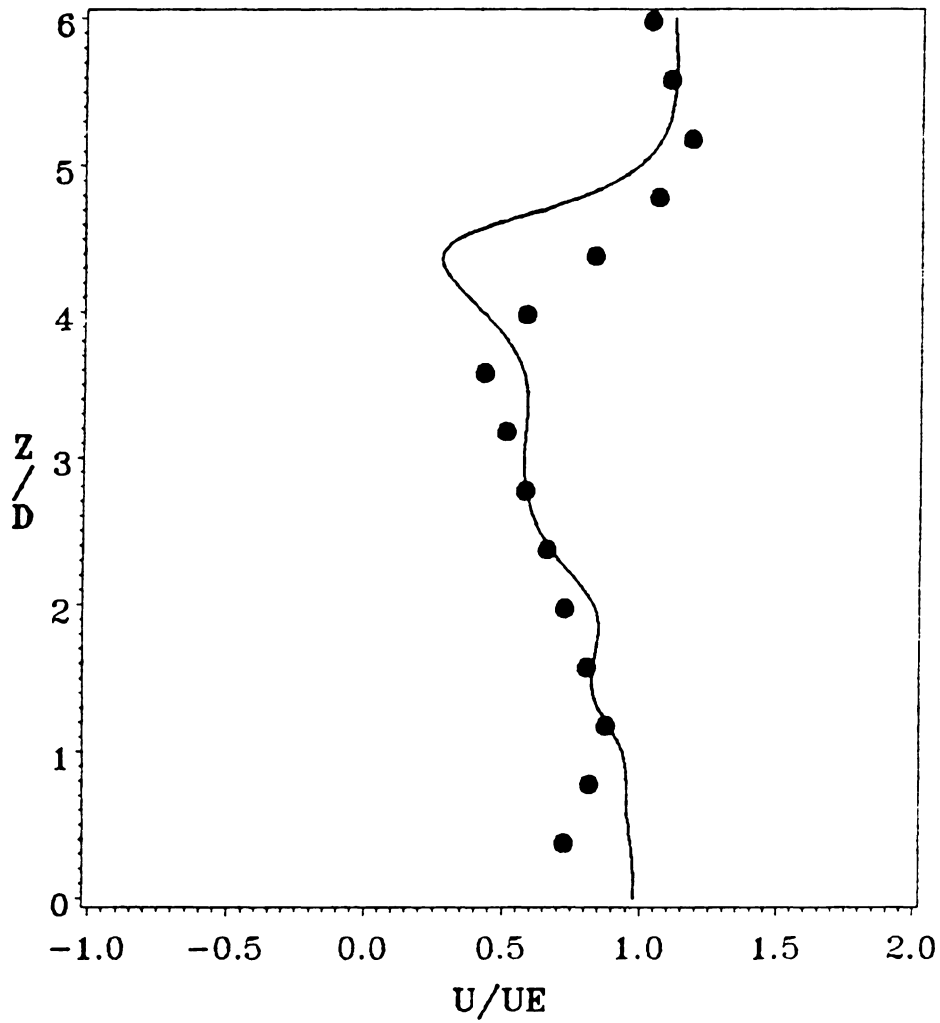


Figure 19. Single Circular Jet in a Crossflow at $R = 4$: Comparison of Streamwise Velocity Profiles at $x/D = 5.0$ and $y/D = 0.0$: circle - measured data [80], solid line - computed result

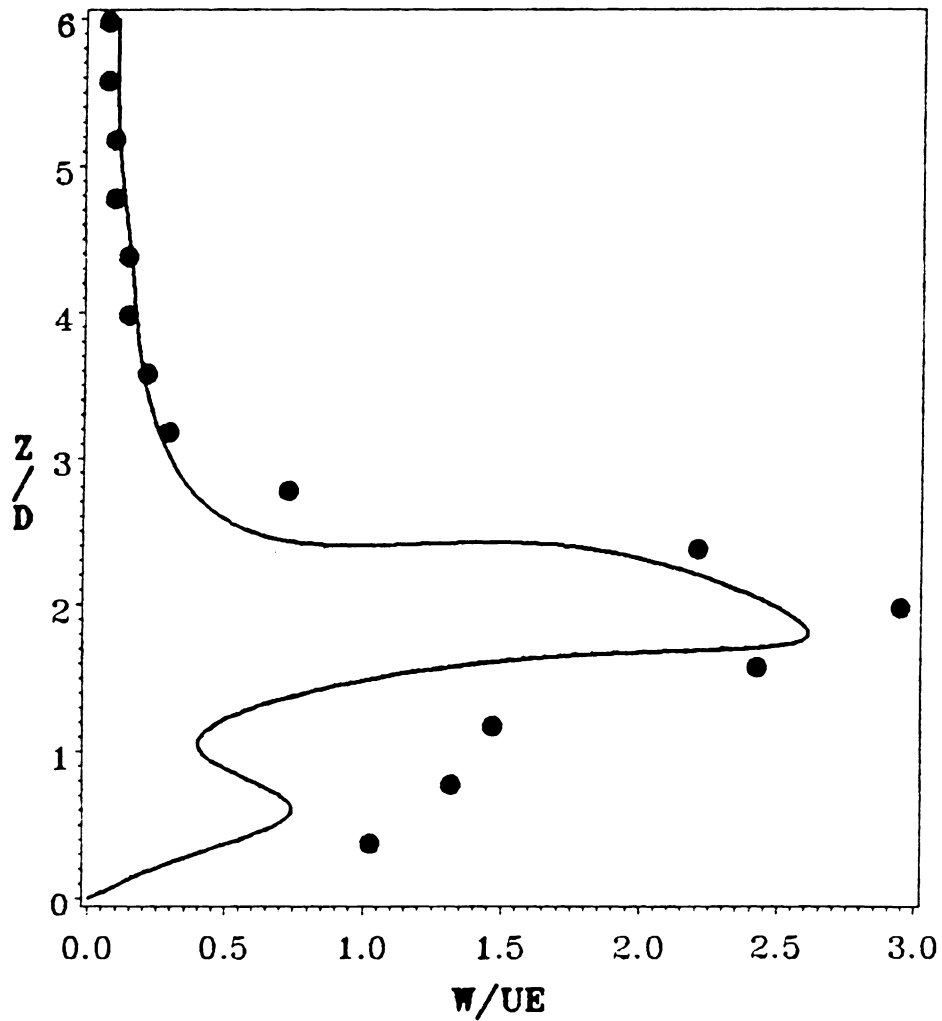


Figure 20. Single Circular Jet in a Crossflow at $R=4$: Comparison of Normal Velocity Profiles at $x/D=0.5$ and $y/D=0.0$: circle - measured data [80], solid line - computed result

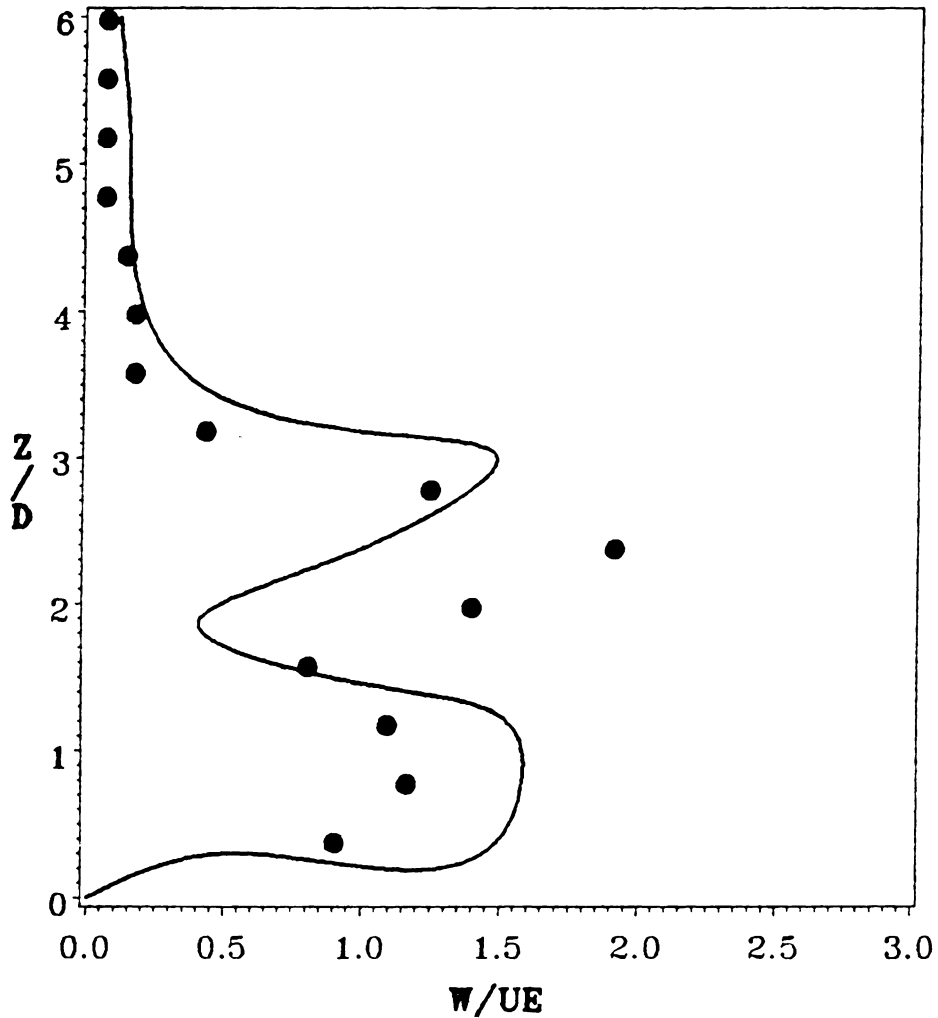


Figure 21. Single Circular Jet in a Crossflow at $R=4$: Comparison of Normal Velocity Profiles at $x/D=1.0$ and $y/D=0.0$: circle - measured data [80], solid line - computed result

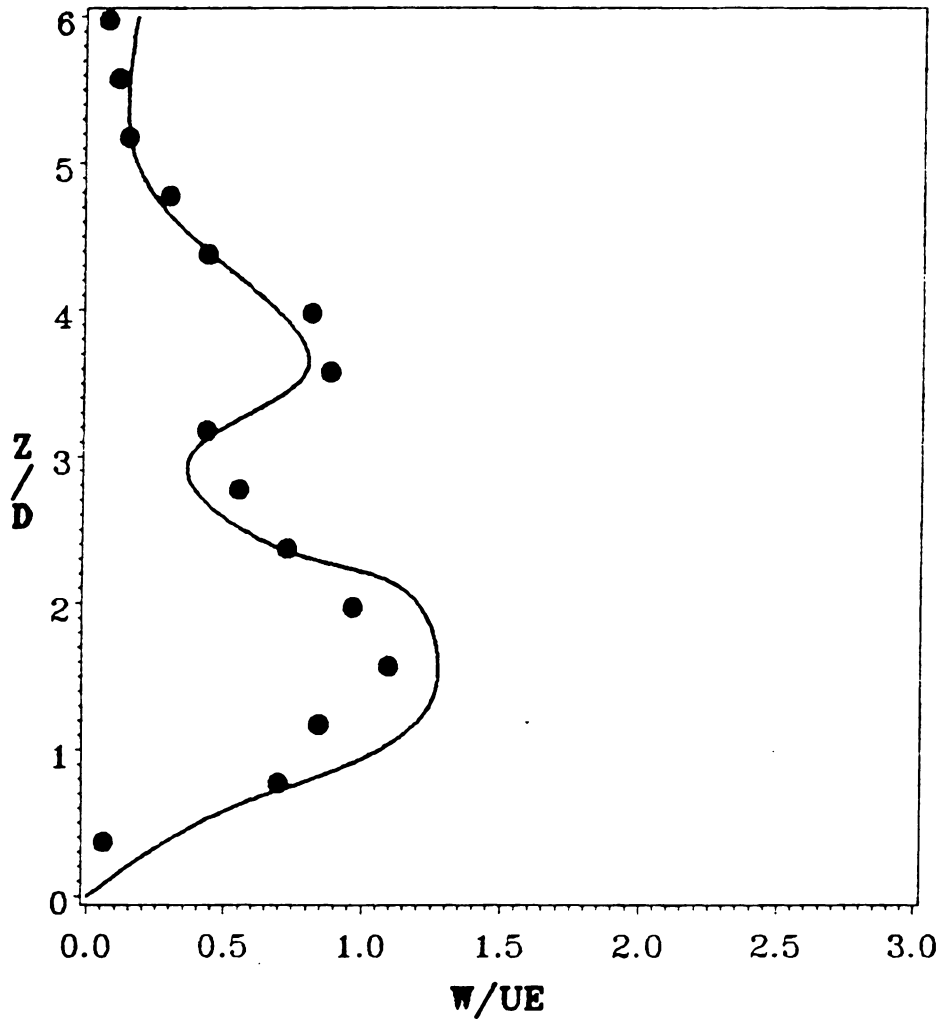


Figure 22. Single Circular Jet in a Crossflow at $R=4$: Comparison of Normal Velocity Profiles at $x/D=2.0$ and $y/D=0.0$: circle - measured data [80], solid line - computed result

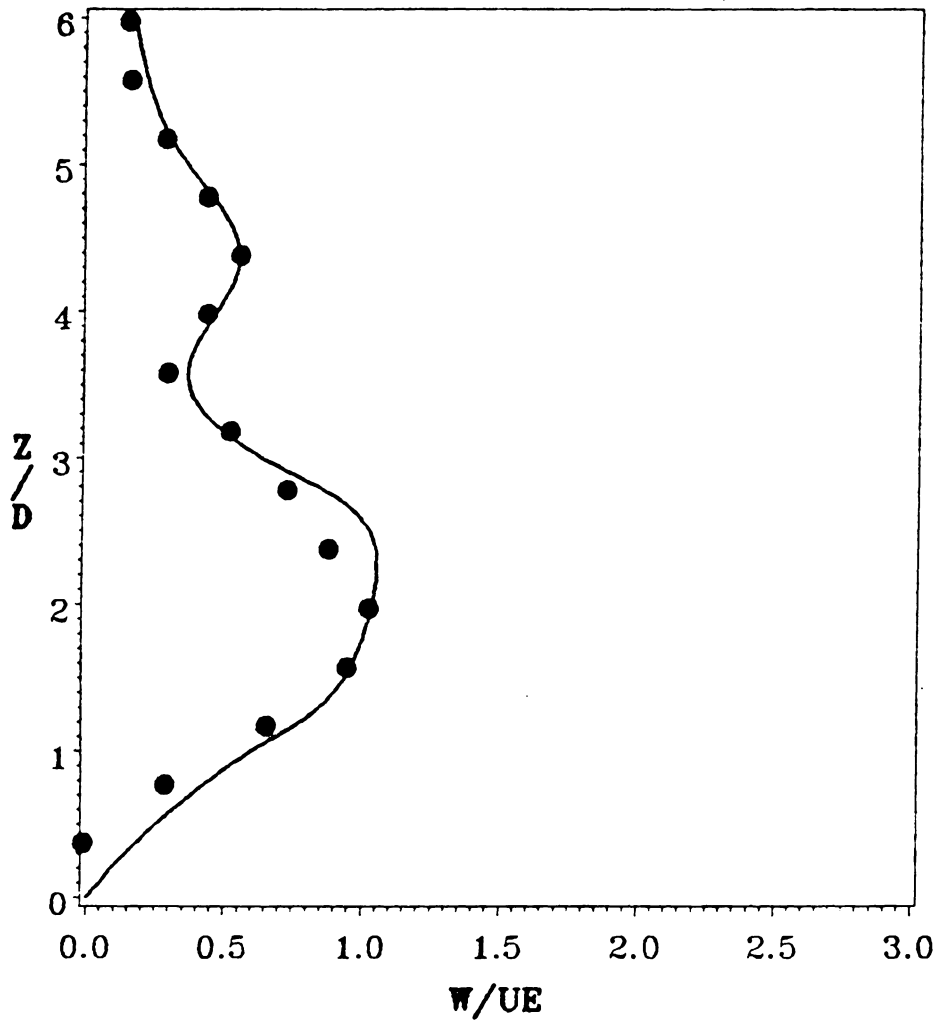


Figure 23. Single Circular Jet in a Crossflow at $R=4$: Comparison of Normal Velocity Profiles at $x/D=3.0$ and $y/D=0.0$: circle - measured data [80], solid line - computed result

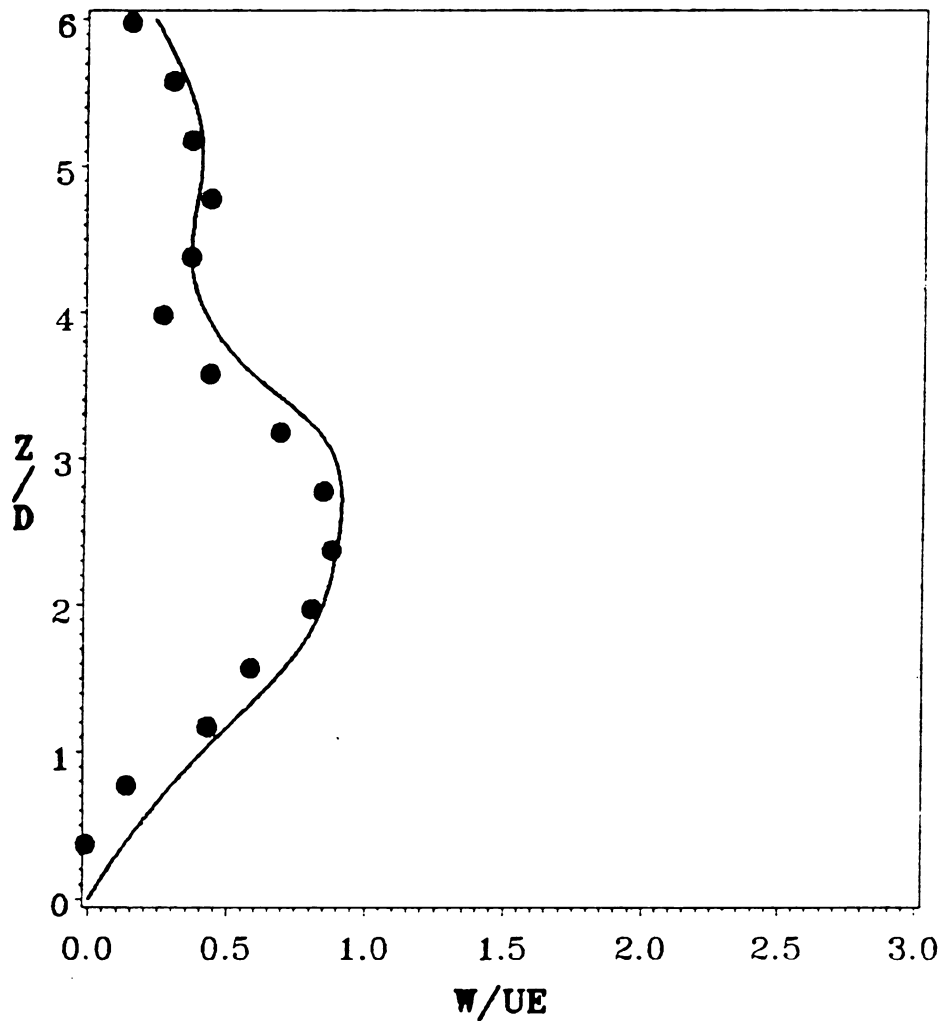


Figure 24. Single Circular Jet in a Crossflow at $R=4$: Comparison of Normal Velocity Profiles at $x/D=4.0$ and $y/D=0.0$: circle - measured data [80], solid line - computed result

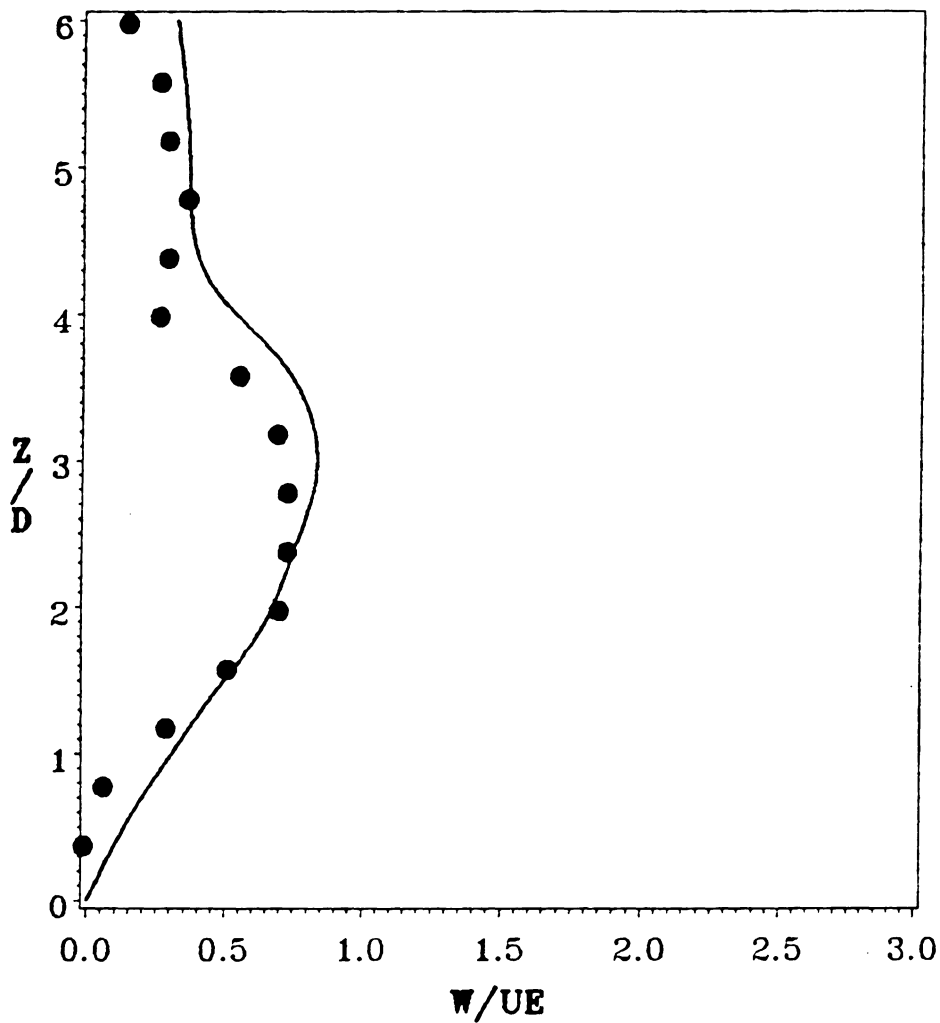


Figure 25. Single Circular Jet in a Crossflow at $R=4$: Comparison of Normal Velocity Profiles at $x/D=5.0$ and $y/D=0.0$: circle - measured data [80], solid line - computed result

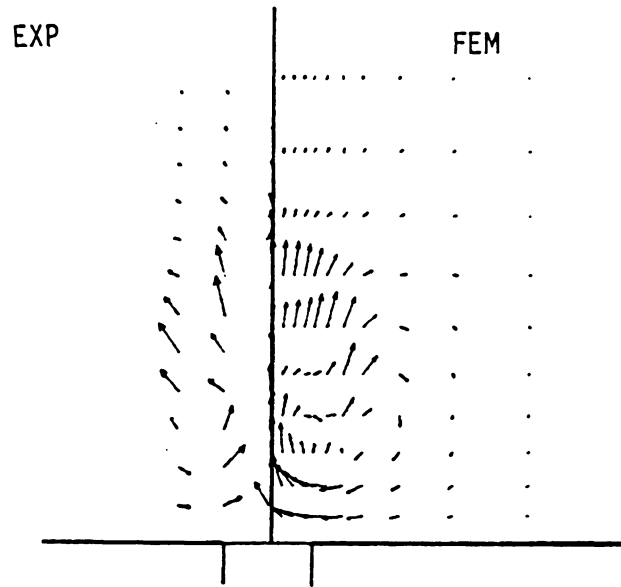


Figure 26. Single Circular Jet in a Crossflow at $R=4$: Comparison of Velocity Vector Plots on the Crossflow Plane ($x/D=0.0$)

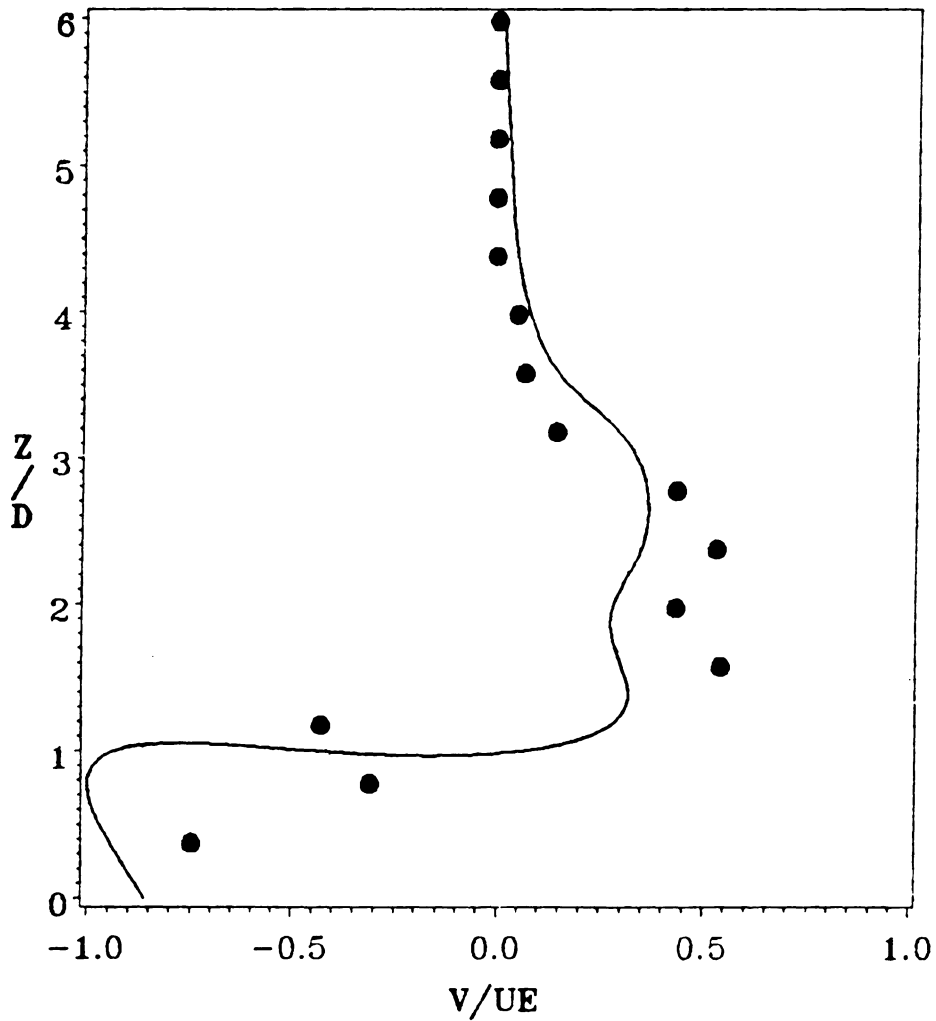


Figure 27. Single Circular Jet in a Crossflow at $R=4$: Comparison of Transverse Velocity Profiles at $x/D=1.0$ and $y/D=0.5$: circle - measured data [80], solid line - computed result

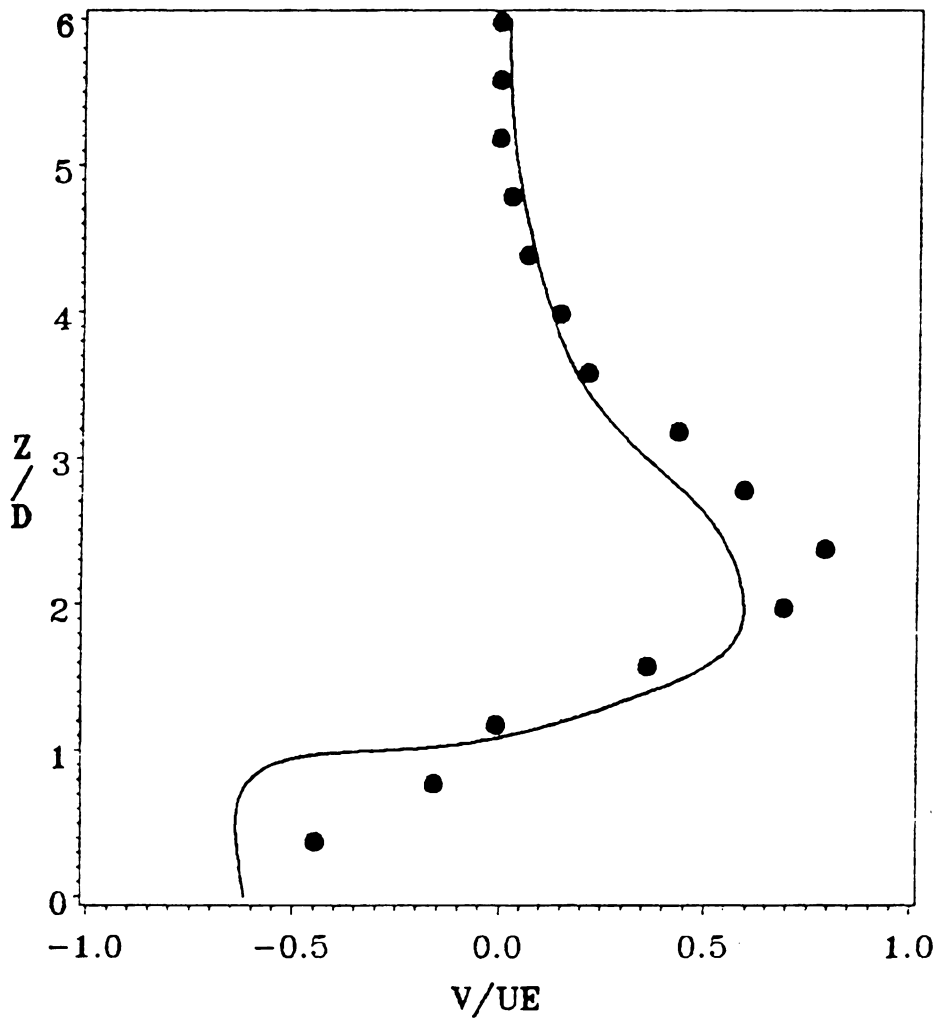


Figure 28. Single Circular Jet in a Crossflow at $R=4$: Comparison of Transverse Velocity Profiles at $x/D=1.0$ and $y/D=1.0$: circle - measured data [80], solid line - computed result

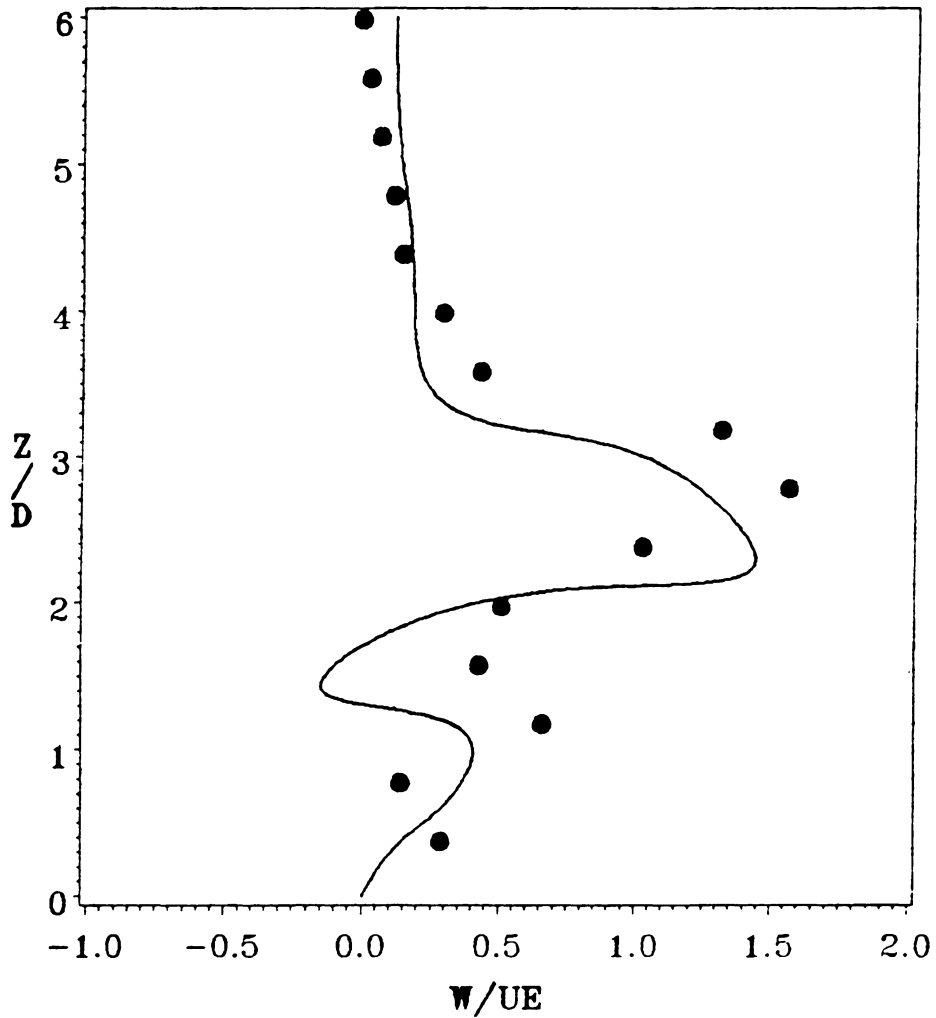


Figure 29. Single Circular Jet in a Crossflow at $R=4$: Comparison of Normal Velocity Profiles at $x/D=1.0$ and $y/D=0.5$: circle - measured data [80], solid line - computed result

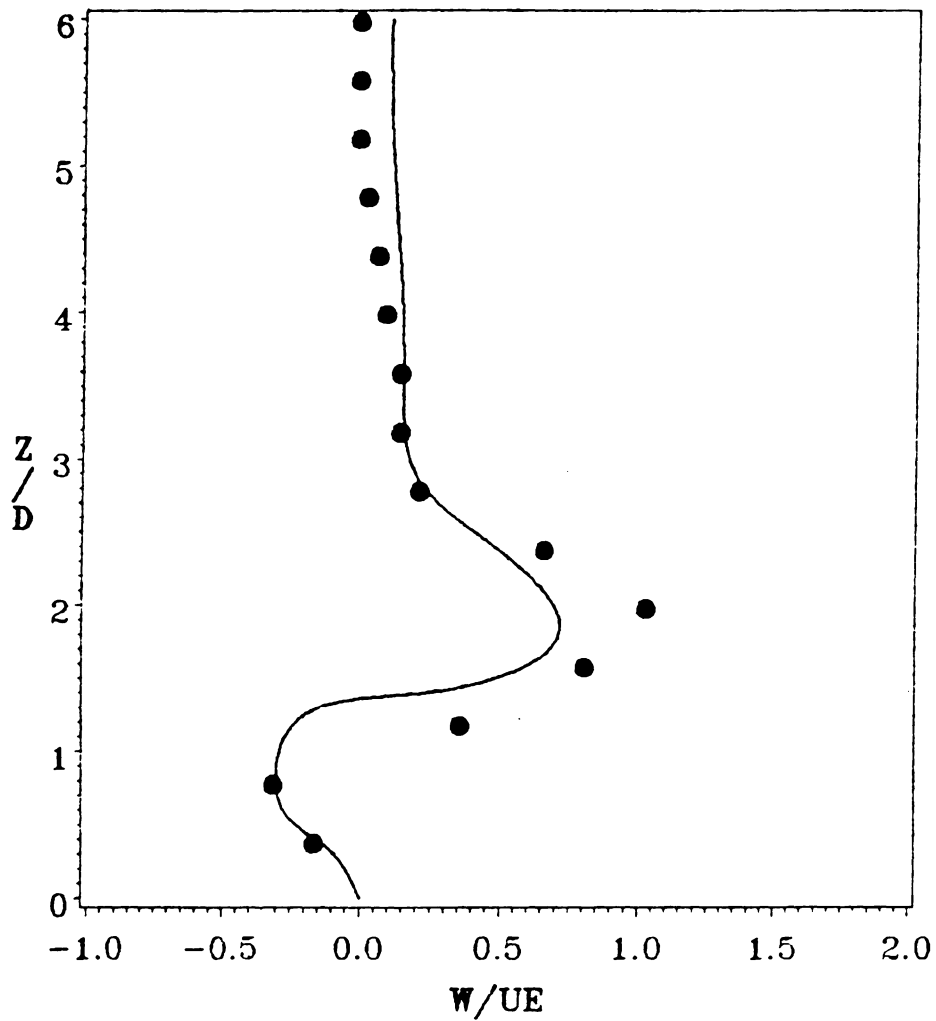


Figure 30. Single Circular Jet in a Crossflow at $R=4$: Comparison of Normal Velocity Profiles at $x/D=1.0$ and $y/D=1.0$: circle - measured data [80], solid line - computed result

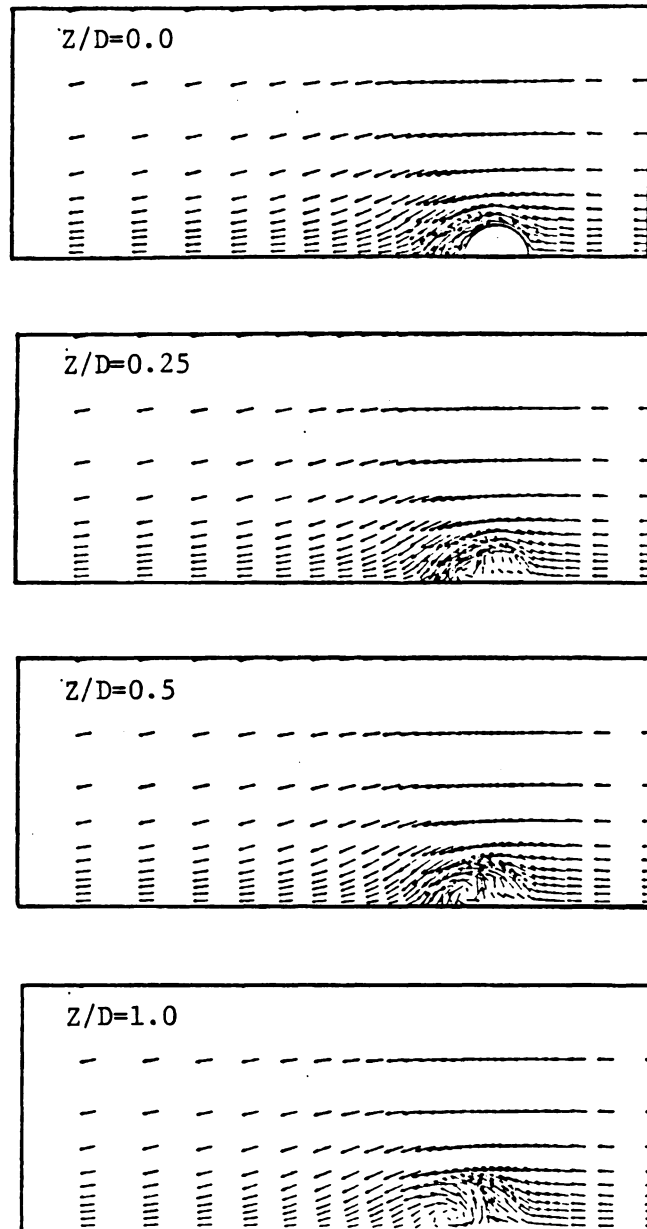


Figure 31. Single Circular Jet in a Crossflow at $R = 4$: Display of Velocity Vectors on the Plane $z/D = 0.0, 0.25, 0.5, 1.0$ from above

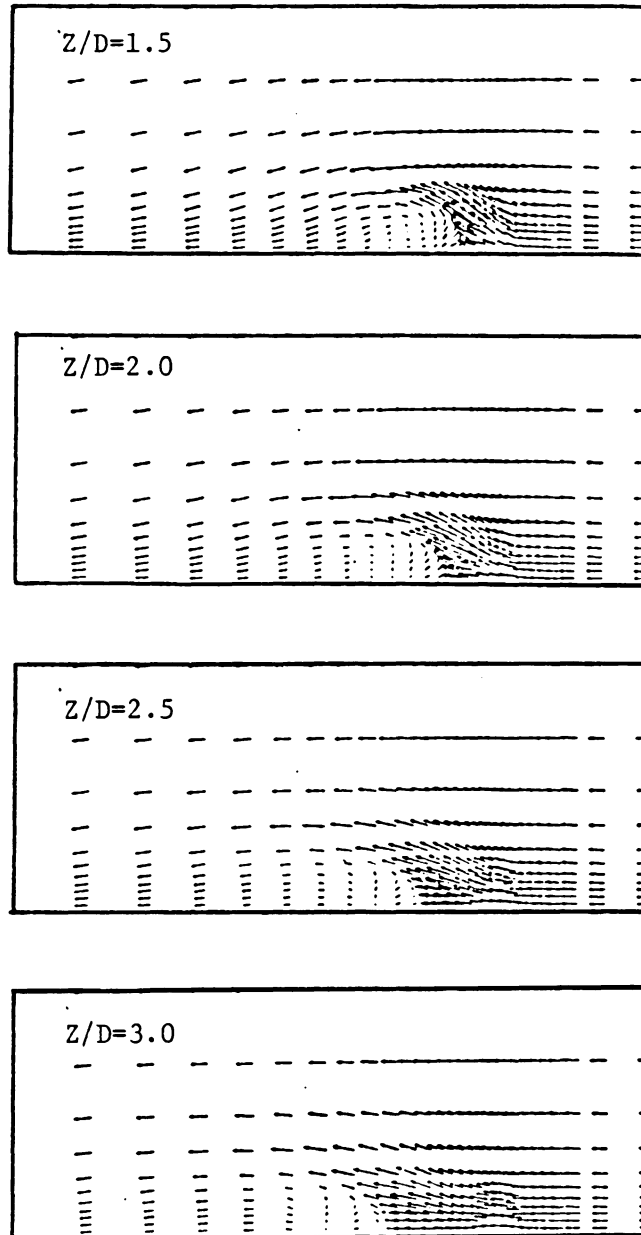


Figure 32. Single Circular Jet in a Crossflow at $R = 4$: Display of Velocity Vectors on the Plane $z/D = 1.5, 2.0, 2.5, 3.0$ from above

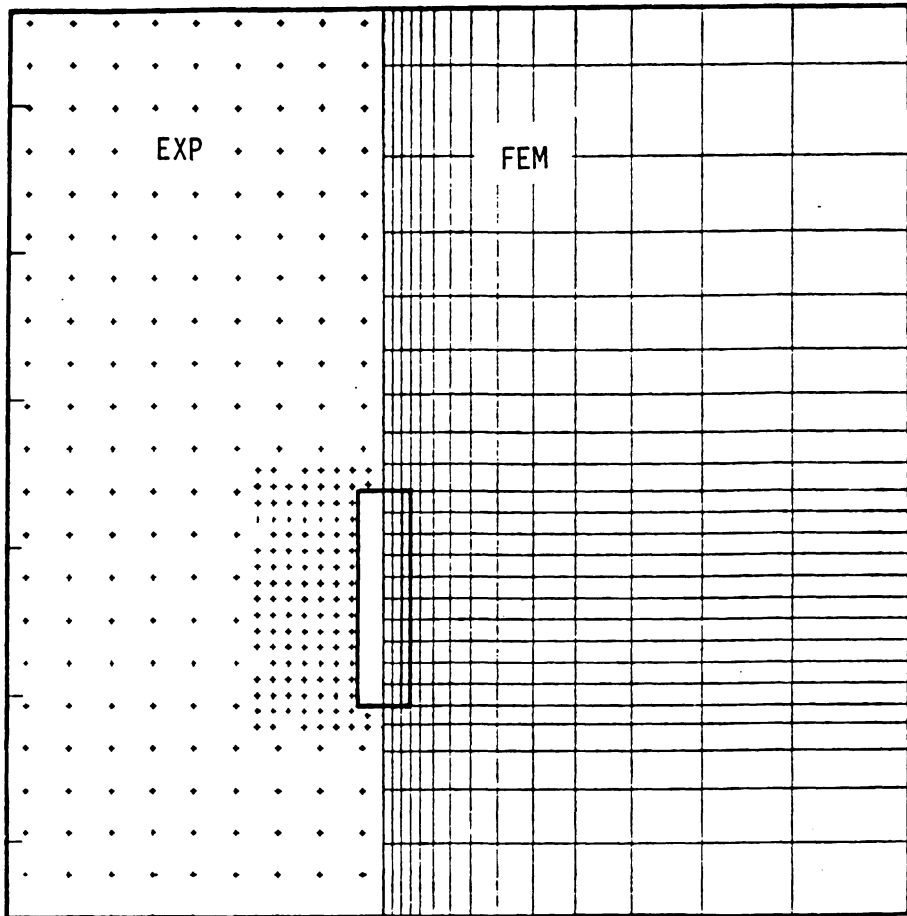


Figure 33. Single Rectangular Jet in a Crossflow at $R=4$: Finite Element Mesh vs. Surface Pressure Tap Locations

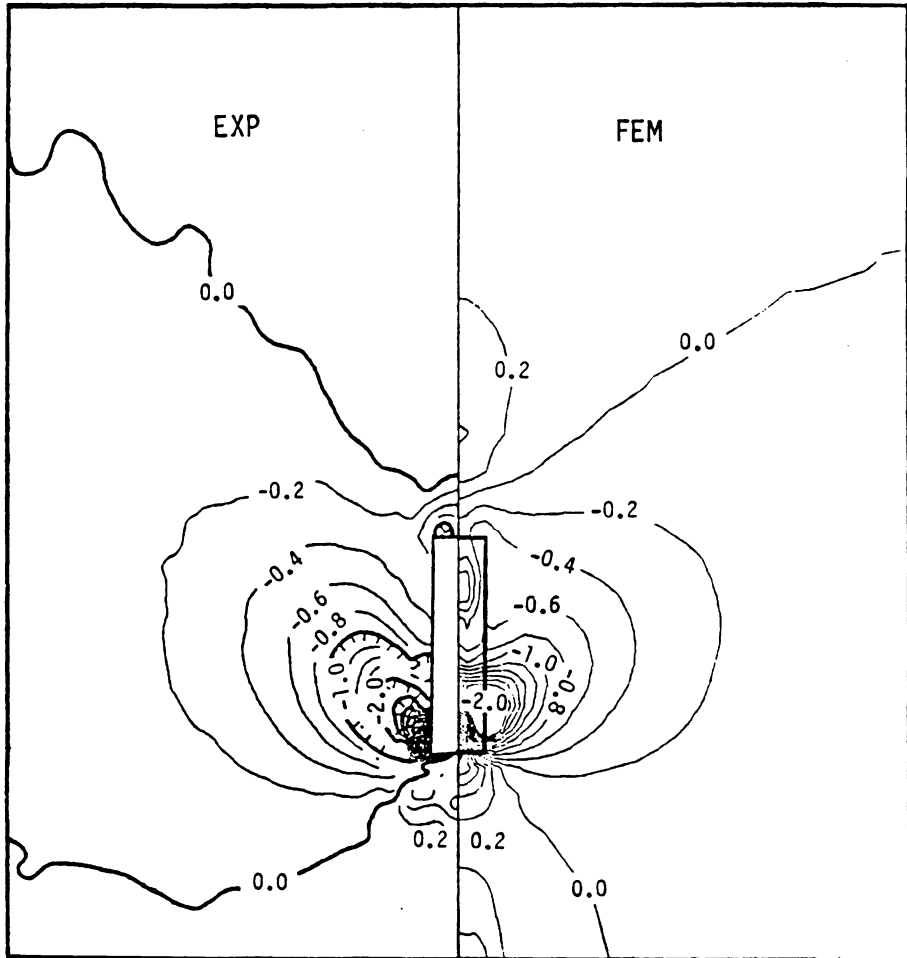


Figure 34. Single Rectangular Jet in a Crossflow at $R=4$: Comparison of Surface Pressure coefficient

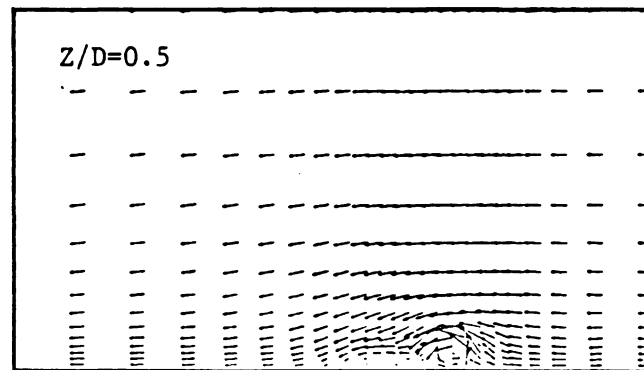
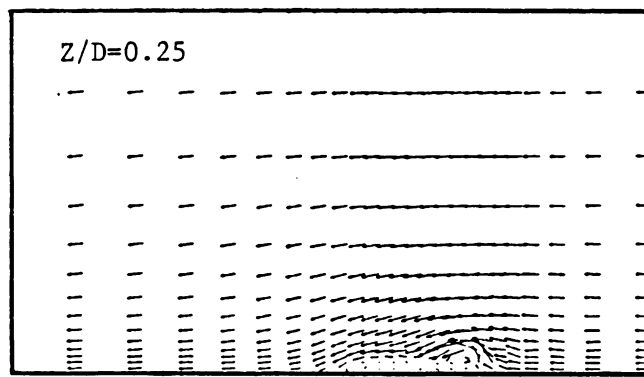
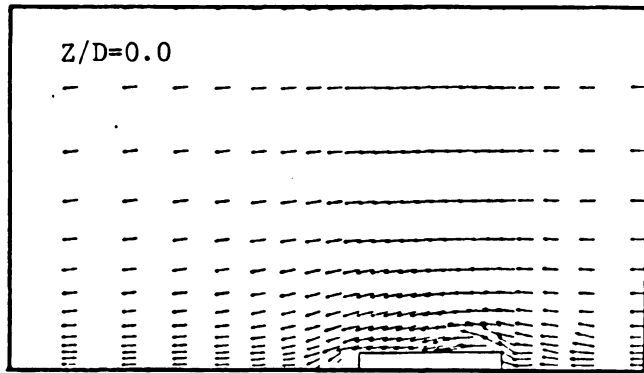


Figure 35. Single Rectangular Jet in a Crossflow at $R=4$: Display of Velocity Vectors on the Plane $z/D=0.0, 0.25, 0.5$ from above

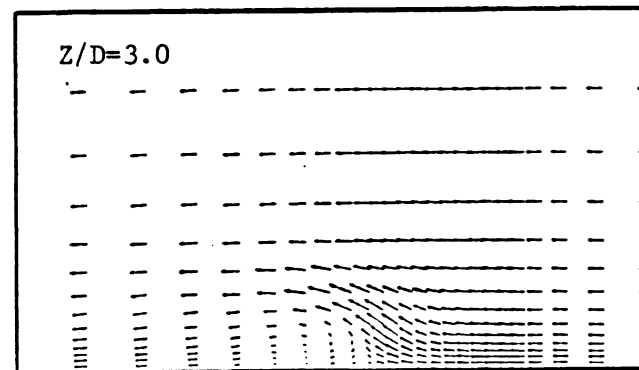
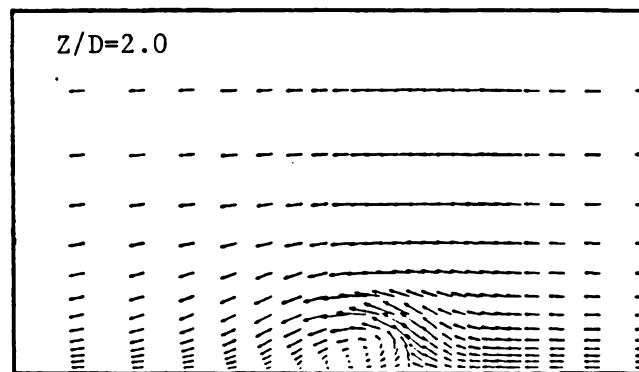
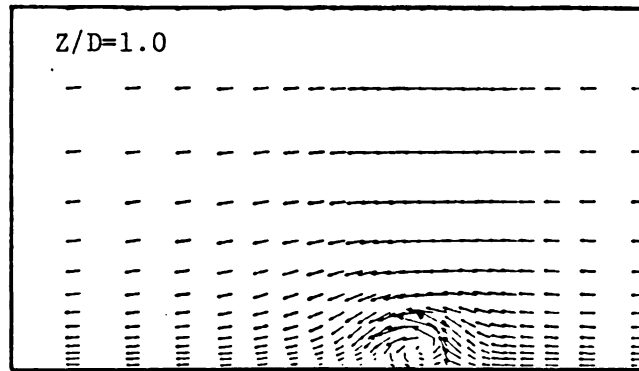


Figure 36. Single Rectangular Jet in a Crossflow at $R=4$: Display of Velocity Vectors on the Plane $z/D = 1.0, 2.0, 3.0$ from above

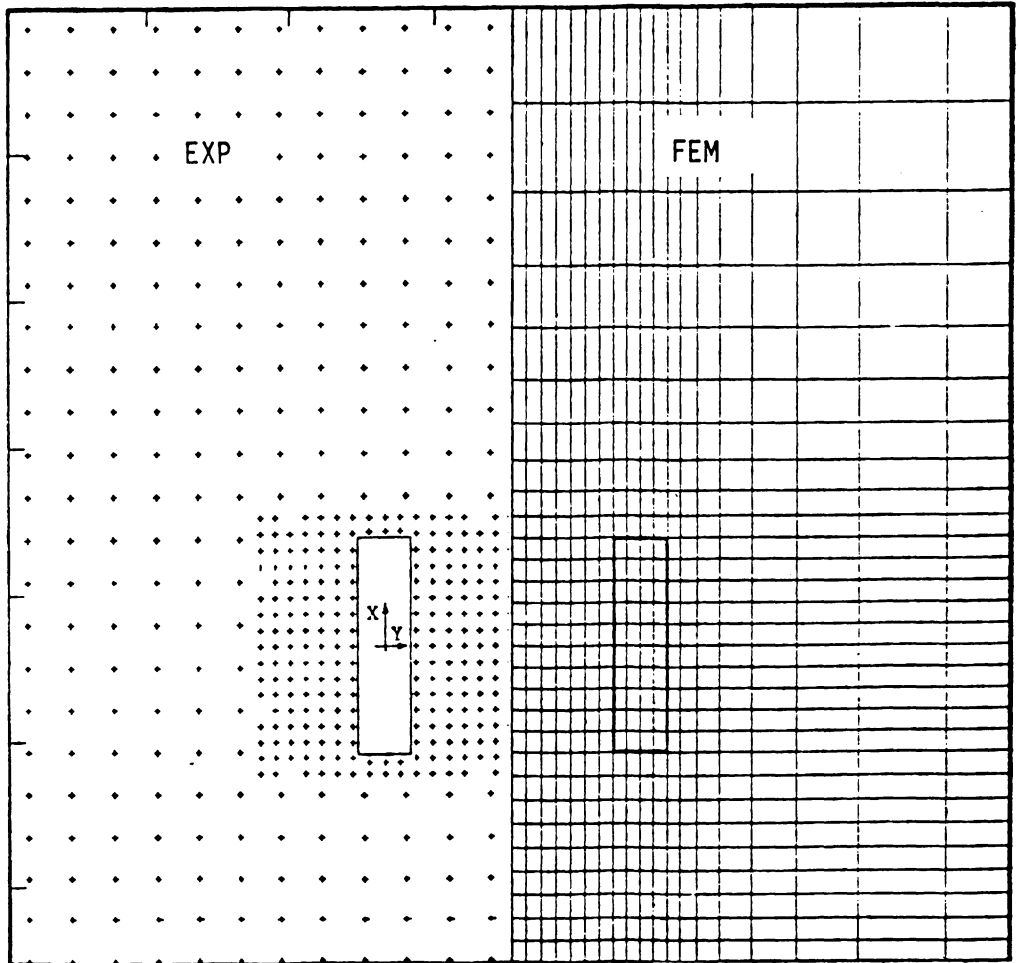


Figure 37. Dual Rectangular Jets in a Crossflow at $R=4$: Finite Element Mesh vs. Surface Pressure Tap Locations

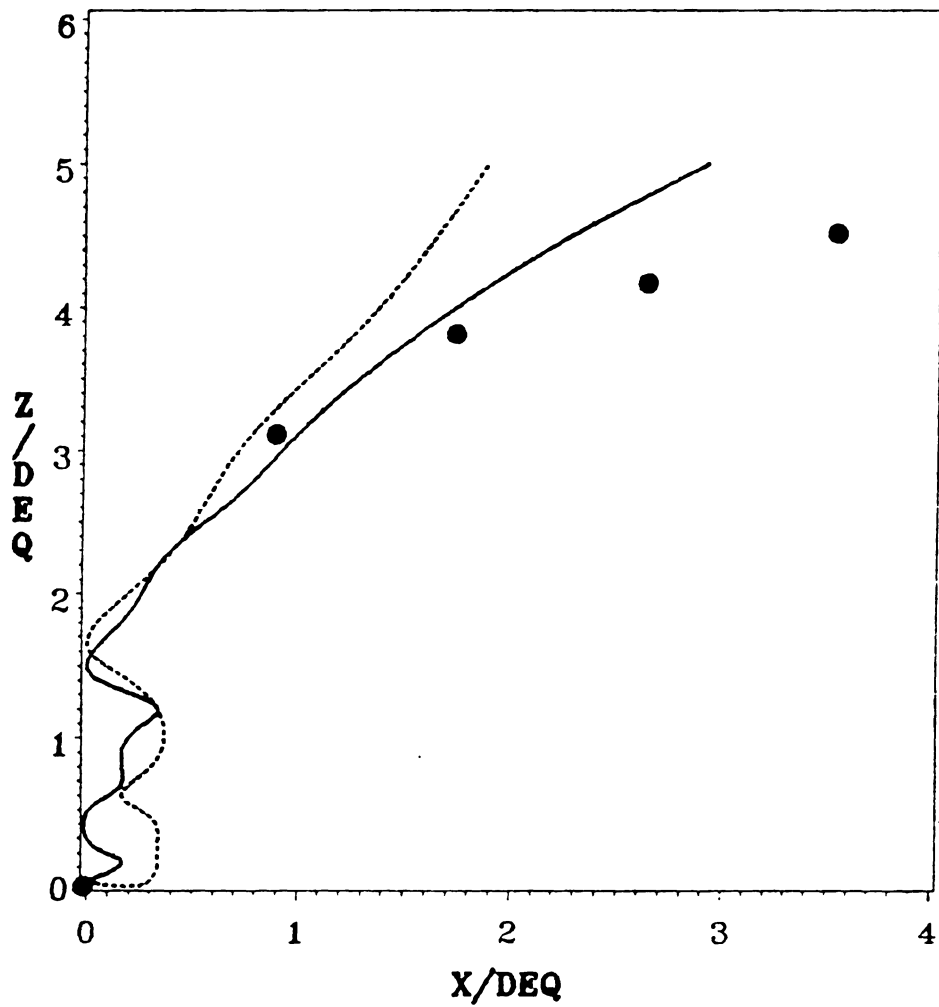


Figure 38. Dual Rectangular Jets in a Crossflow at $R=4$: Comparison of Jet Trajectory

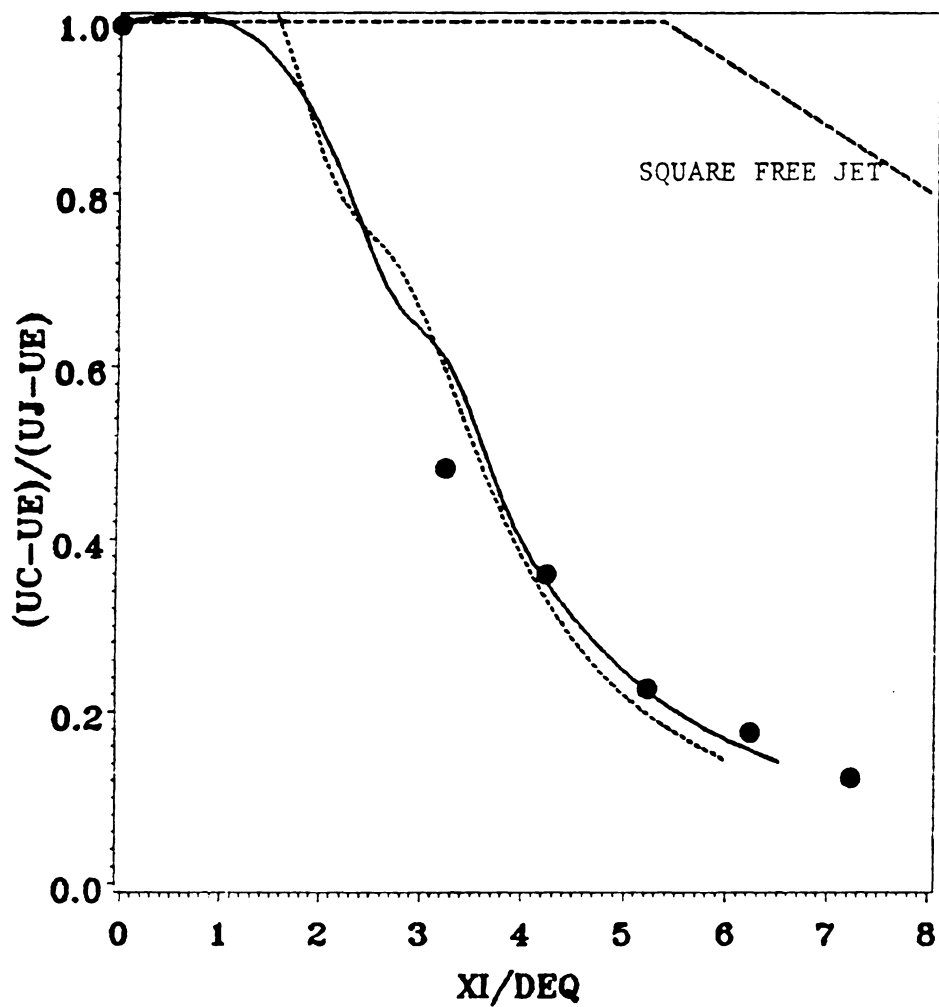


Figure 39. Dual Rectangular Jets in a Crossflow at $R=4$: Comparison of Axial Velocity Decay

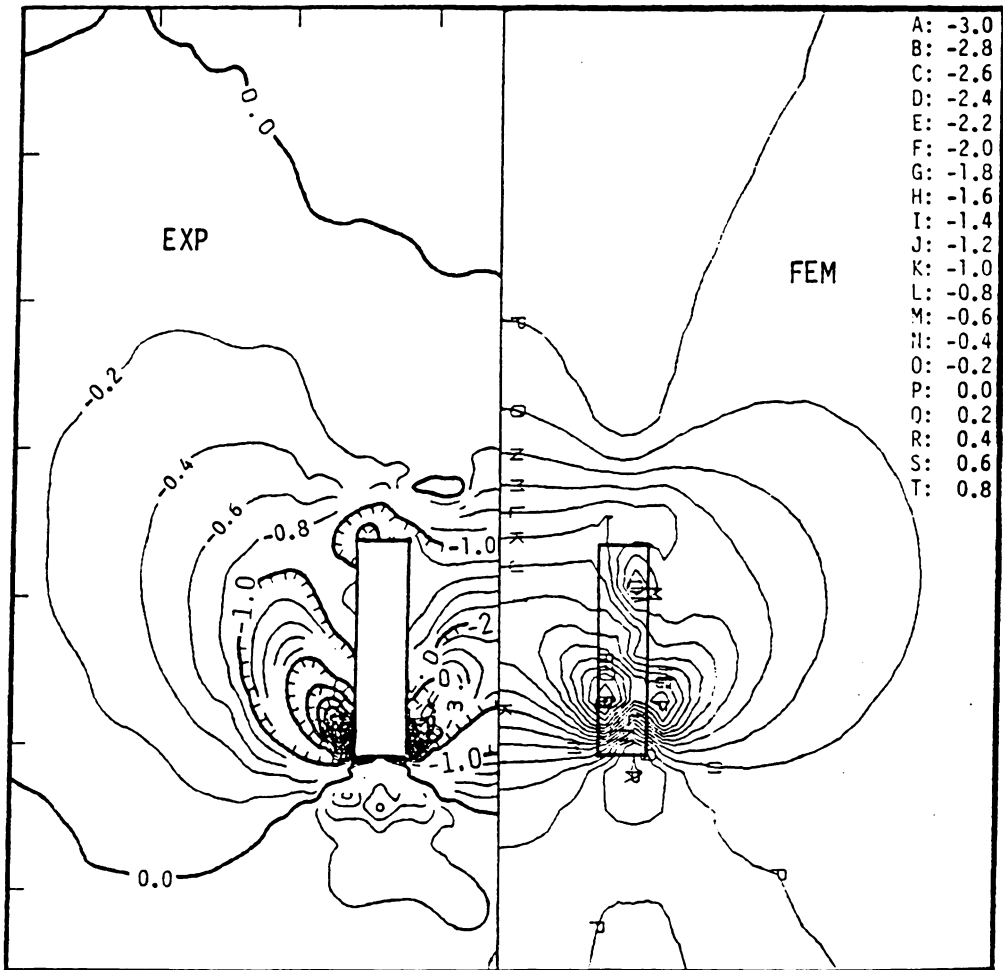
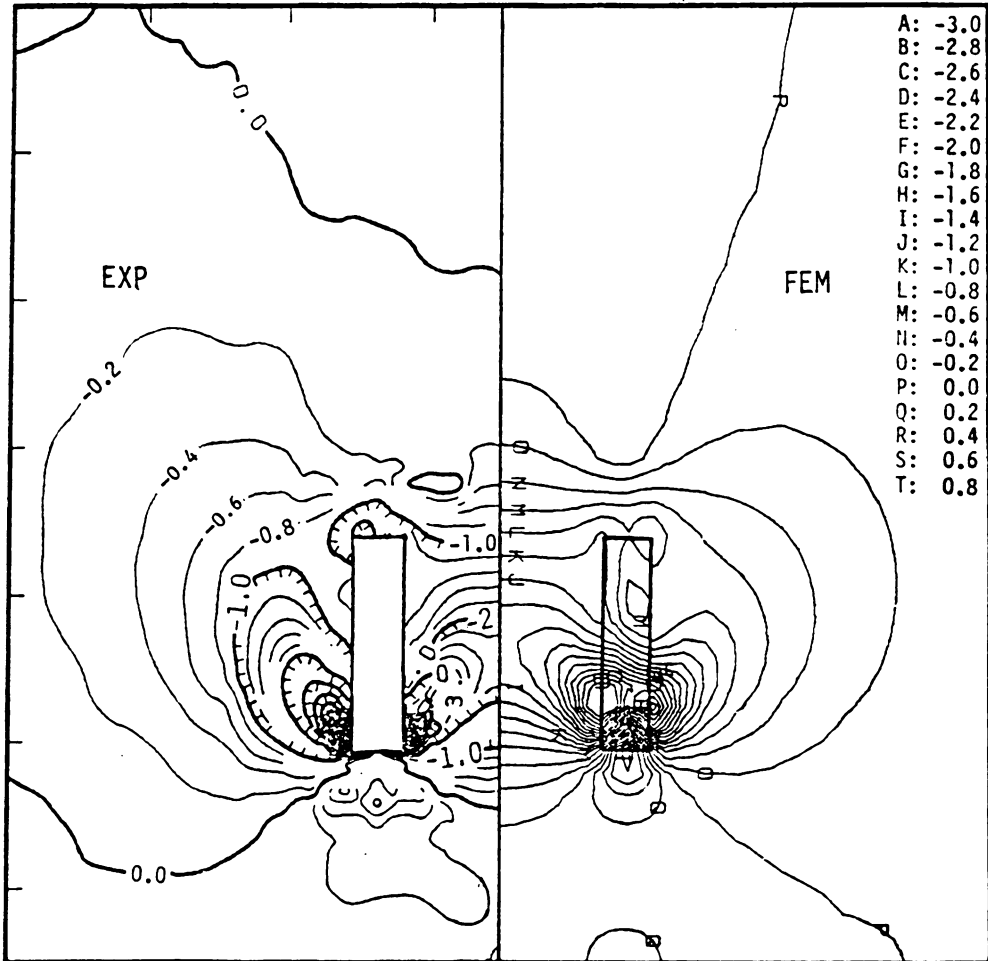


Figure 40. Dual Rectangular Jets in a Crossflow at $R = 4$: Comparison of Surface Pressure coefficient: (a) Coarse Mesh



Dual Rectangular Jets in a Crossflow at $R=4$: Comparison of Surface Pressure coefficient (b) Fine Mesh

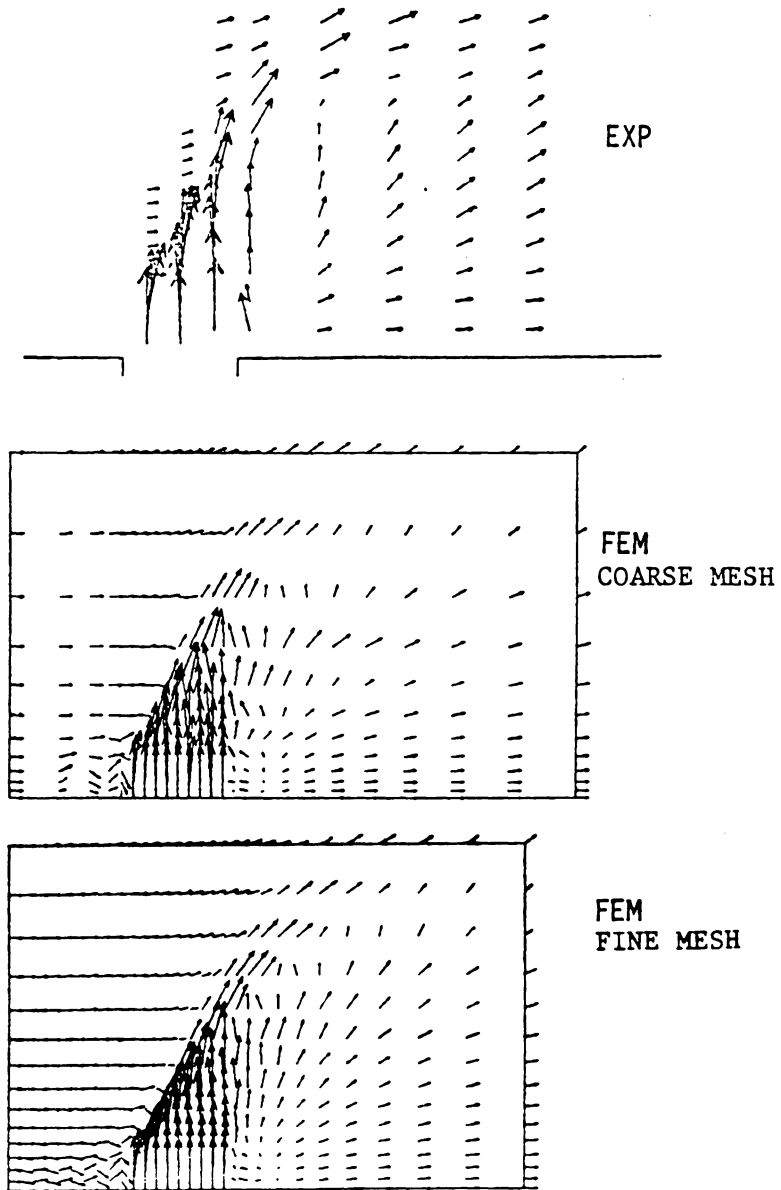


Figure 41. Dual Rectangular Jets in a Crossflow at $R = 4$: Comparison of Velocity Vector Plots on the Plane of Nozzle Symmetry ($y/D = 0.0$)

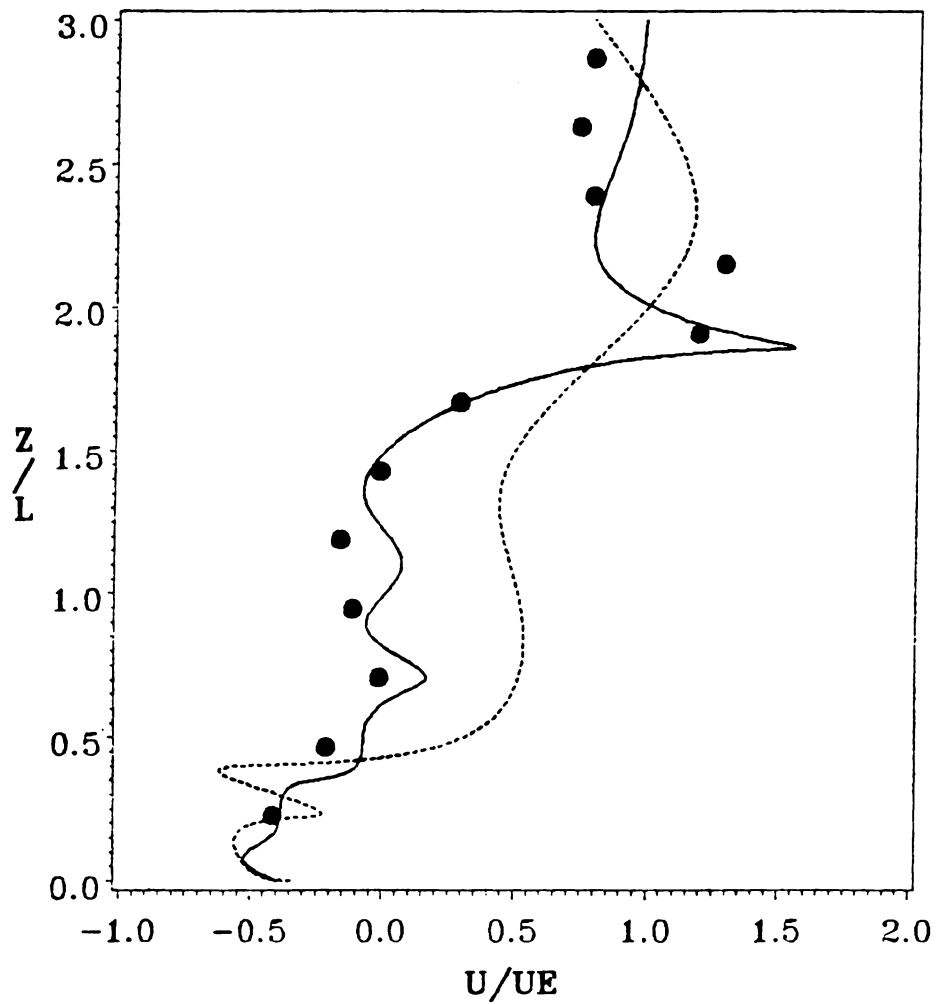


Figure 42. Dual Rectangular Jets in a Crossflow at $R=4$: Comparison of Streamwise Velocity Profiles at $x/D=1.0$ and $y/D=0.0$: circle - measured data [80], broken line - coarse mesh, solid line - fine mesh

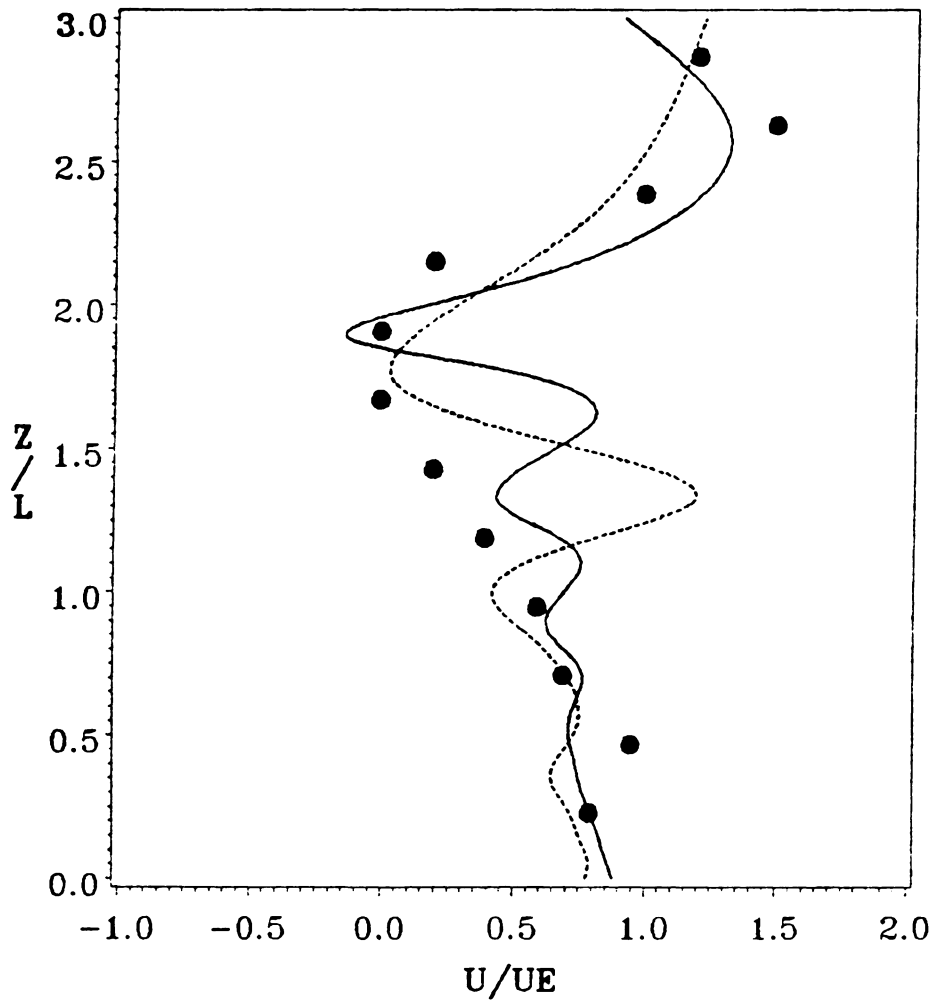


Figure 43. Dual Rectangular Jets in a Crossflow at $R=4$: Comparison of Streamwise Velocity Profiles at $x/D=2.0$ and $y/D=0.0$: circle - measured data [80], broken line - coarse mesh, solid line - fine mesh

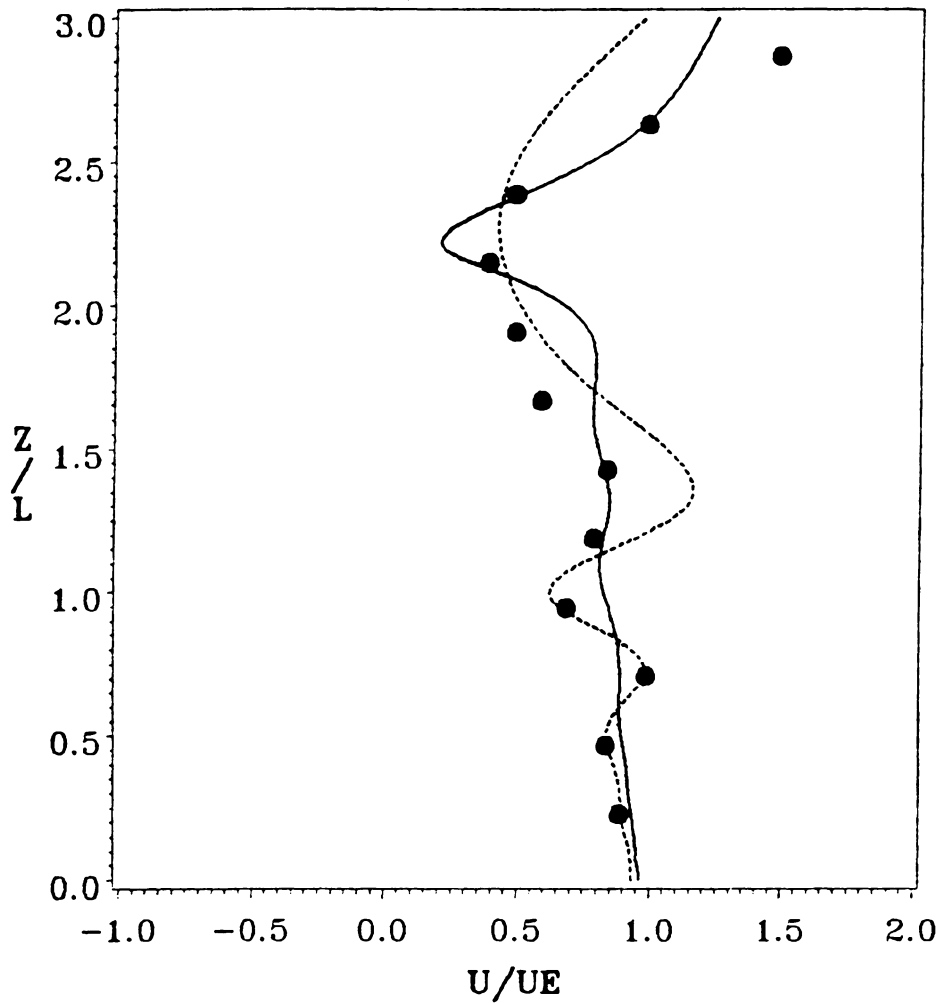


Figure 44. Dual Rectangular Jets in a Crossflow at $R=4$: Comparison of Streamwise Velocity Profiles at $x/D=3.0$ and $y/D=0.0$: circle - measured data [80], broken line - coarse mesh, solid line - fine mesh

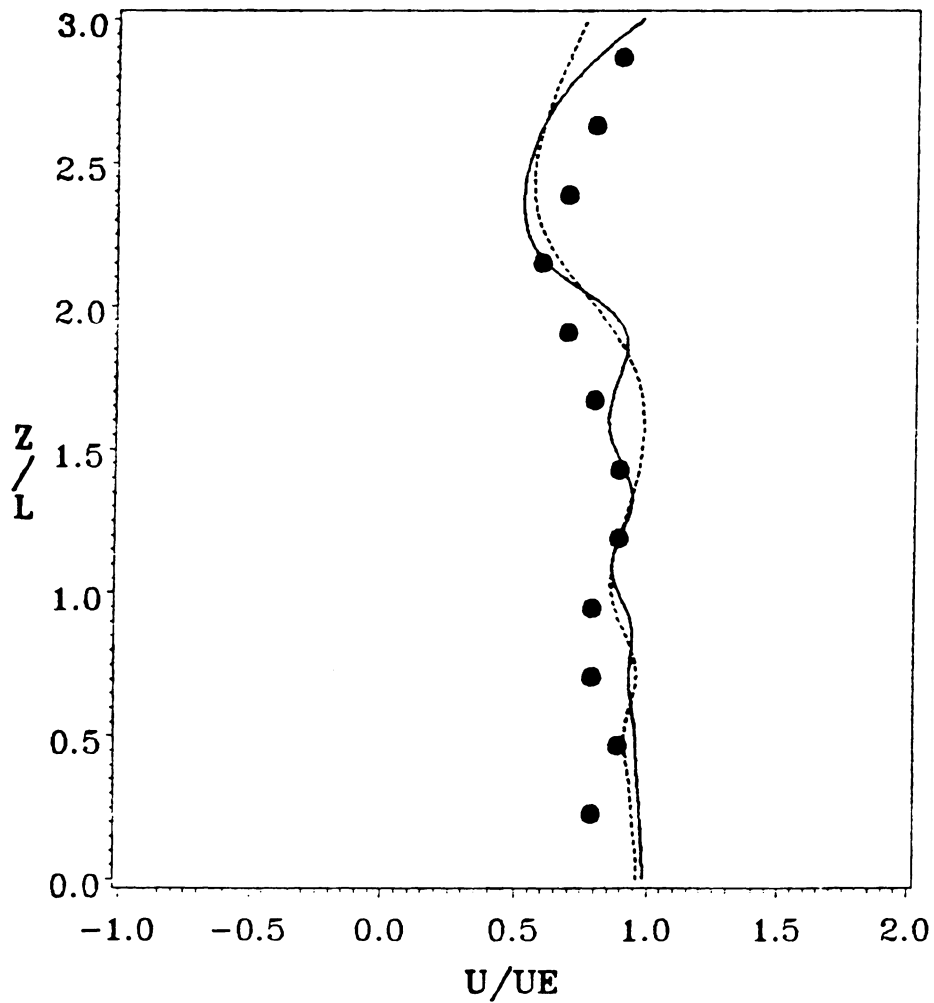


Figure 45. Dual Rectangular Jets in a Crossflow at $R=4$: Comparison of Streamwise Velocity Profiles at $x/D=4.0$ and $y/D=0.0$: circle - measured data [80], broken line - coarse mesh, solid line - fine mesh

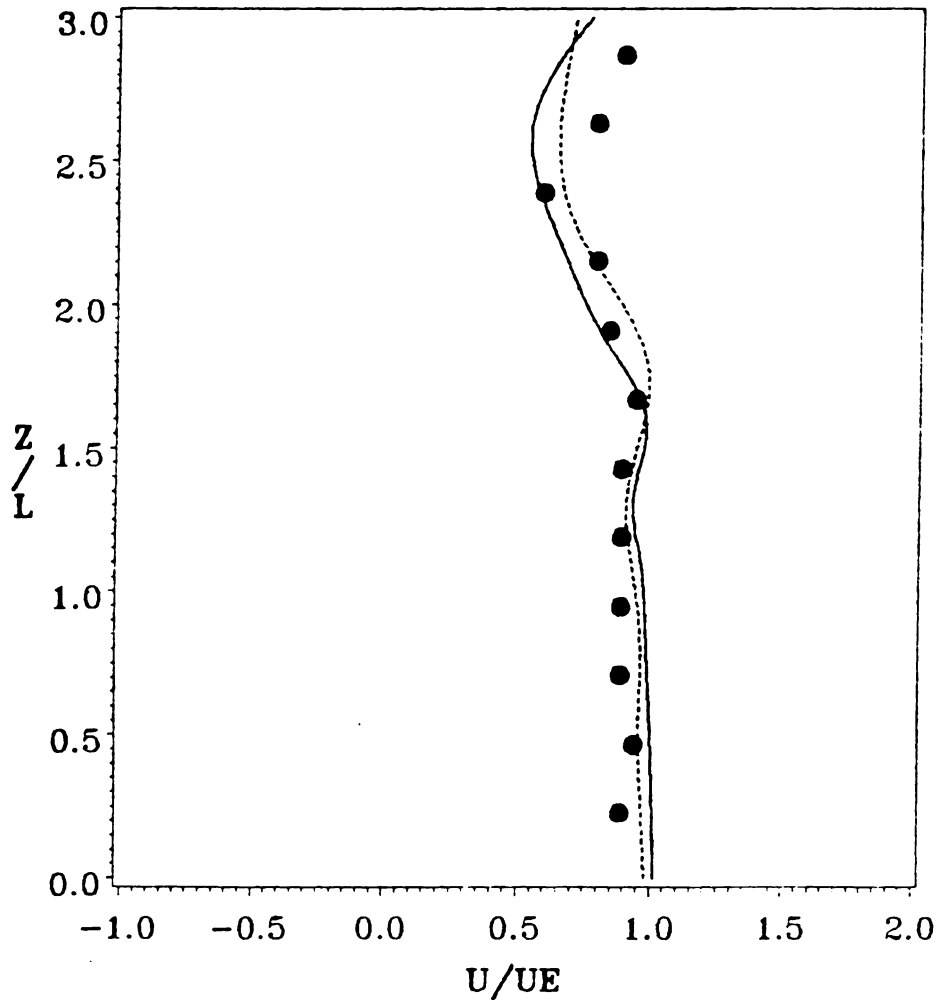


Figure 46. Dual Rectangular Jets in a Crossflow at $R=4$: Comparison of Streamwise Velocity Profiles at $x/D=5.0$ and $y/D=0.0$: circle - measured data [80], broken line - coarse mesh, solid line - fine mesh

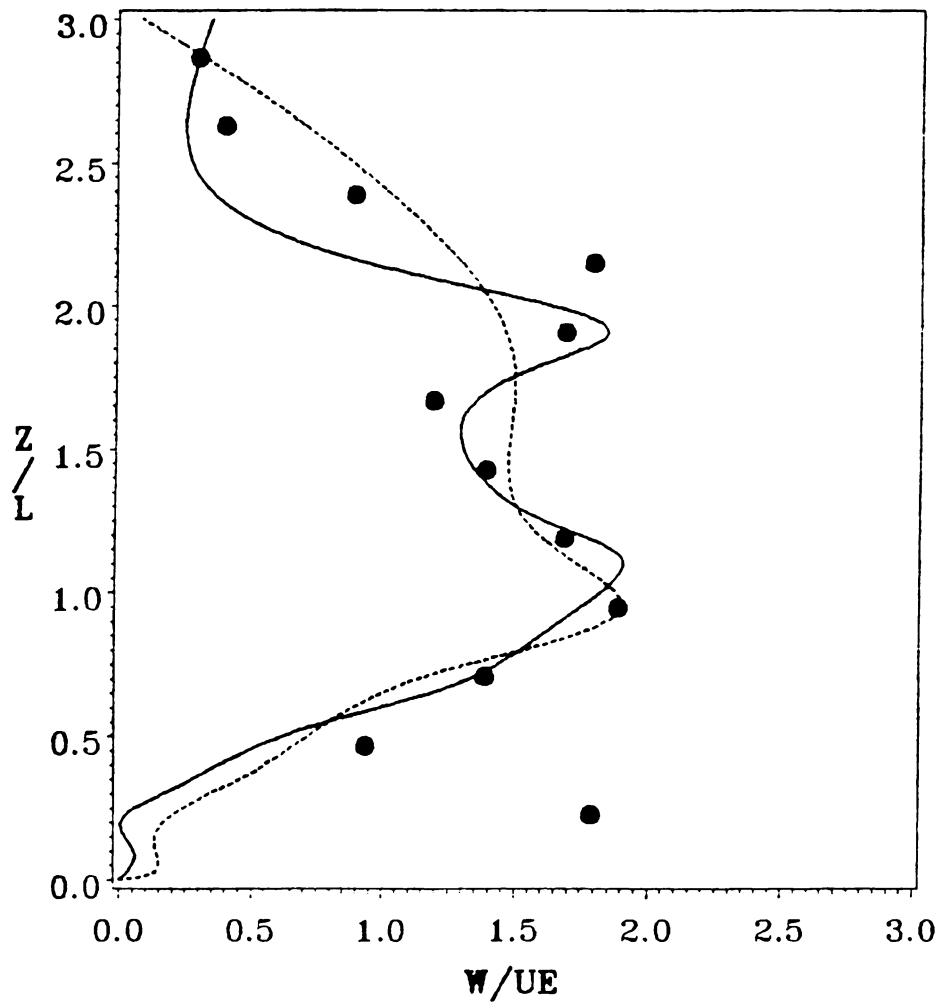


Figure 47. Dual Rectangular Jets in a Crossflow at $R=4$: Comparison of Normal Velocity Profiles at $x/D=1.0$ and $y/D=0.0$: circle - measured data [80], broken line - coarse mesh, solid line - fine mesh

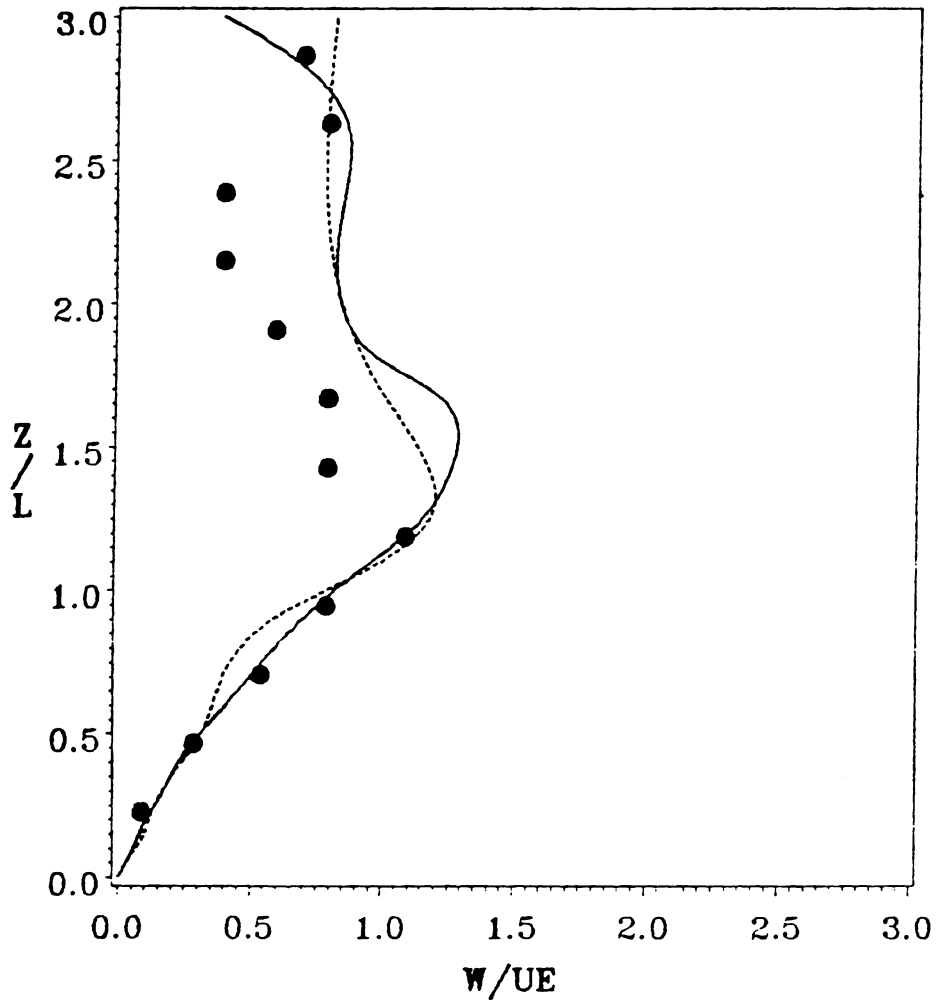


Figure 48. Dual Rectangular Jets in a Crossflow at $R=4$: Comparison of Normal Velocity Profiles at $x/D=2.0$ and $y/D=0.0$: circle - measured data [80], broken line - coarse mesh, solid line - fine mesh

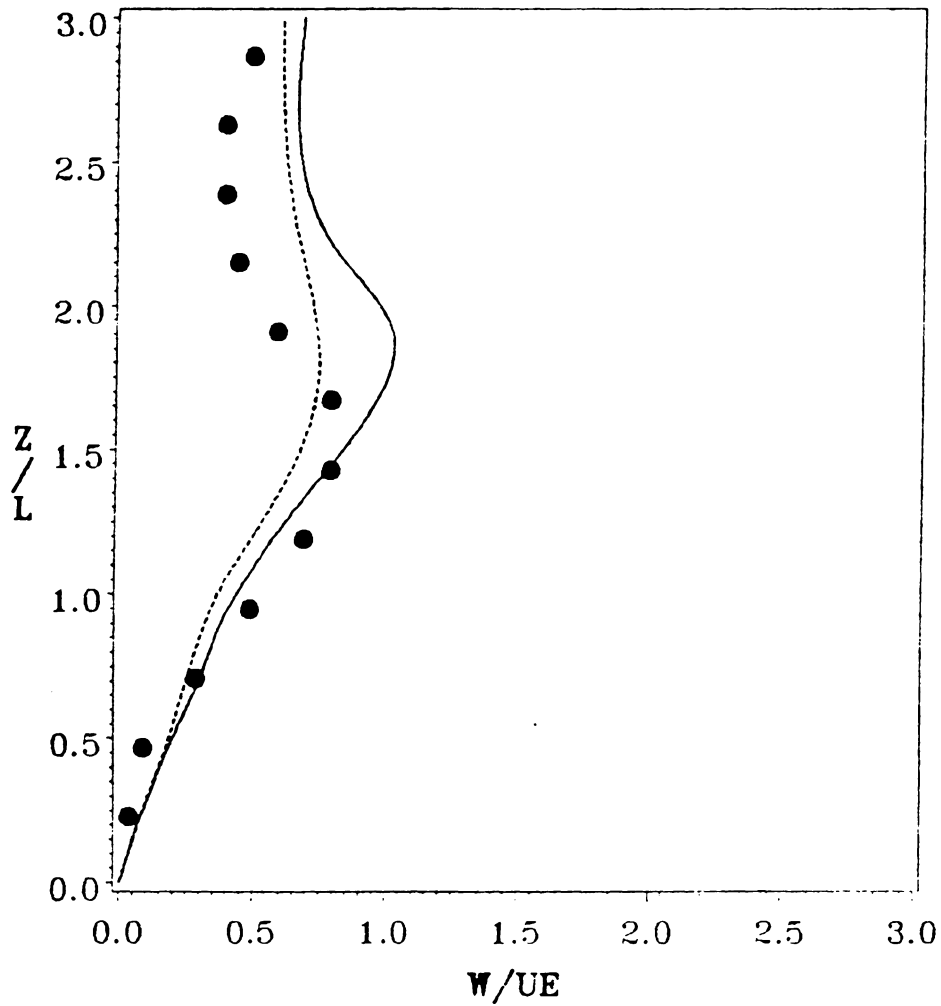


Figure 49. Dual Rectangular Jets in a Crossflow at $R=4$: Comparison of Normal Velocity Profiles at $x/D=3.0$ and $y/D=0.0$: circle - measured data [80], broken line - coarse mesh, solid line - fine mesh

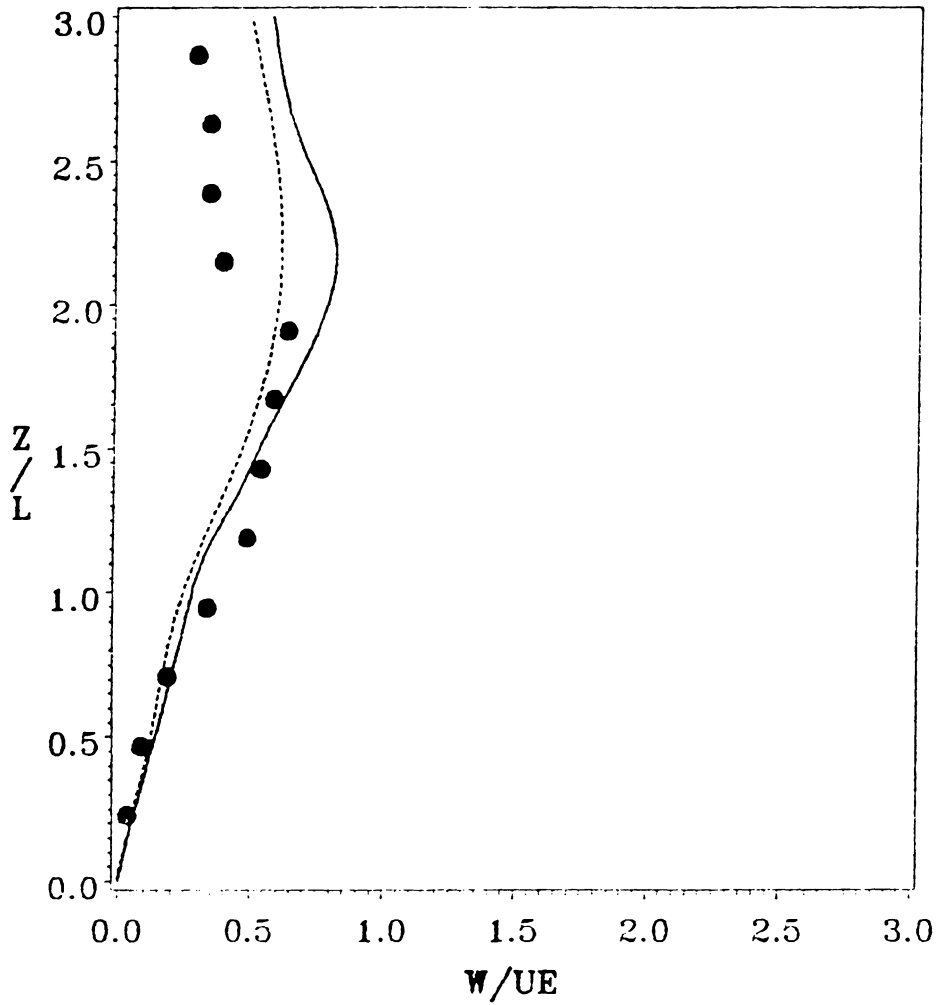


Figure 50. Dual Rectangular Jets in a Crossflow at $R=4$: Comparison of Normal Velocity Profiles at $x/D=4.0$ and $y/D=0.0$: circle - measured data [80], broken line - coarse mesh, solid line - fine mesh

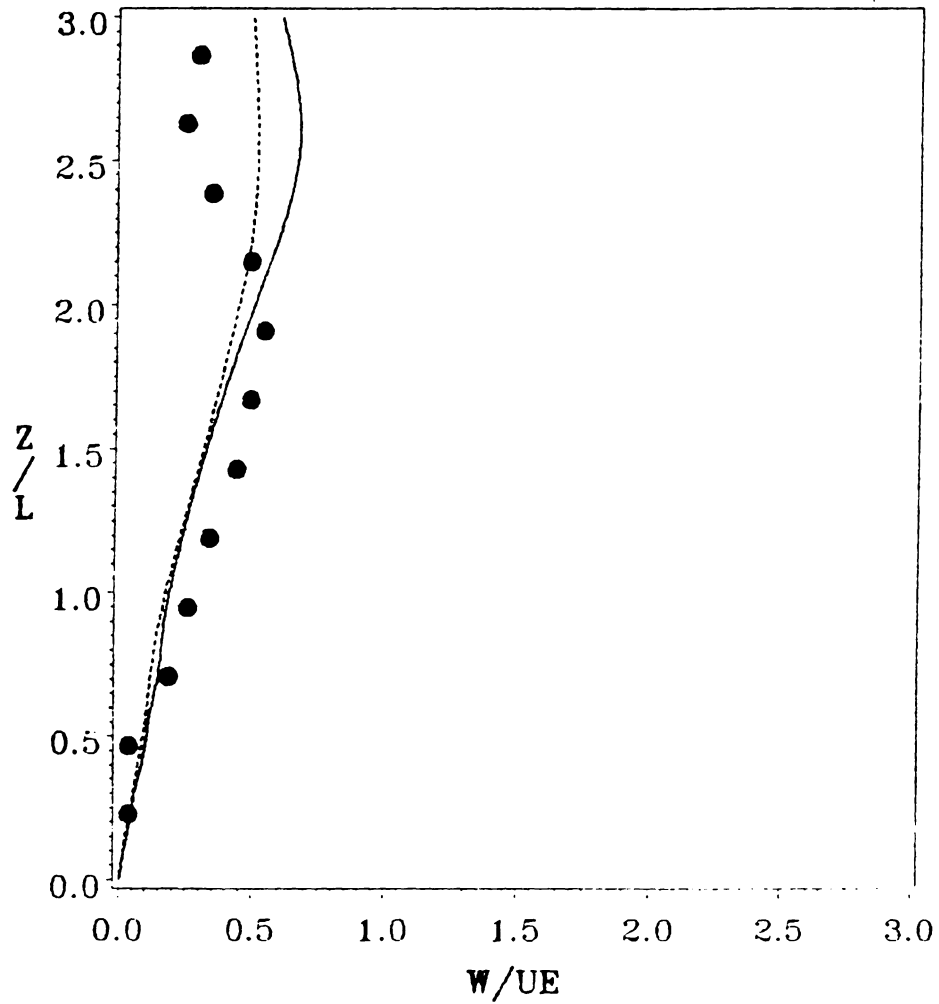


Figure 51. Dual Rectangular Jets in a Crossflow at $R=4$: Comparison of Normal Velocity Profiles at $x/D=5.0$ and $y/D=0.0$: circle - measured data [80], broken line - coarse mesh, solid line - fine mesh

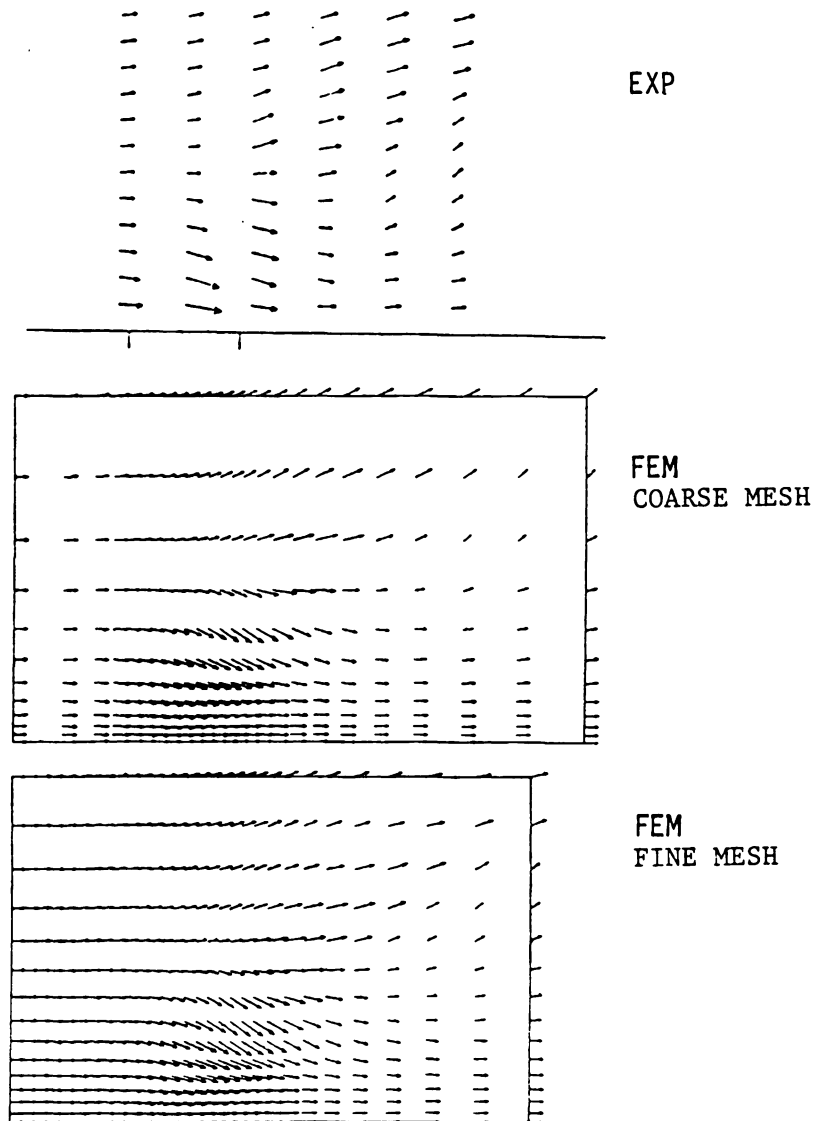


Figure 52. Dual Rectangular Jets in a Crossflow at $R = 4$: Comparison of Velocity Vector Plots on the Plane of Flow Symmetry ($y/D = -1.0$)

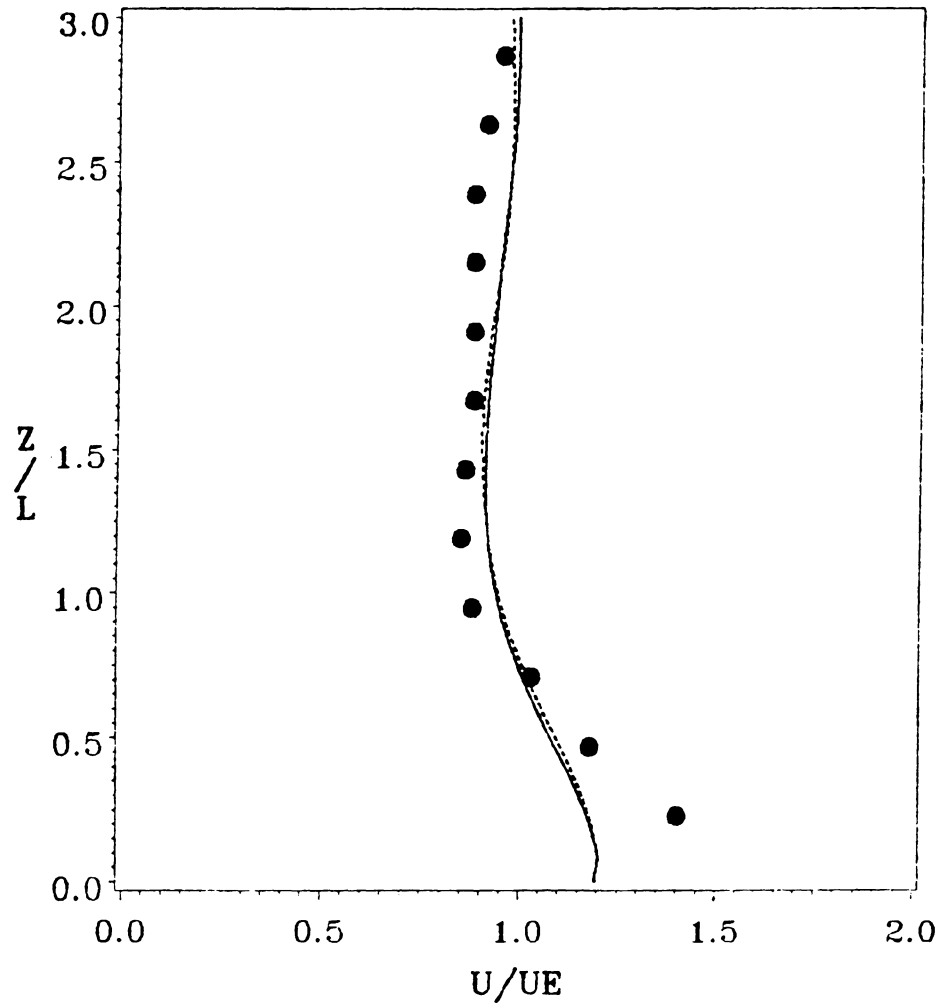


Figure 53. Dual Rectangular Jets in a Crossflow at $R=4$: Comparison of Streamwise Velocity Profiles at $x/D=-1.0$ and $y/D=-1.0$: circle - measured data [80], broken line - coarse mesh, solid line - fine mesh

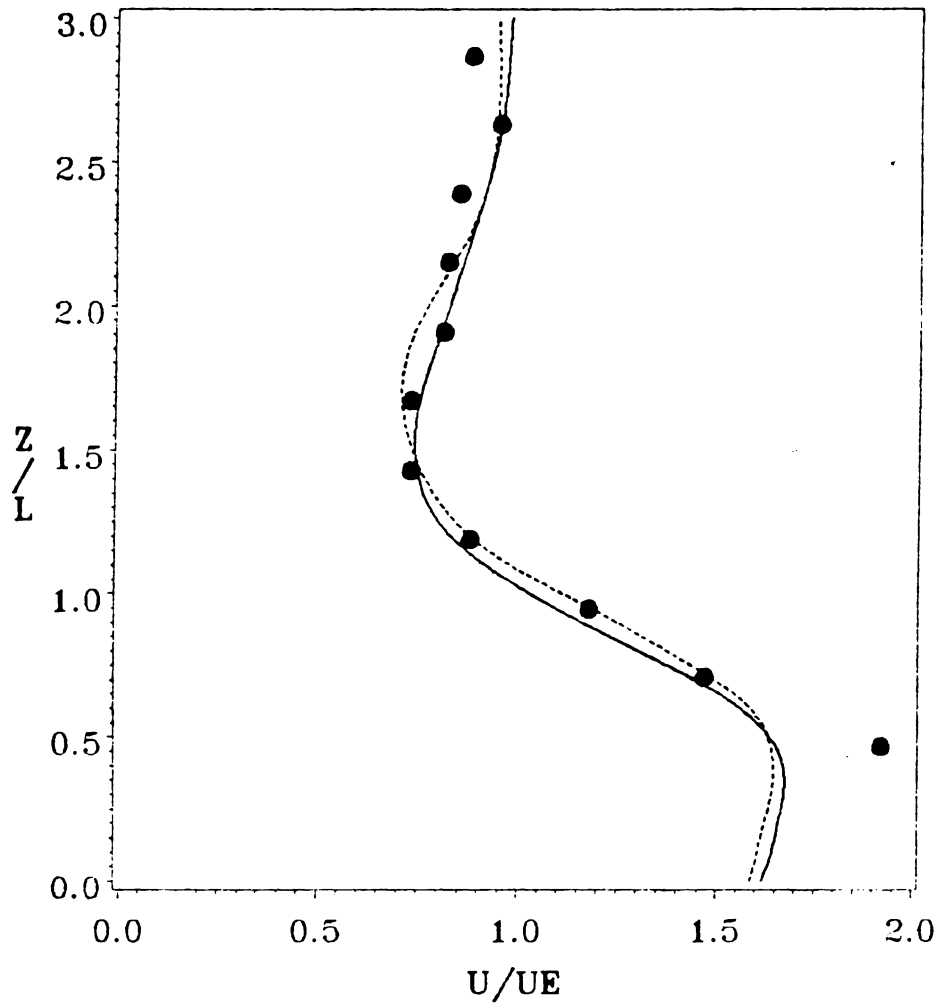


Figure 54. Dual Rectangular Jets in a Crossflow at $R=4$: Comparison of Streamwise Velocity Profiles at $x/D=0.0$ and $y/D=-1.0$: circle - measured data [80], broken line - coarse mesh, solid line - fine mesh

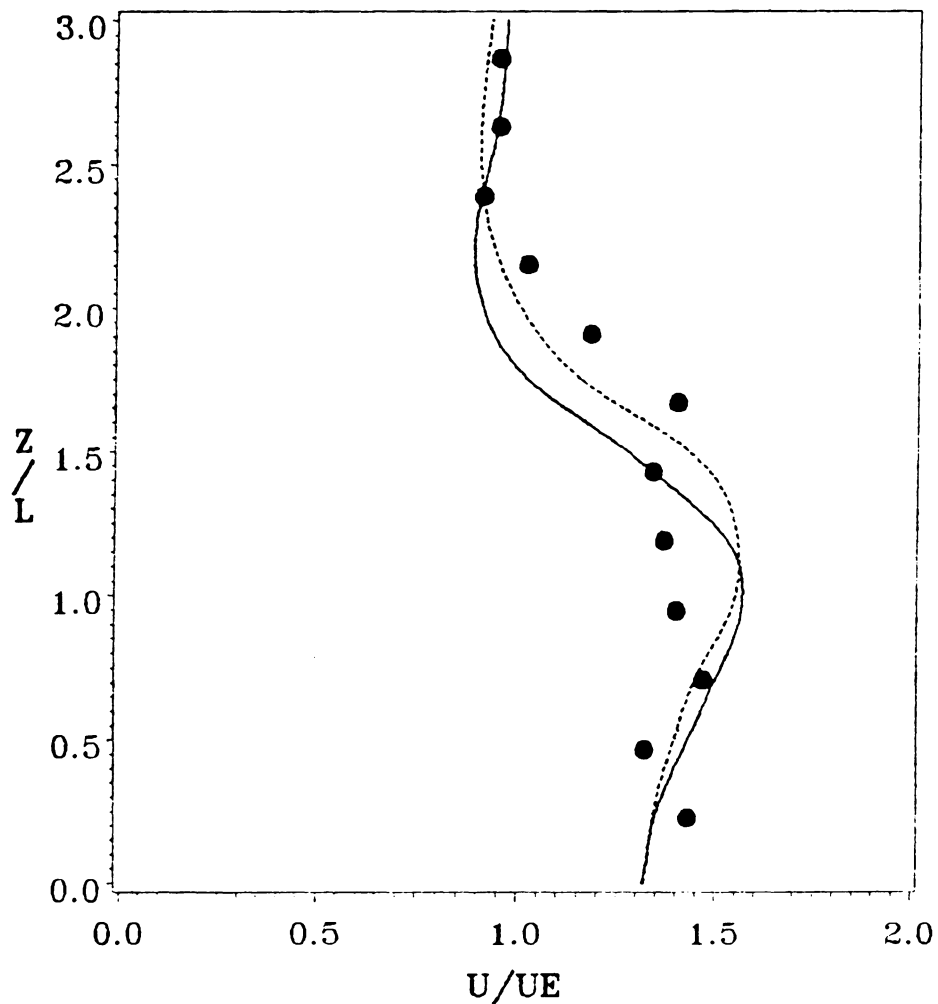


Figure 55. Dual Rectangular Jets in a Crossflow at $R=4$: Comparison of Streamwise Velocity Profiles at $x/D=1.0$ and $y/D=-1.0$: circle - measured data [80], broken line - coarse mesh, solid line - fine mesh

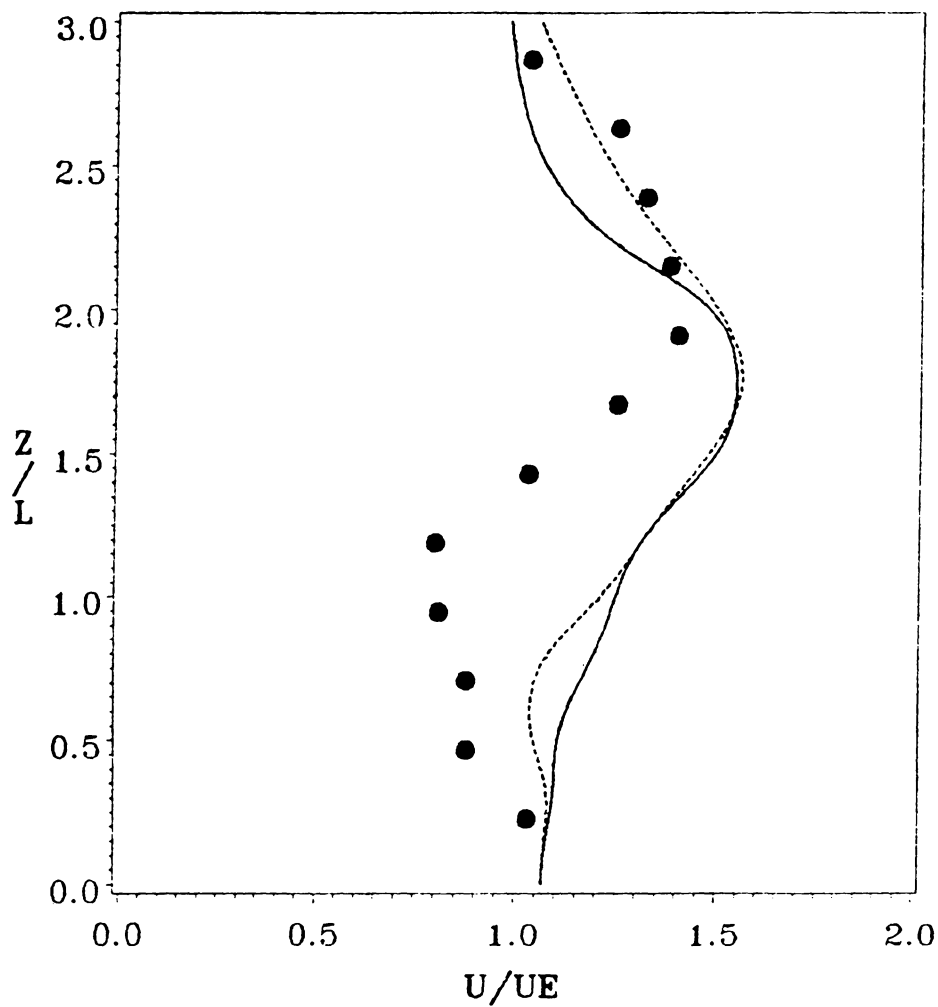


Figure 56. Dual Rectangular Jets in a Crossflow at $R=4$: Comparison of Streamwise Velocity Profiles at $x/D=2.0$ and $y/D=-1.0$: circle - measured data [80], broken line - coarse mesh, solid line - fine mesh

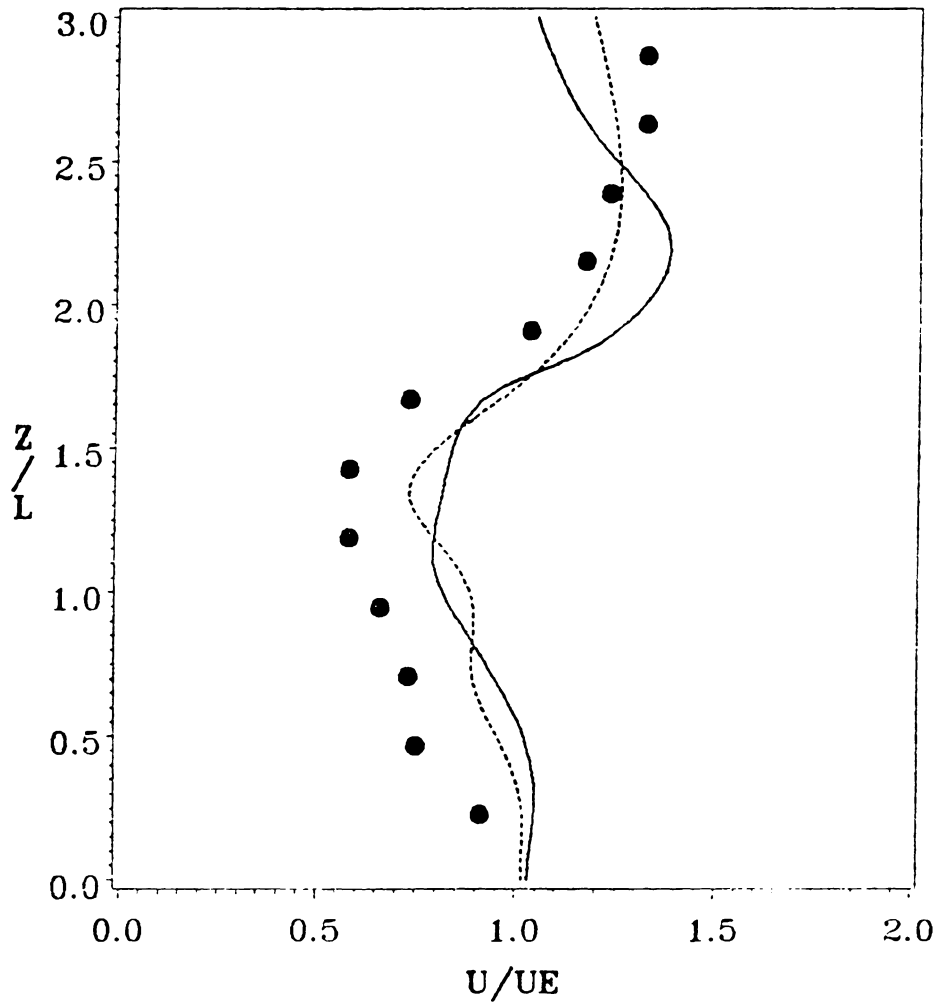


Figure 57. Dual Rectangular Jets in a Crossflow at $R=4$: Comparison of Streamwise Velocity Profiles at $x/D=3.0$ and $y/D=-1.0$: circle - measured data [80], broken line - coarse mesh, solid line - fine mesh

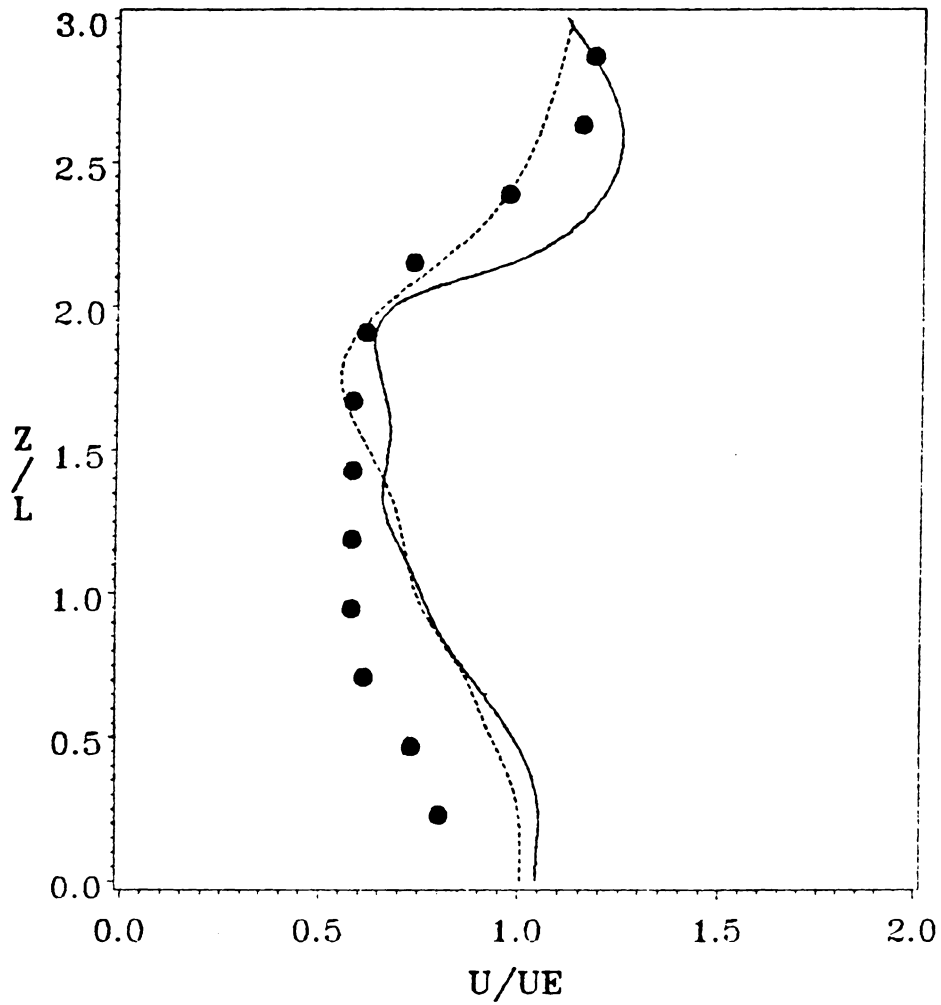


Figure 58. Dual Rectangular Jets in a Crossflow at $R=4$: Comparison of Streamwise Velocity Profiles at $x/D=4.0$ and $y/D=-1.0$: circle - measured data [80], broken line - coarse mesh, solid line - fine mesh

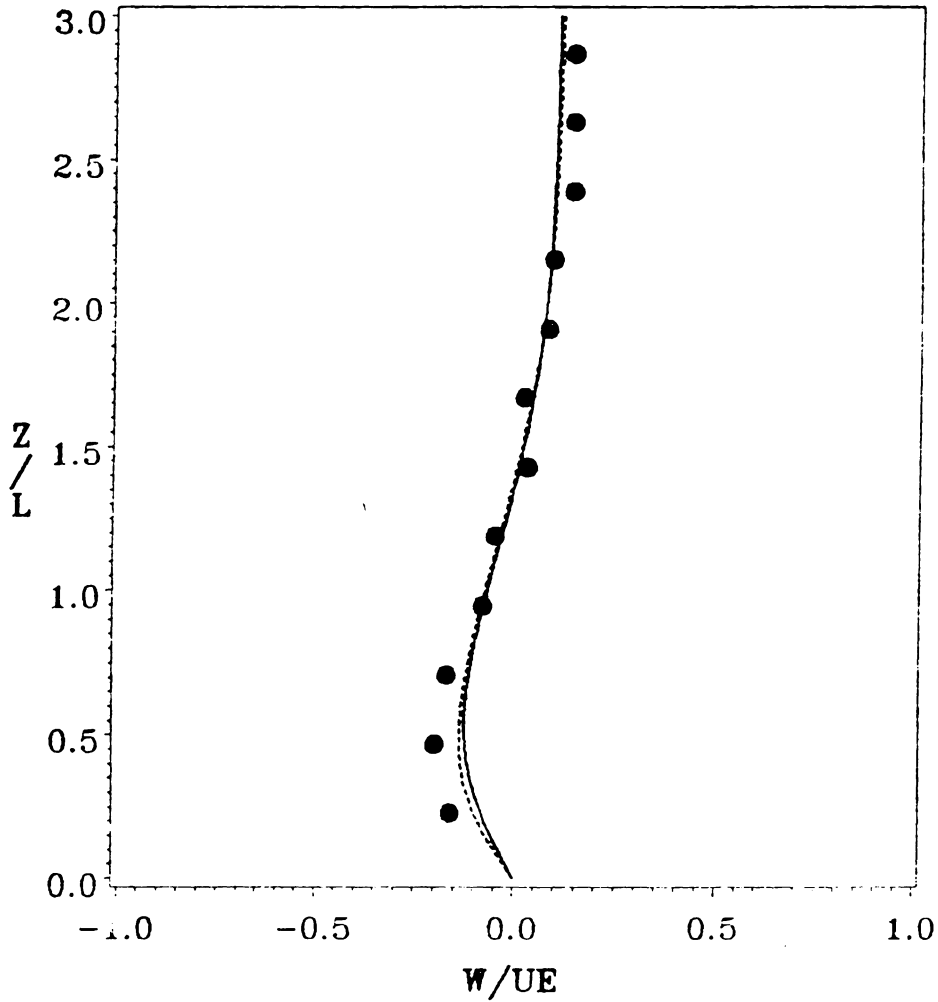


Figure 59. Dual Rectangular Jets in a Crossflow at $R=4$: Comparison of Normal Velocity Profiles at $x/D=-1.0$ and $y/D=-1.0$: circle - measured data [80], broken line - coarse mesh, solid line - fine mesh

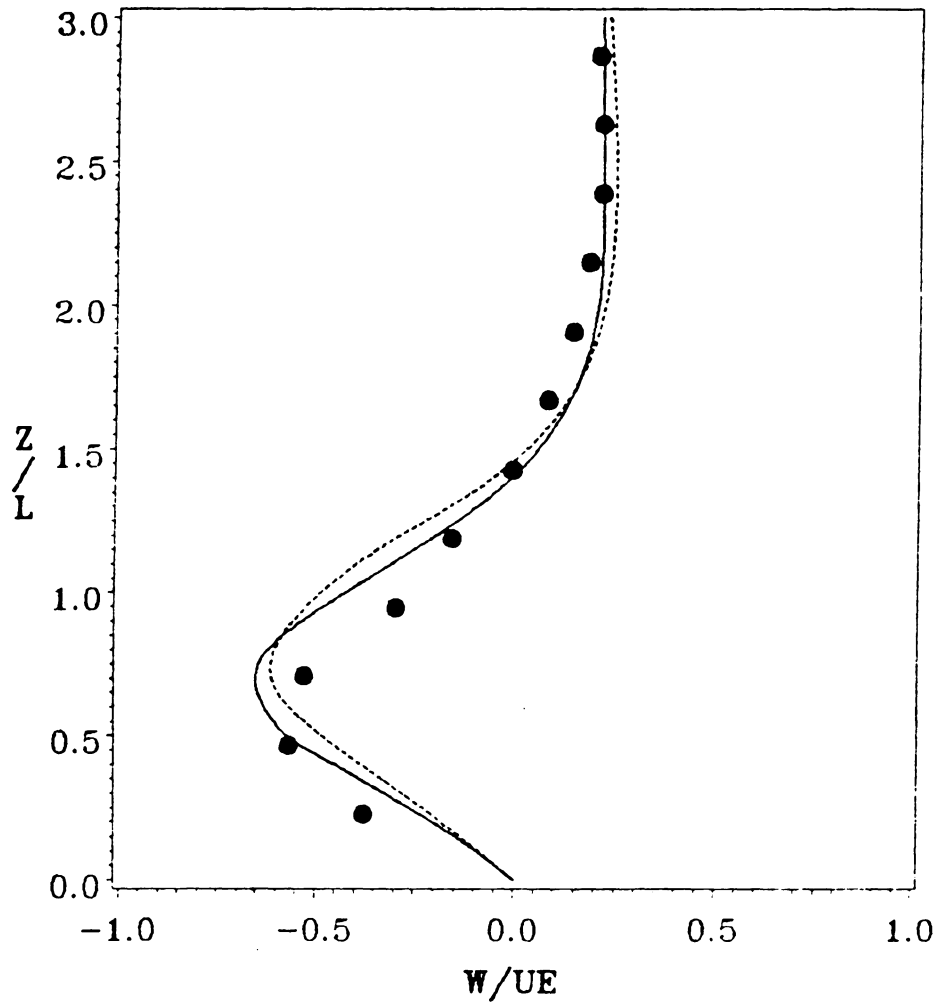


Figure 60. Dual Rectangular Jets in a Crossflow at $R = 4$: Comparison of Normal Velocity Profiles at $x/D = 0.0$ and $y/D = -1.0$: circle - measured data [80], broken line - coarse mesh, solid line - fine mesh

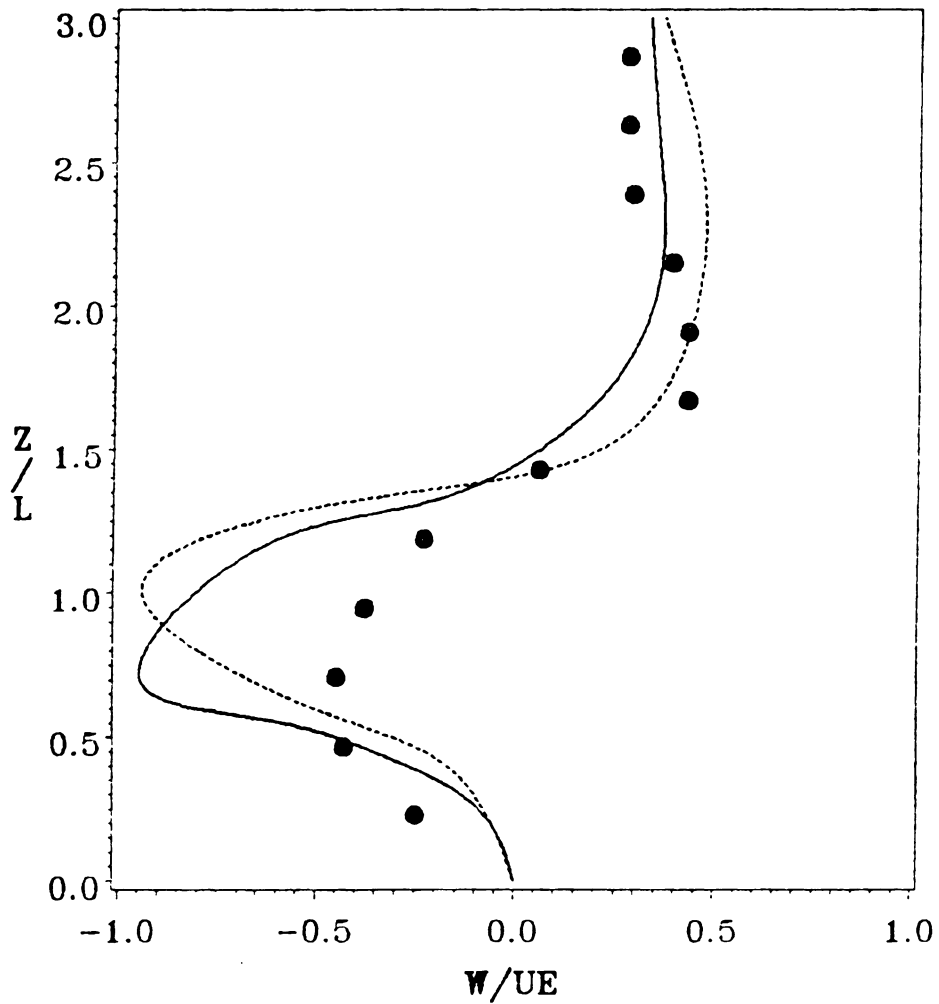


Figure 61. Dual Rectangular Jets in a Crossflow at $R=4$: Comparison of Normal Velocity Profiles at $x/D=1.0$ and $y/D=-1.0$: circle - measured data [80], broken line - coarse mesh, solid line - fine mesh

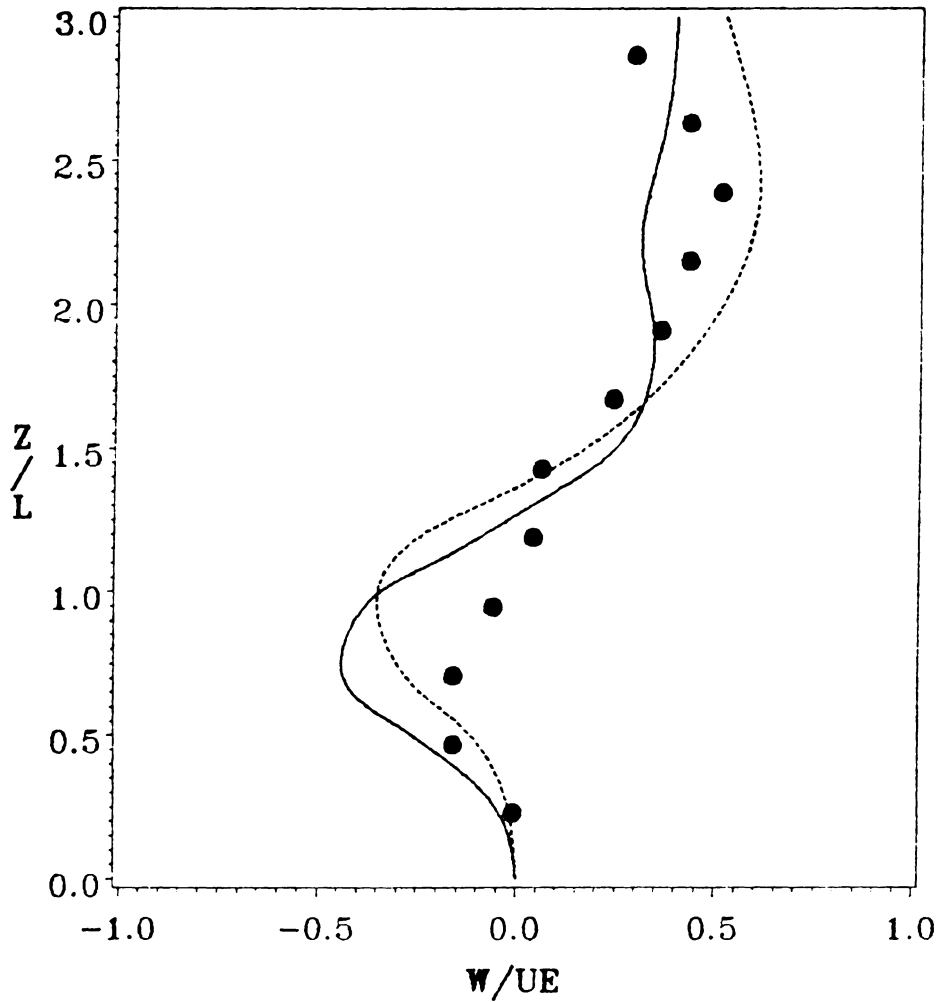


Figure 62. Dual Rectangular Jets in a Crossflow at $R=4$: Comparison of Normal Velocity Profiles at $x/D=2.0$ and $y/D=-1.0$: circle - measured data [80], broken line - coarse mesh, solid line - fine mesh

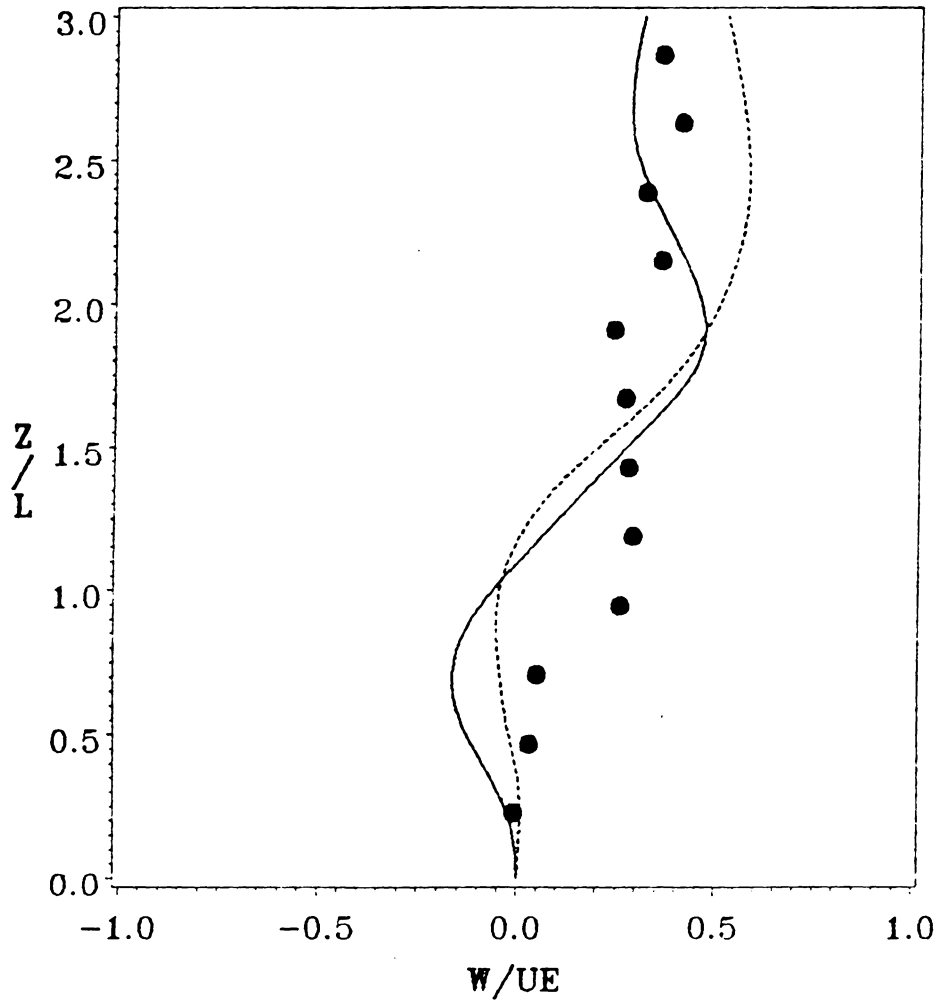


Figure 63. Dual Rectangular Jets in a Crossflow at $R = 4$: Comparison of Normal Velocity Profiles at $x/D = 3.0$ and $y/D = -1.0$: circle - measured data [80], broken line - coarse mesh, solid line - fine mesh

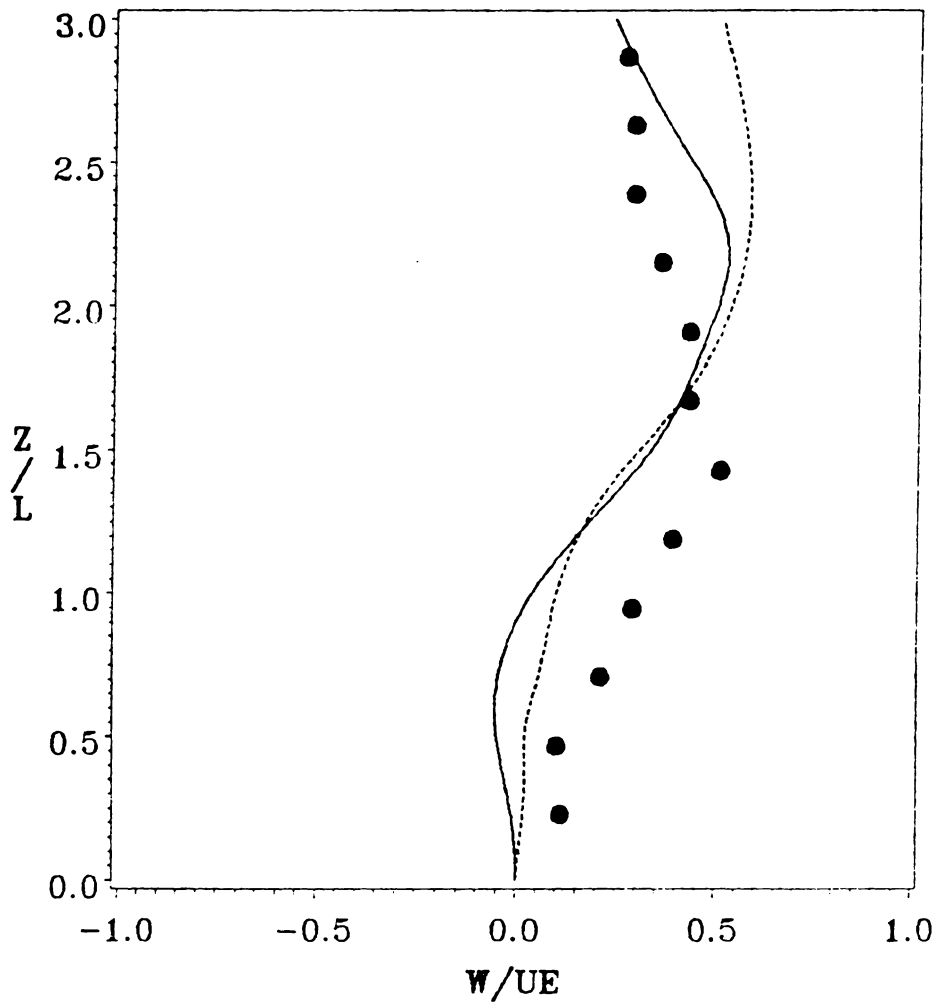


Figure 64. Dual Rectangular Jets in a Crossflow at $R=4$: Comparison of Normal Velocity Profiles at $x/D=4.0$ and $y/D=-1.0$: circle - measured data [80], broken line - coarse mesh, solid line - fine mesh

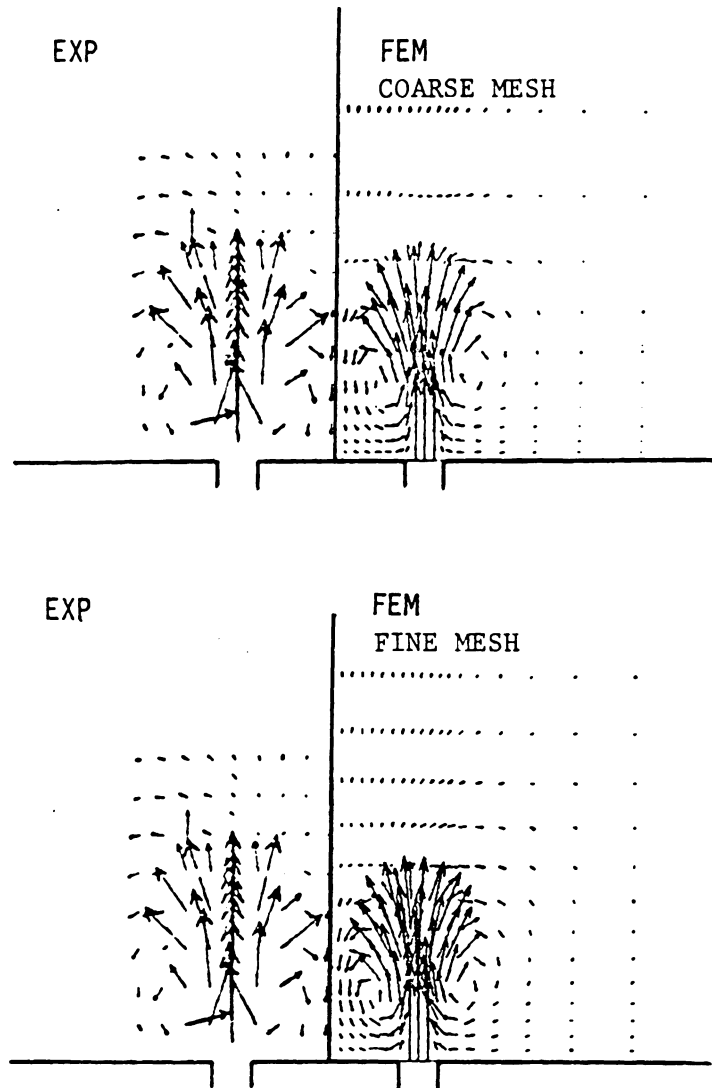


Figure 65. Dual Rectangular Jets in a Crossflow at $R = 4$: Comparison of Velocity Vector Plots on the Crossflow Plane ($x/D = 0.0$)

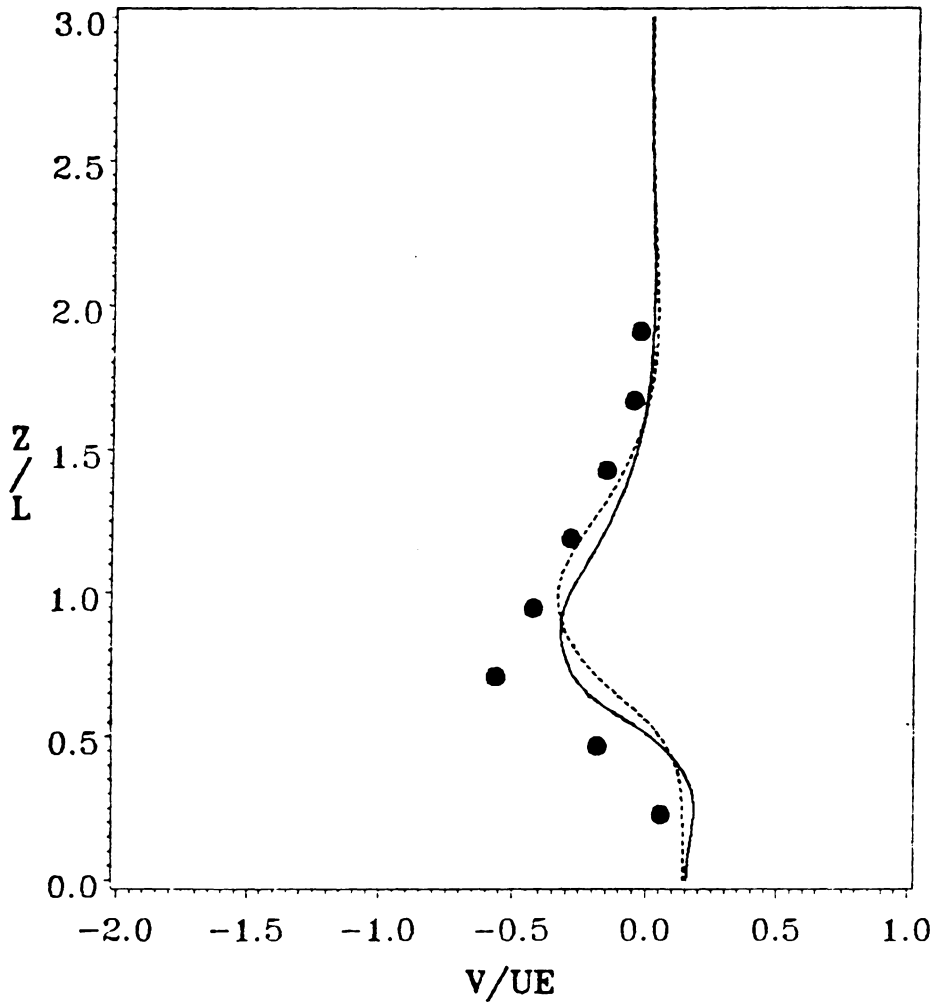


Figure 66. Dual Rectangular Jets in a Crossflow at $R=4$: Comparison of Transverse Velocity Profiles at $x/D=0.0$ and $y/D=-0.75$: circle - measured data [80], broken line - coarse mesh, solid line - fine mesh

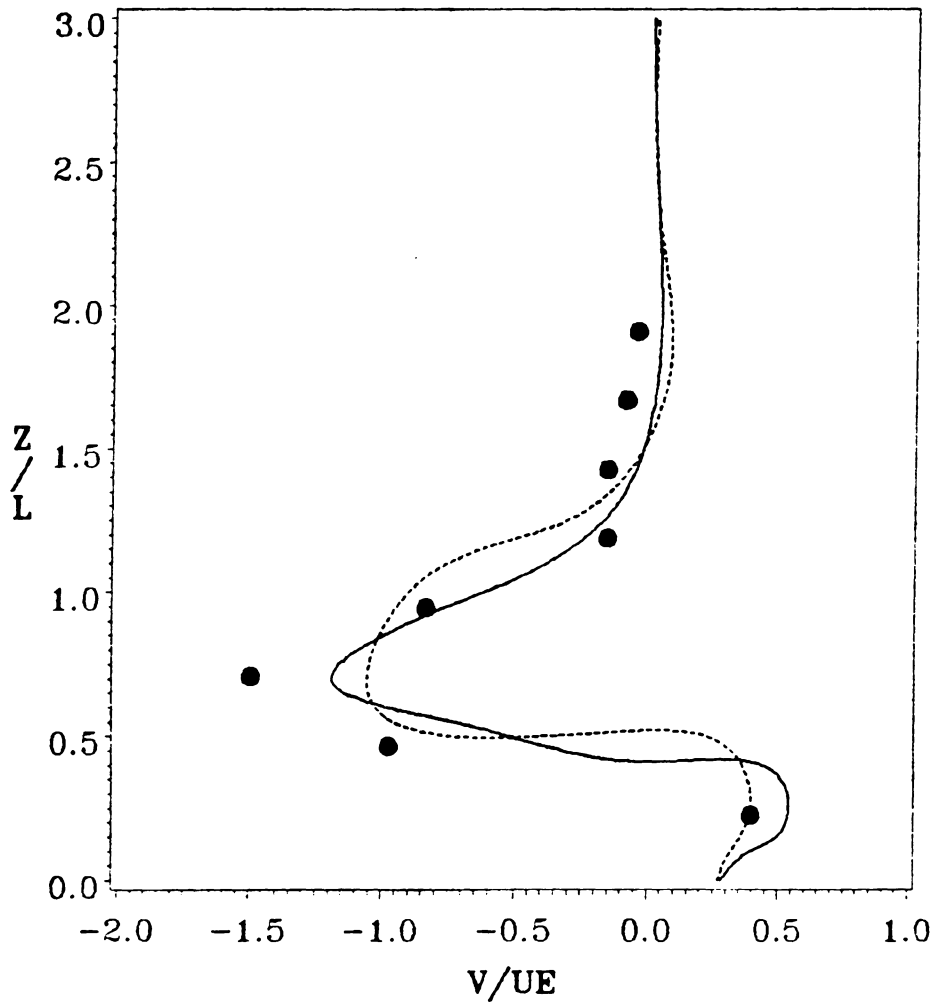


Figure 67. Dual Rectangular Jets in a Crossflow at $R=4$: Comparison of Transverse Velocity Profiles at $x/D=0.0$ and $y/D=-0.5$: circle - measured data [80], broken line - coarse mesh, solid line - fine mesh

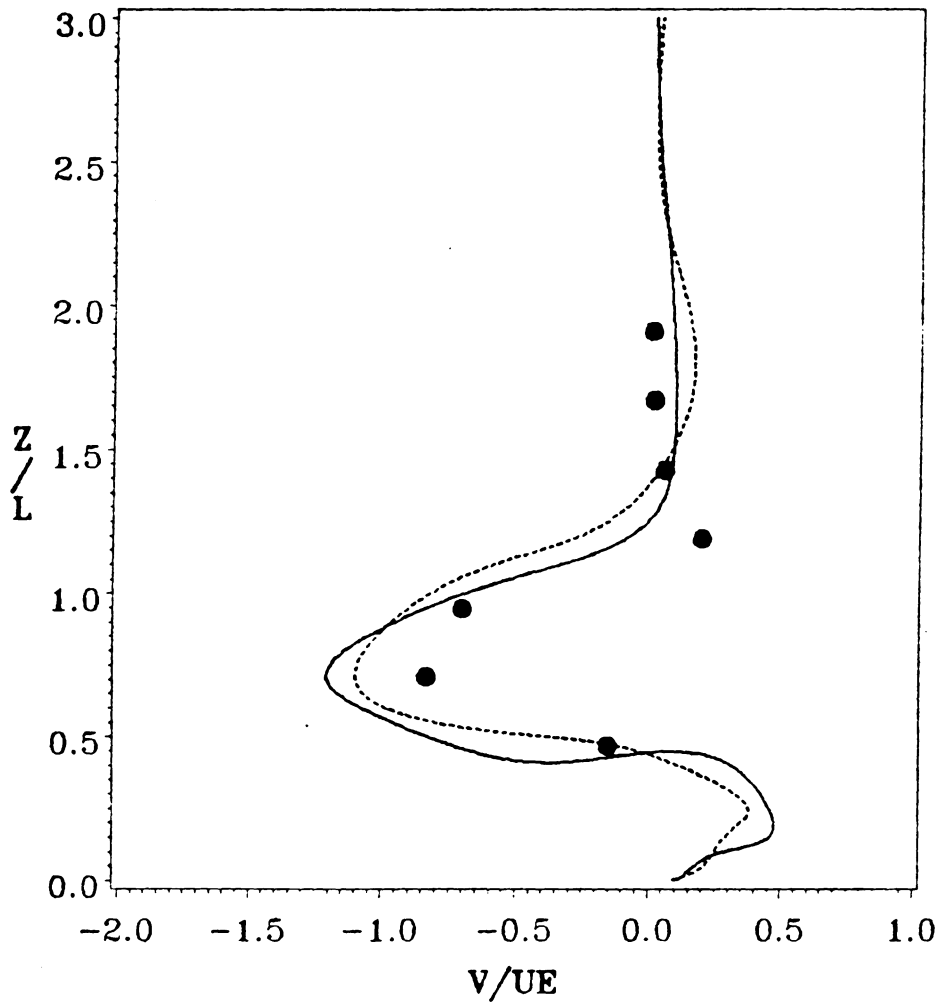


Figure 68. Dual Rectangular Jets in a Crossflow at $R=4$: Comparison of Transverse Velocity Profiles at $x/D=0.0$ and $y/D=-0.25$: circle - measured data [80], broken line - coarse mesh, solid line - fine mesh

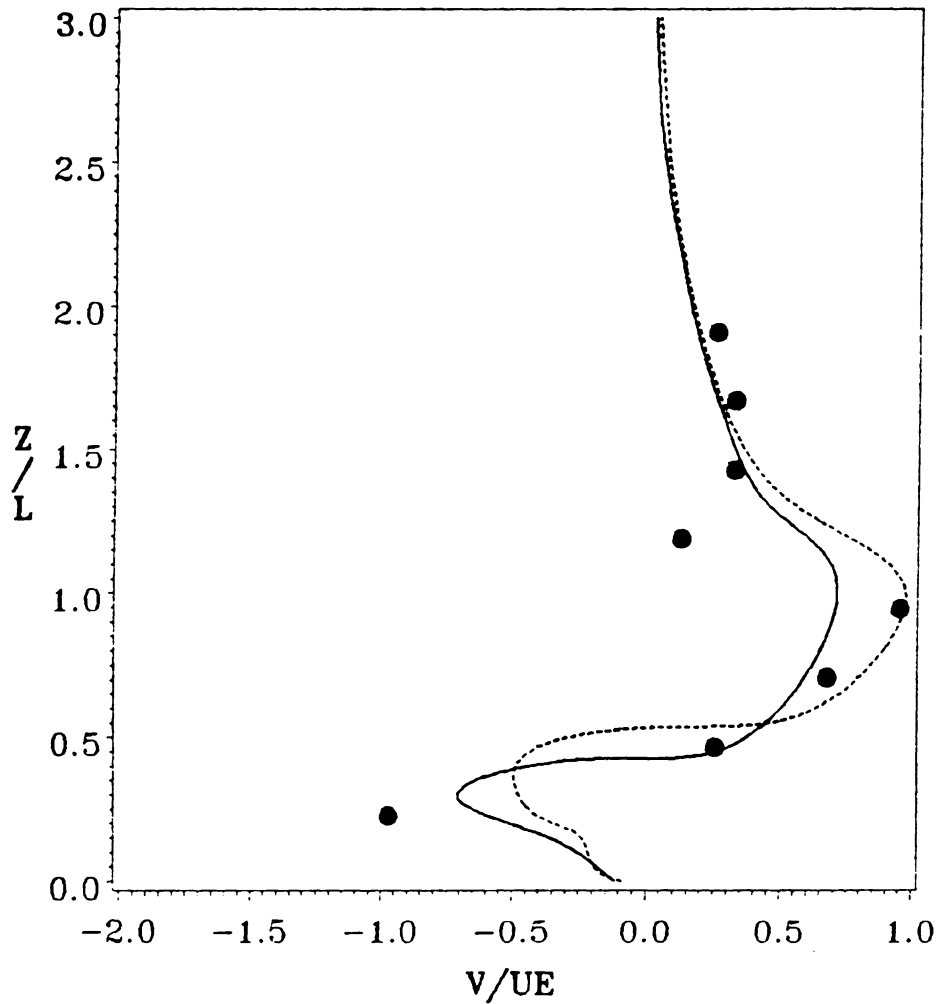


Figure 69. Dual Rectangular Jets in a Crossflow at $R=4$: Comparison of Transverse Velocity Profiles at $x/D=0.0$ and $y/D=0.25$: circle - measured data [80], broken line - coarse mesh, solid line - fine mesh

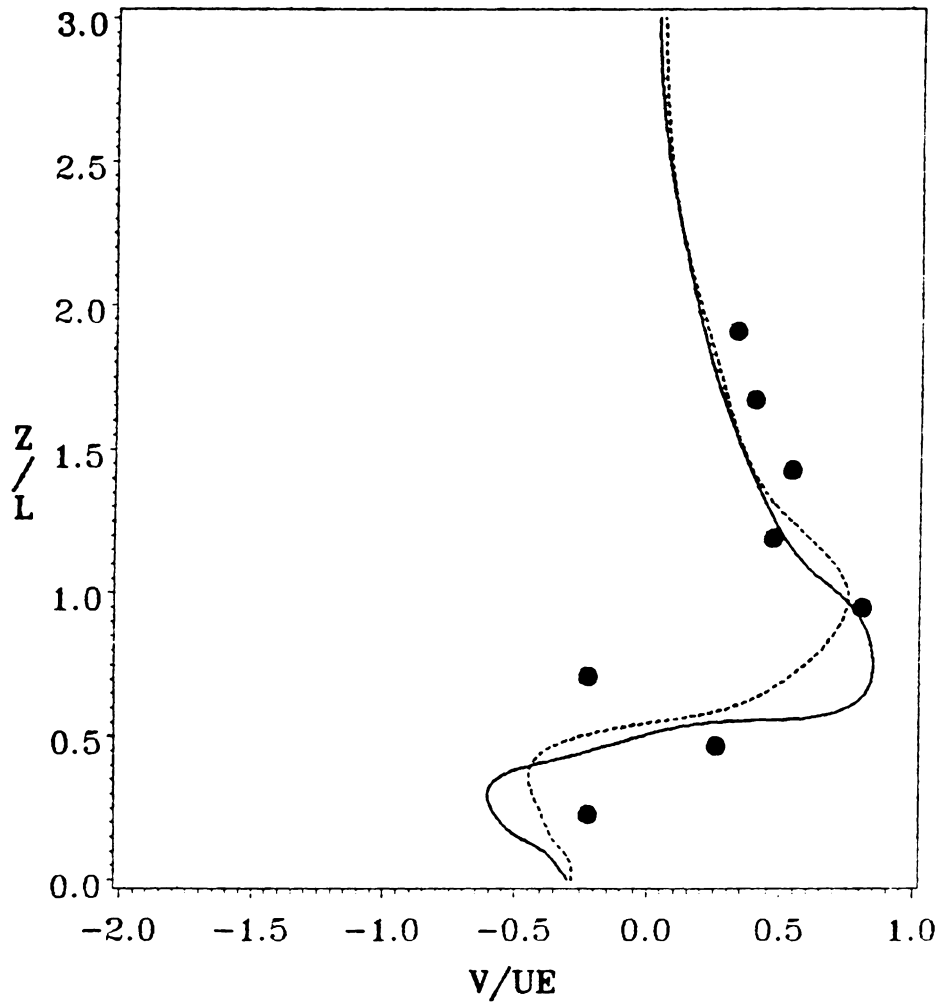


Figure 70. Dual Rectangular Jets in a Crossflow at $R=4$: Comparison of Transverse Velocity Profiles at $x/D=0.0$ and $y/D=0.5$: circle - measured data [80], broken line - coarse mesh, solid line - fine mesh

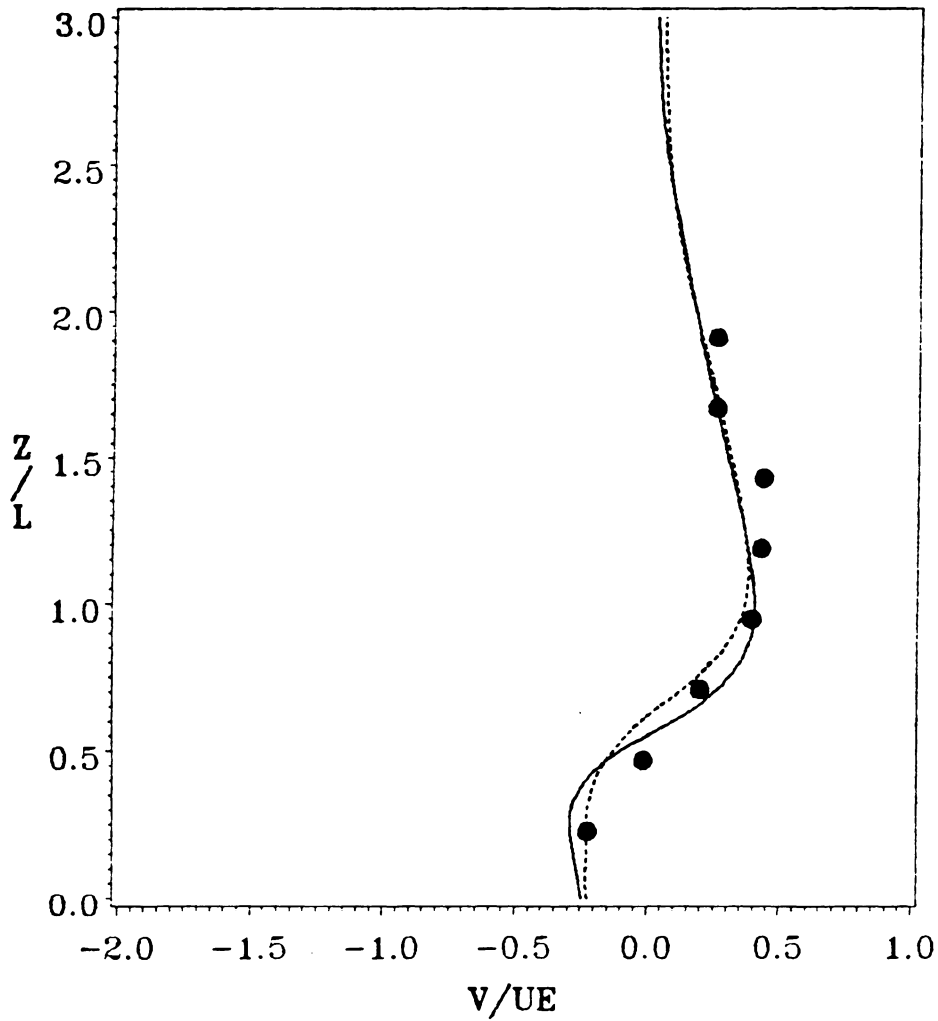


Figure 71. Dual Rectangular Jets in a Crossflow at $R=4$: Comparison of Transverse Velocity Profiles at $x/D=0.0$ and $y/D=0.75$: circle - measured data [80], broken line - coarse mesh, solid line - fine mesh

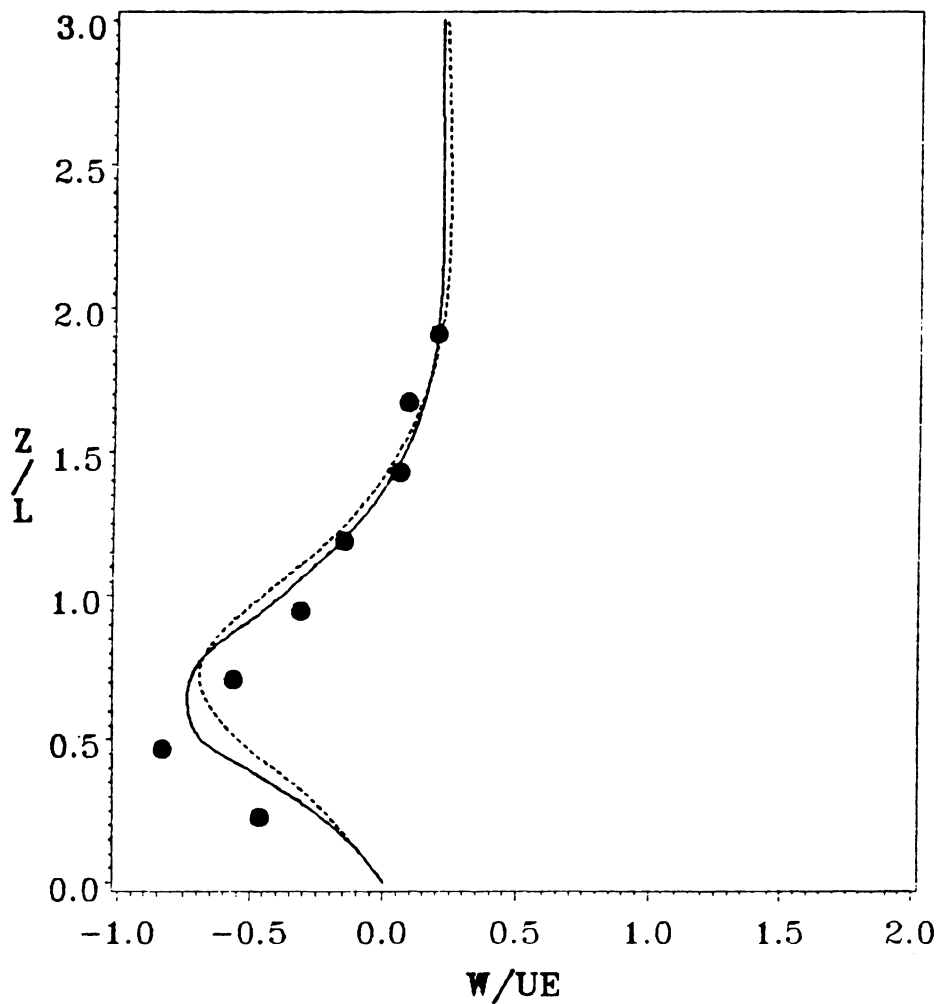


Figure 72. Dual Rectangular Jets in a Crossflow at $R = 4$: Comparison of Normal Velocity Profiles at $x/D = 0.0$ and $y/D = -0.75$: circle - measured data [80], broken line - coarse mesh, solid line - fine mesh

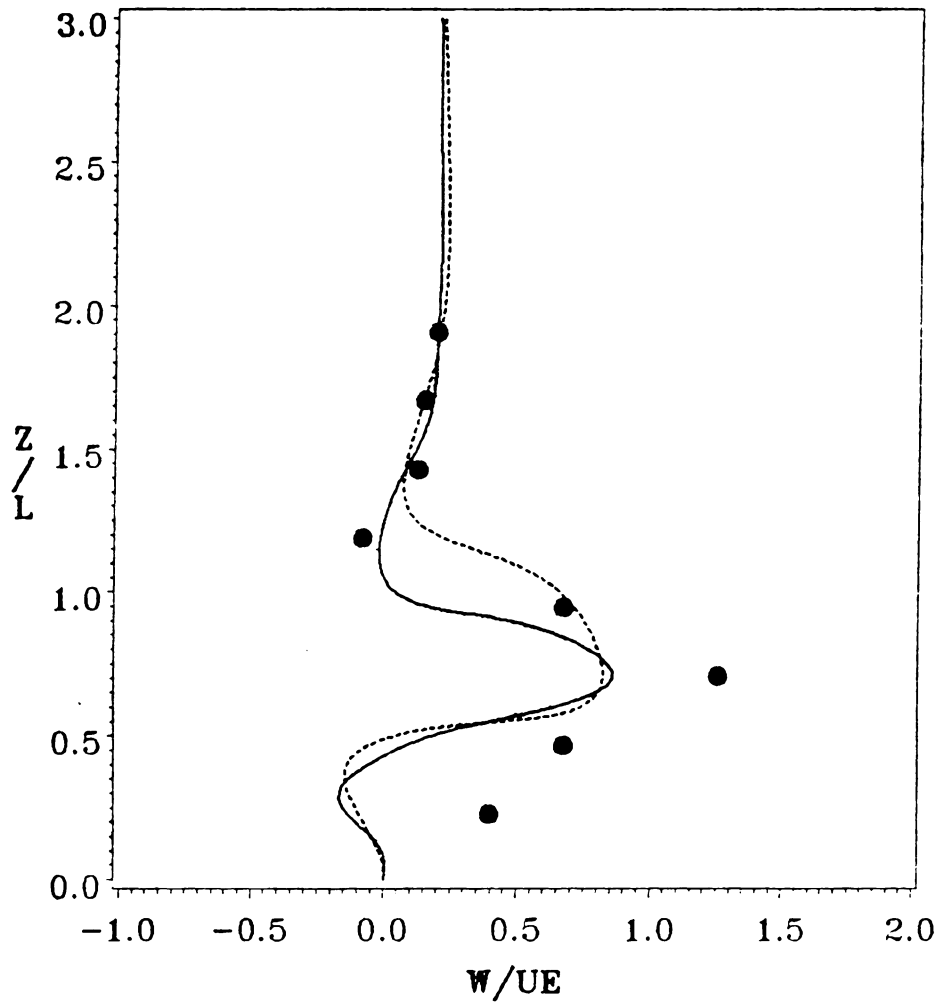


Figure 73. Dual Rectangular Jets in a Crossflow at $R=4$: Comparison of Normal Velocity Profiles at $x/D=0.0$ and $y/D=-0.5$: circle - measured data [80], broken line - coarse mesh, solid line - fine mesh

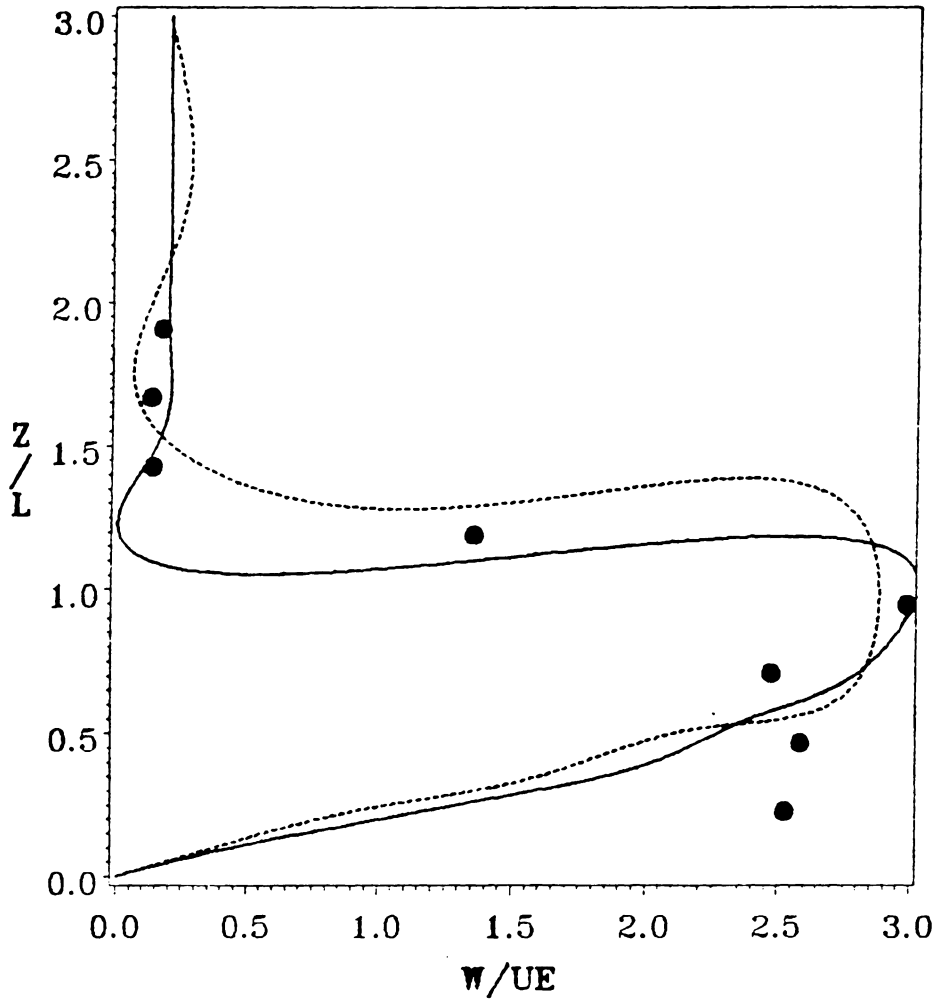


Figure 74. Dual Rectangular Jets in a Crossflow at $R=4$: Comparison of Normal Velocity Profiles at $x/D=0.0$ and $y/D=-0.25$: circle - measured data [80], broken line - coarse mesh, solid line - fine mesh

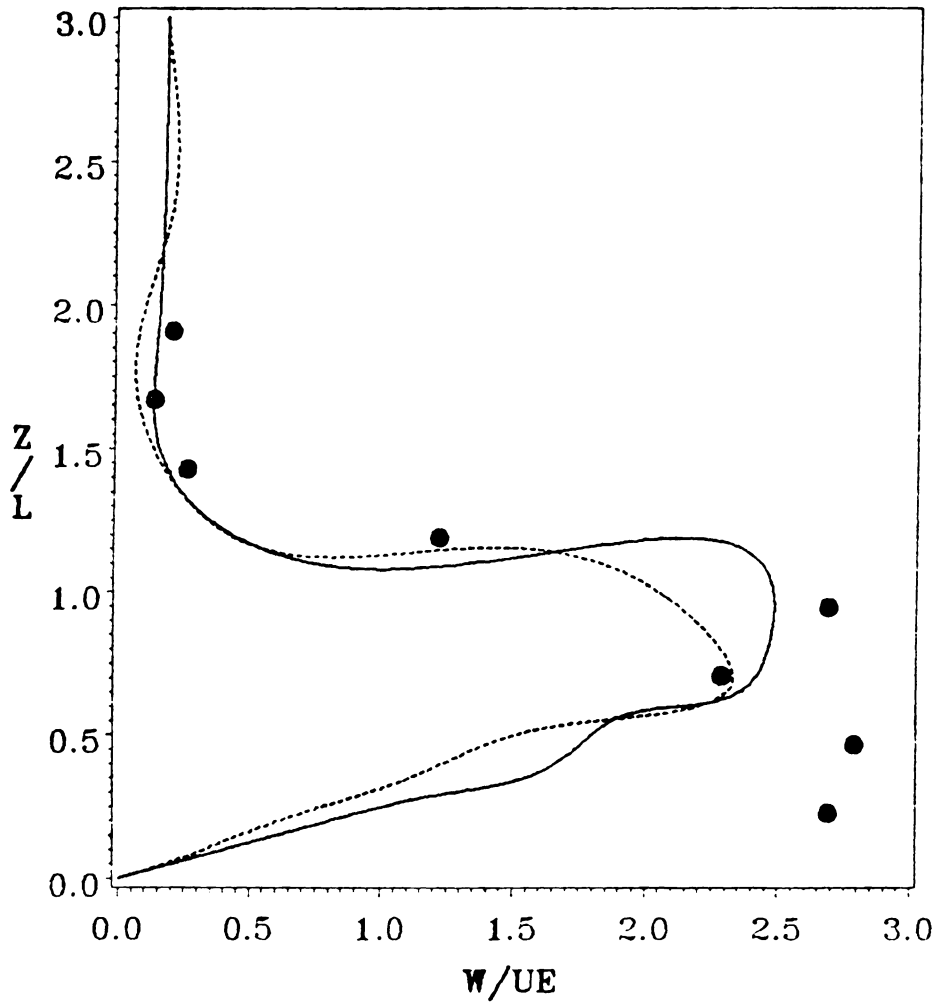


Figure 75. Dual Rectangular Jets in a Crossflow at $R=4$: Comparison of Normal Velocity Profiles at $x/D=0.0$ and $y/D=0.25$: circle - measured data [80], broken line - coarse mesh, solid line - fine mesh

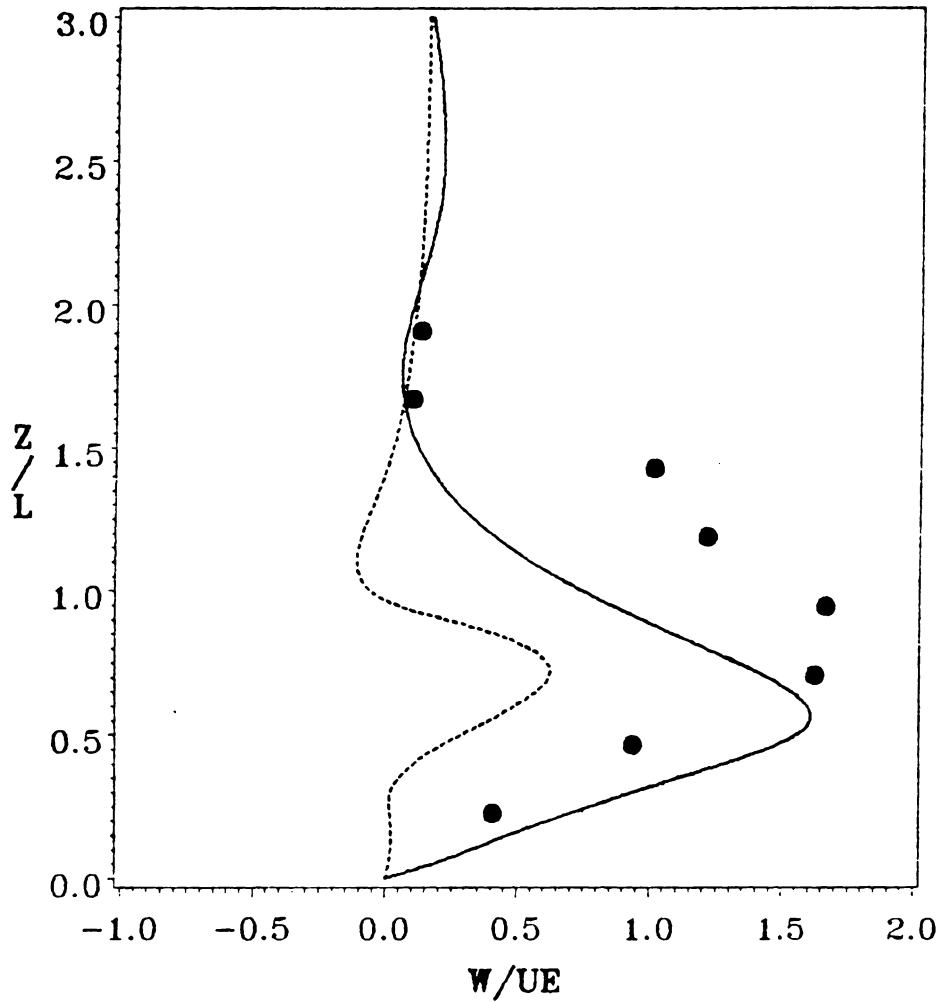


Figure 76. Dual Rectangular Jets in a Crossflow at $R=4$: Comparison of Normal Velocity Profiles at $x/D=0.0$ and $y/D=0.5$: circle - measured data [80], broken line - coarse mesh, solid line - fine mesh

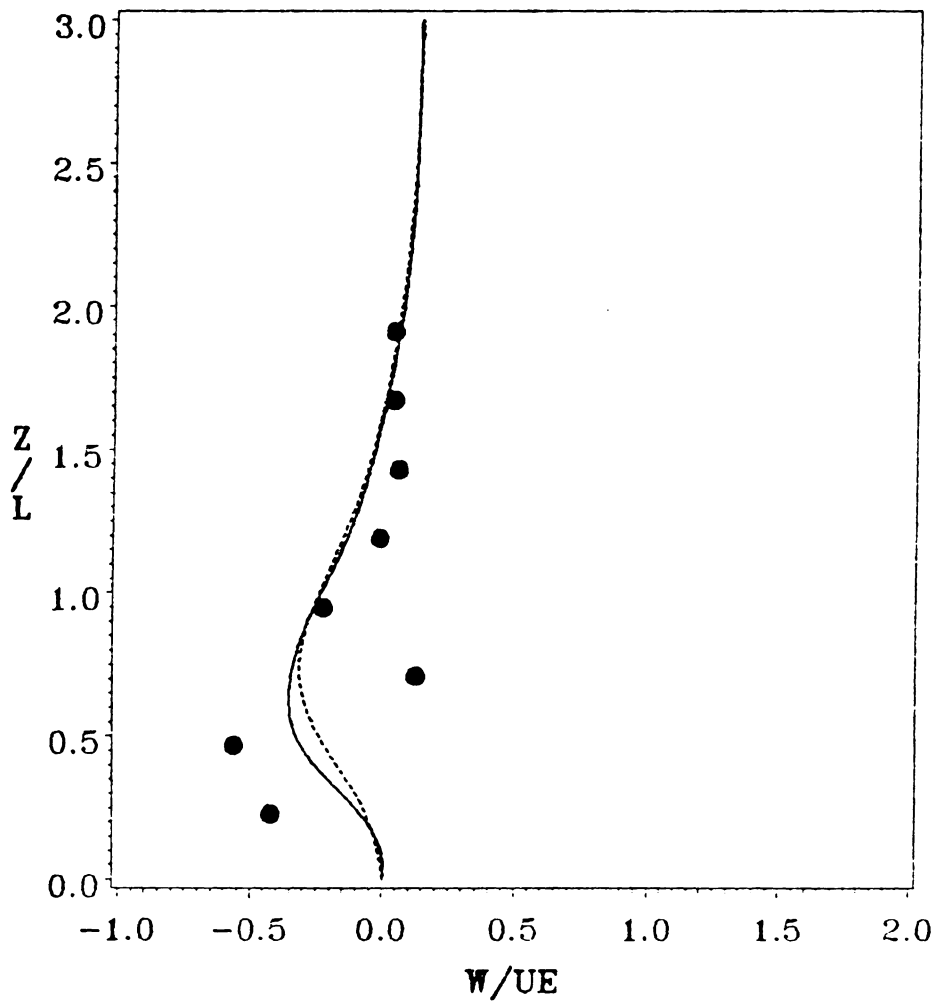


Figure 77. Dual Rectangular Jets in a Crossflow at $R=4$: Comparison of Normal Velocity Profiles at $x/D=0.0$ and $y/D=0.75$: circle - measured data [80], broken line - coarse mesh, solid line - fine mesh

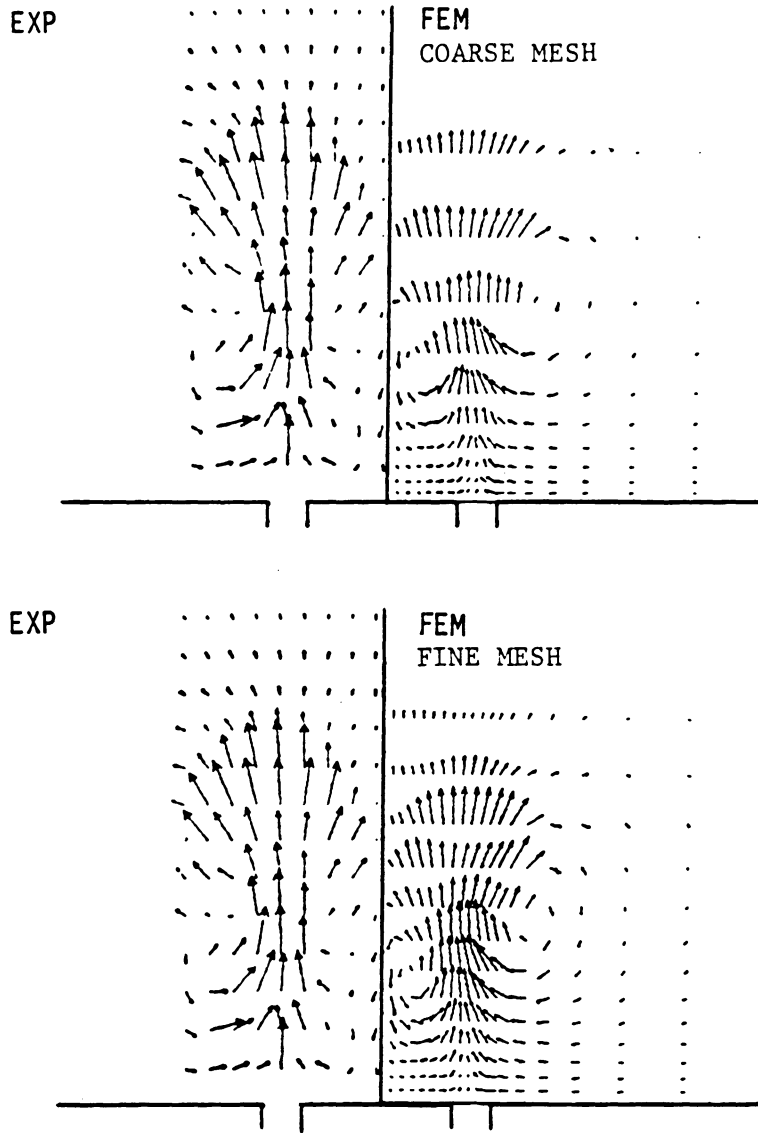


Figure 78. Dual Rectangular Jets in a Crossflow at $R = 4$: Comparison of Velocity Vector Plots on the Crossflow Plane ($x/D = 1.0$)

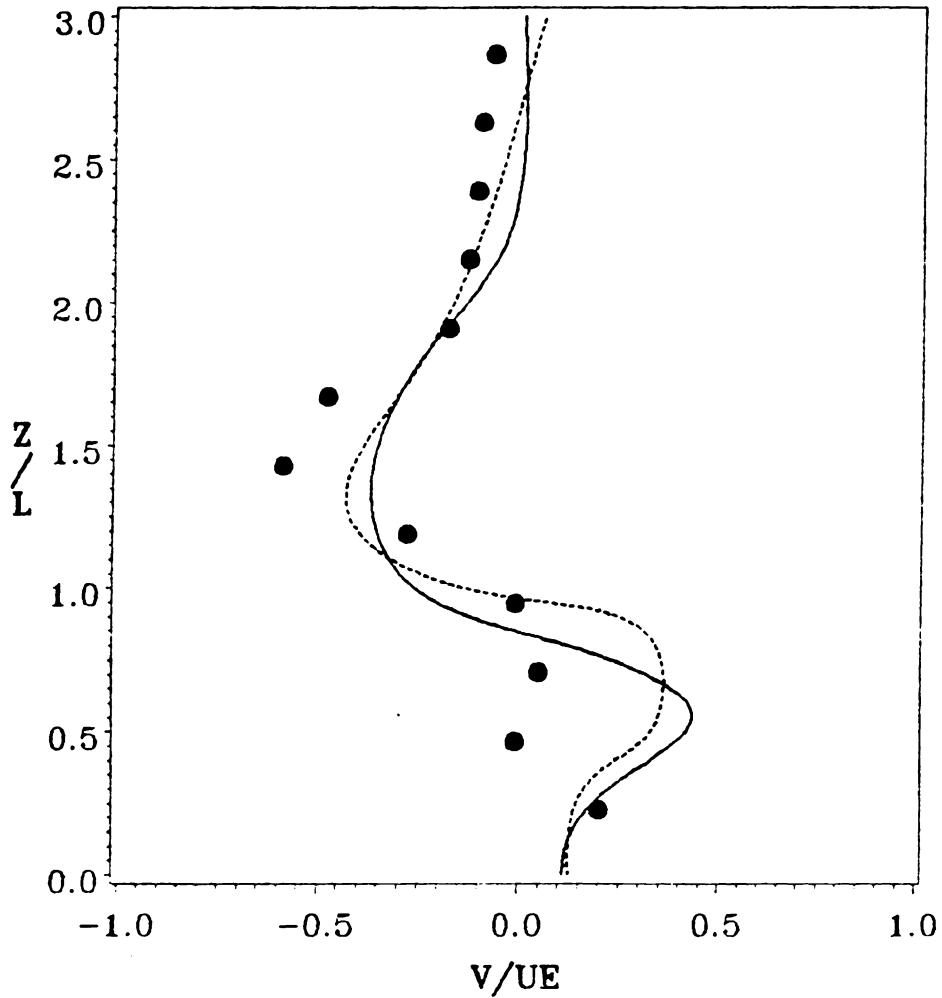


Figure 79. Dual Rectangular Jets in a Crossflow at $R=4$: Comparison of Transverse Velocity Profiles at $x/D=1.0$ and $y/D=-0.75$: circle - measured data [80], broken line - coarse mesh, solid line - fine mesh

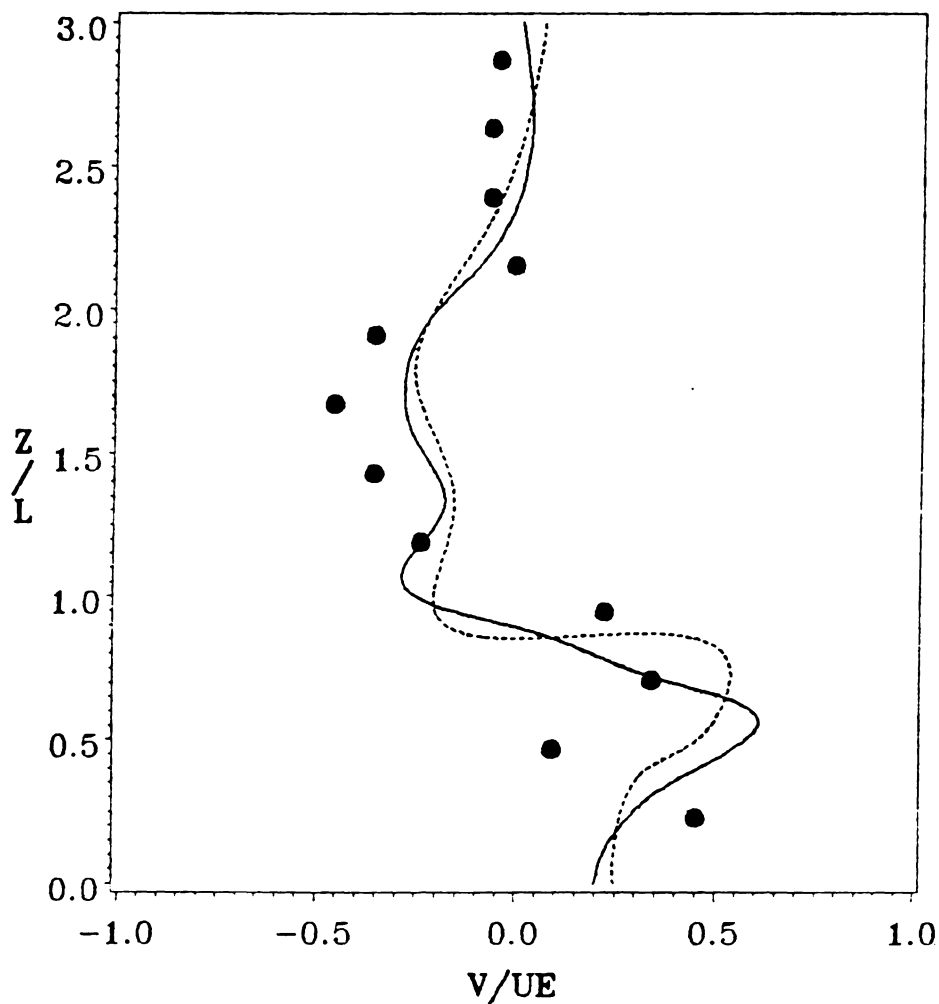


Figure 80. Dual Rectangular Jets in a Crossflow at $R=4$: Comparison of Transverse Velocity Profiles at $x/D=1.0$ and $y/D=-0.5$: circle - measured data [80], broken line - coarse mesh, solid line - fine mesh

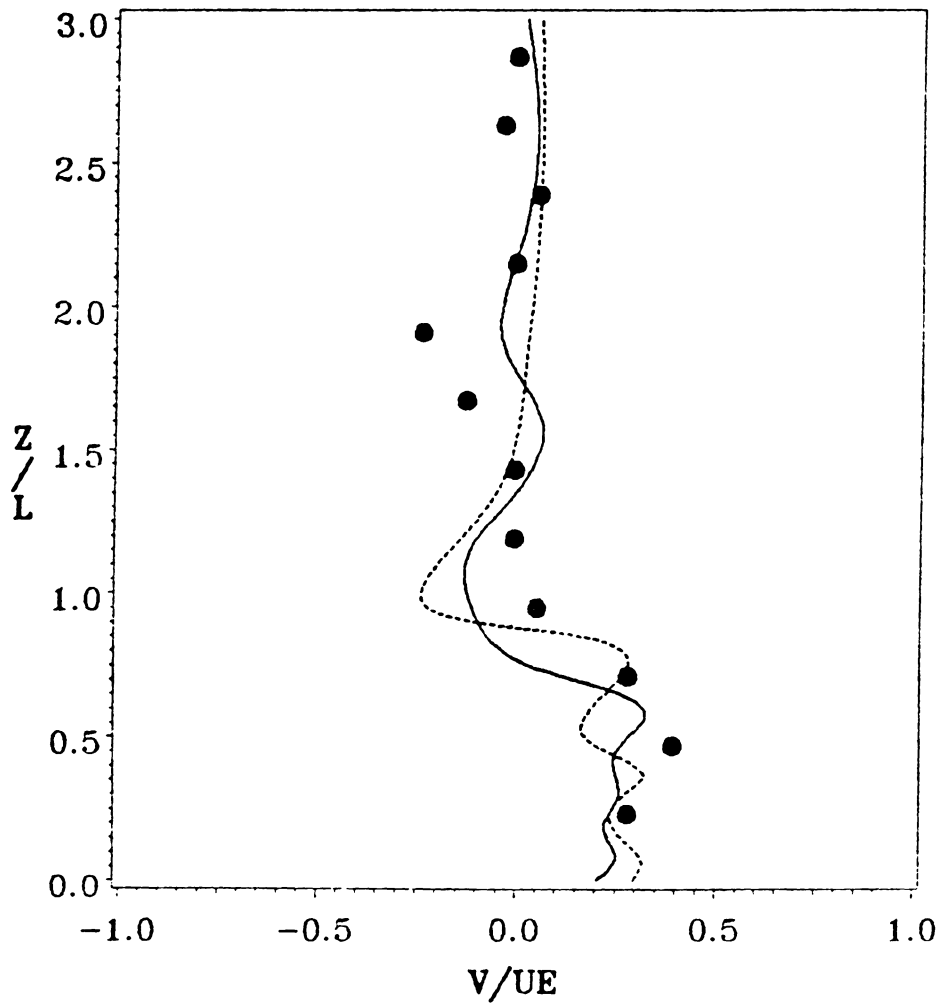


Figure 81. Dual Rectangular Jets in a Crossflow at $R=4$: Comparison of Transverse Velocity Profiles at $x/D=1.0$ and $y/D=-0.25$: circle - measured data [80], broken line - coarse mesh, solid line - fine mesh

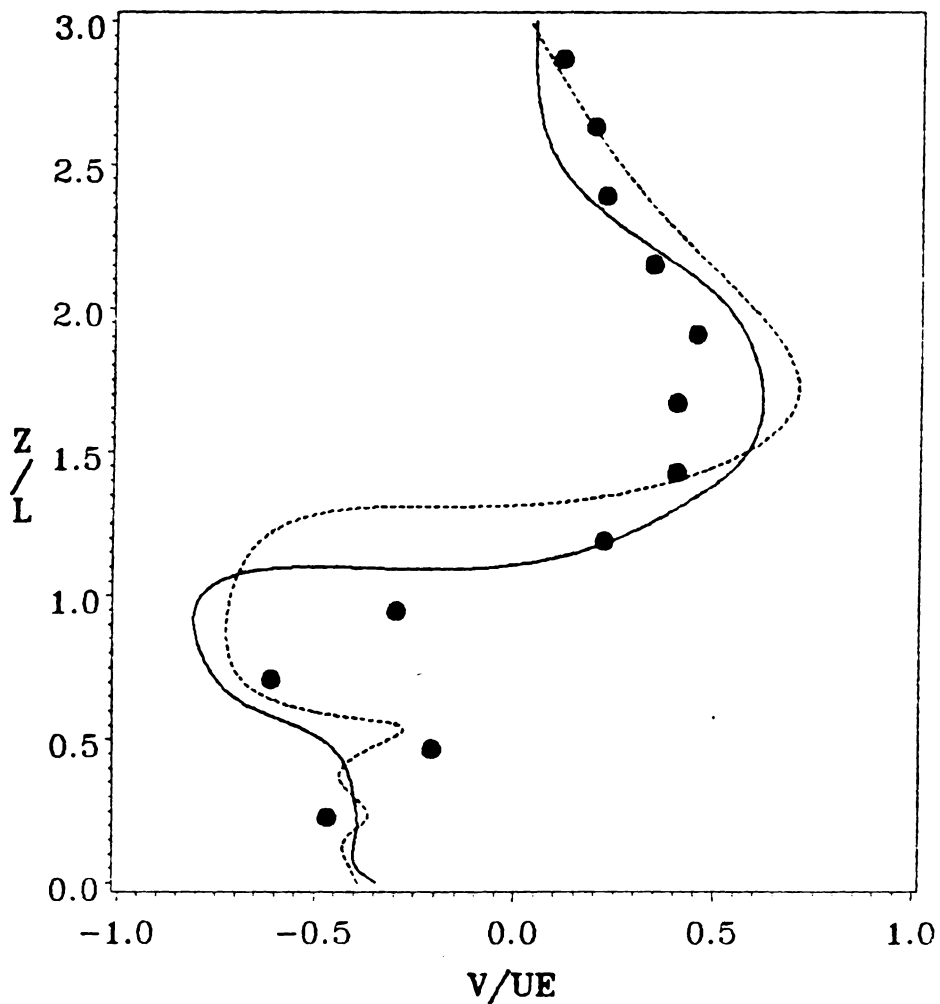


Figure 82. Dual Rectangular Jets in a Crossflow at $R=4$: Comparison of Transverse Velocity Profiles at $x/D=1.0$ and $y/D=0.25$: circle - measured data [80], broken line - coarse mesh, solid line - fine mesh

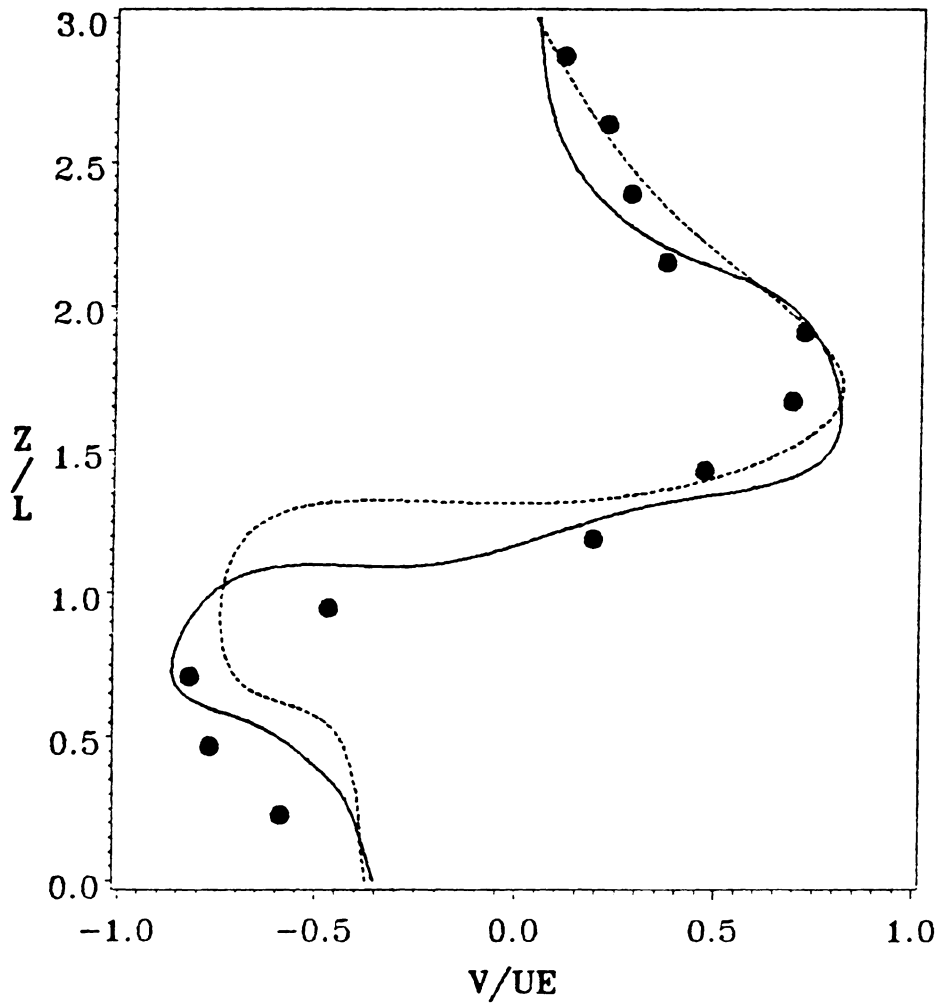


Figure 83. Dual Rectangular Jets in a Crossflow at $R=4$: Comparison of Transverse Velocity Profiles at $x/D=1.0$ and $y/D=0.5$: circle - measured data [80], broken line - coarse mesh, solid line - fine mesh

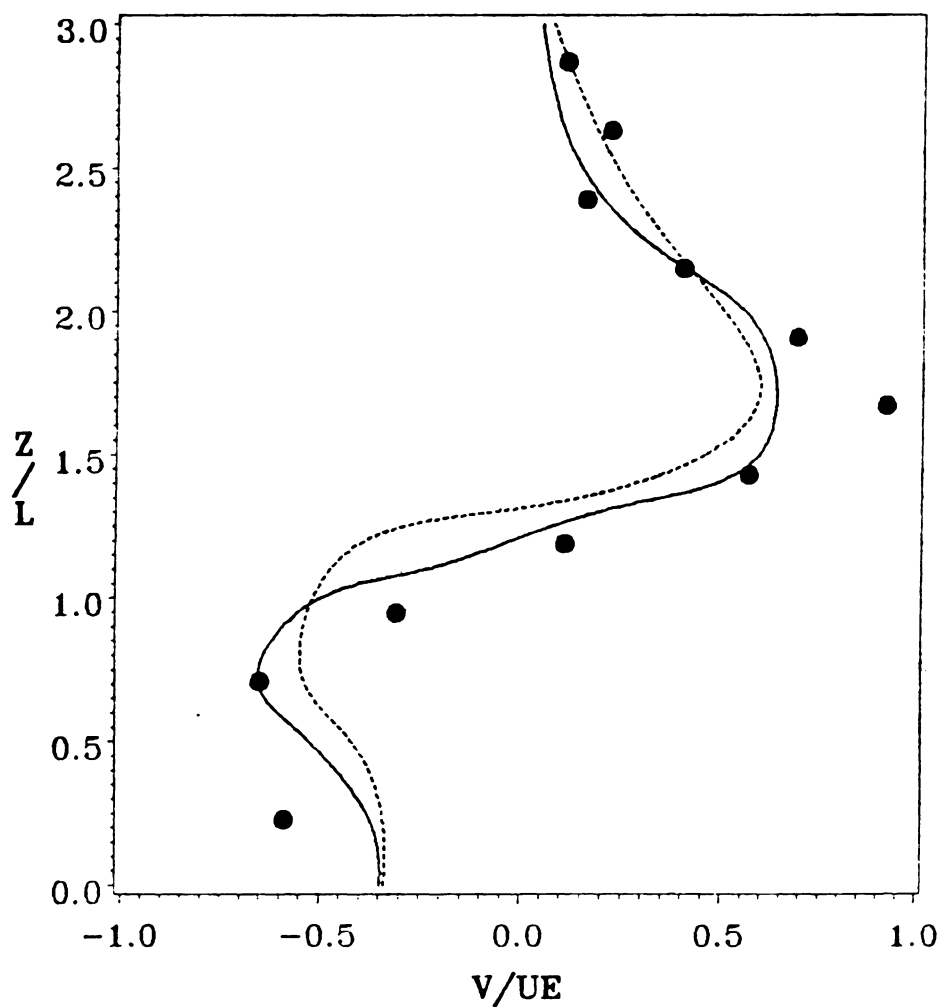


Figure 84. Dual Rectangular Jets in a Crossflow at $R=4$: Comparison of Transverse Velocity Profiles at $x/D=1.0$ and $y/D=0.75$: circle - measured data [80], broken line - coarse mesh, solid line - fine mesh

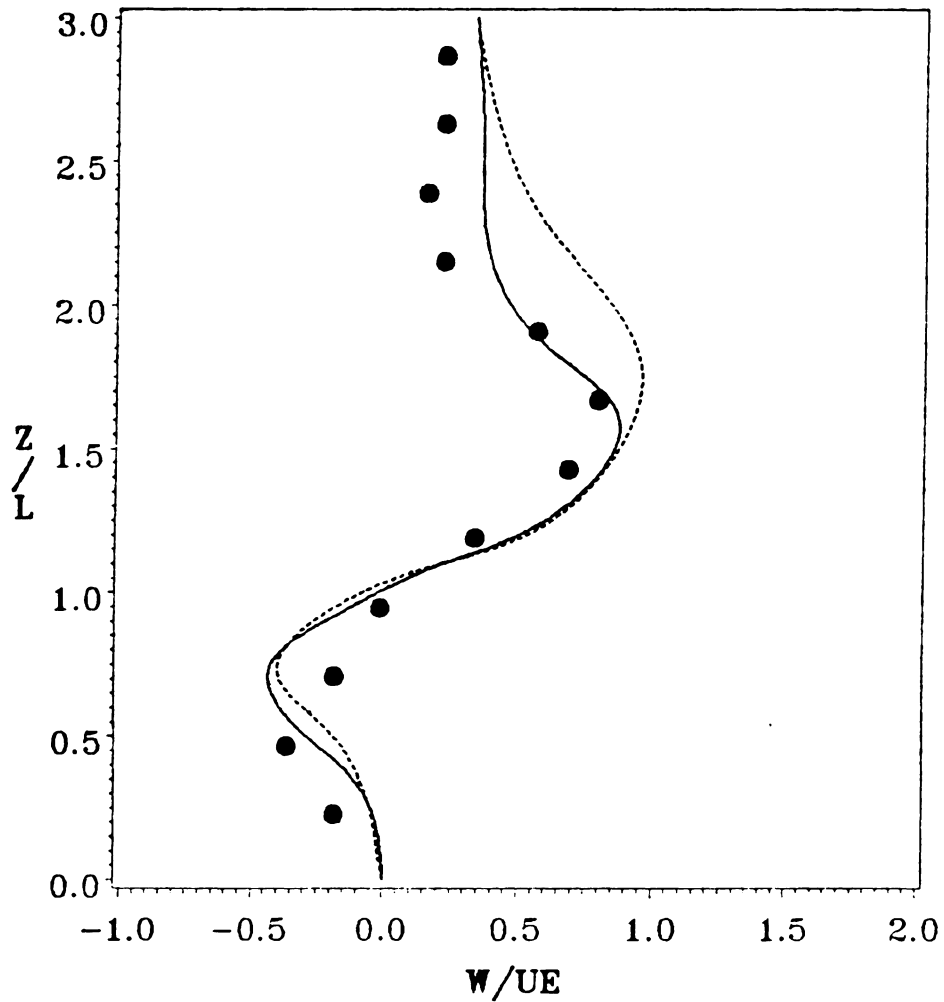


Figure 85. Dual Rectangular Jets in a Crossflow at $R=4$: Comparison of Normal Velocity Profiles at $x/D=1.0$ and $y/D=-0.75$: circle - measured data [80], broken line - coarse mesh, solid line - fine mesh

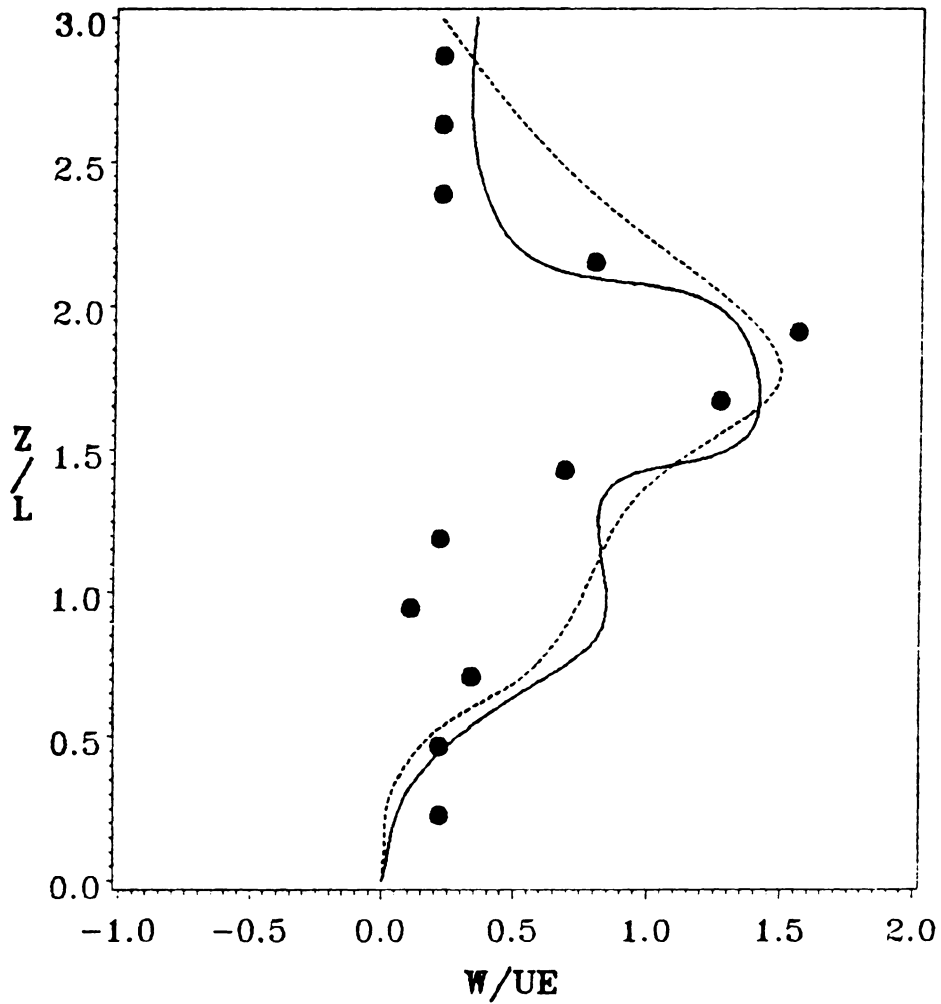


Figure 86. Dual Rectangular Jets in a Crossflow at $R=4$: Comparison of Normal Velocity Profiles at $x/D=1.0$ and $y/D=-0.5$: circle - measured data [80], broken line - coarse mesh, solid line - fine mesh

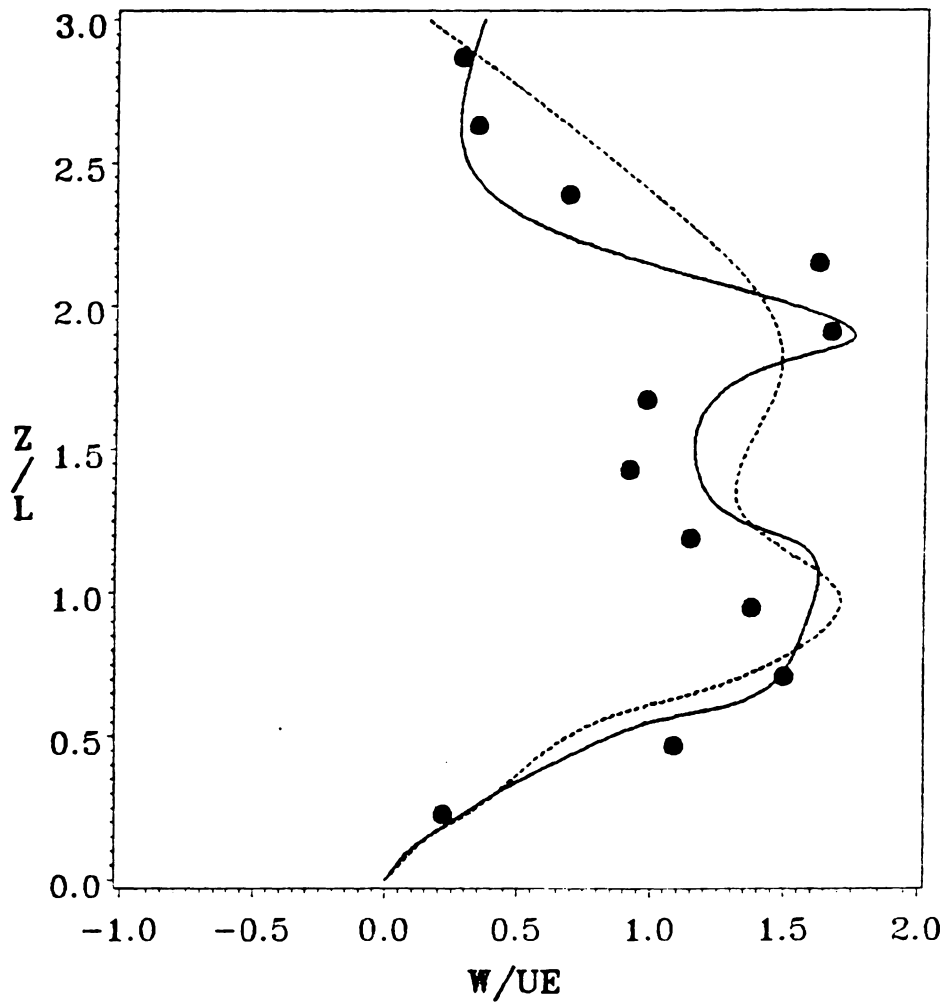


Figure 87. Dual Rectangular Jets in a Crossflow at $R = 4$: Comparison of Normal Velocity Profiles at $x/D = 1.0$ and $y/D = -0.25$: circle - measured data [80], broken line - coarse mesh, solid line - fine mesh

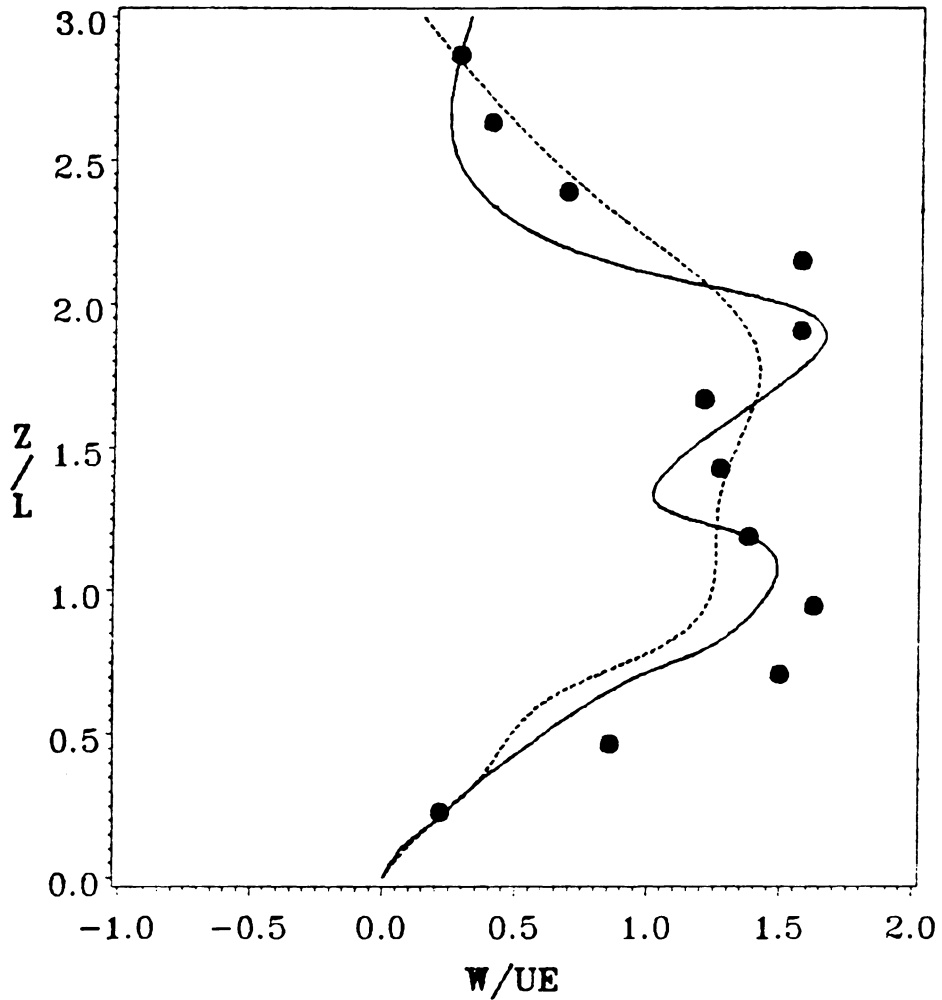


Figure 88. Dual Rectangular Jets in a Crossflow at $R=4$: Comparison of Normal Velocity Profiles at $x/D=1.0$ and $y/D=0.25$: circle - measured data [80], broken line - coarse mesh, solid line - fine mesh

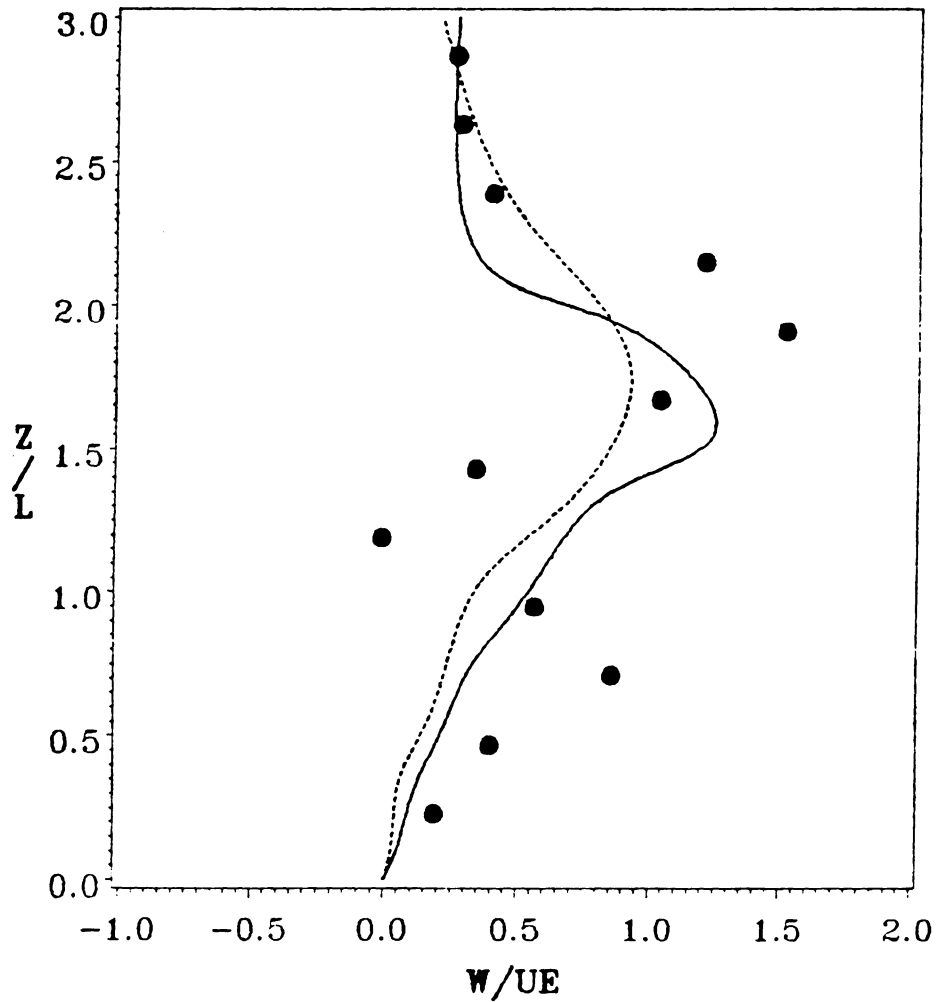


Figure 89. Dual Rectangular Jets in a Crossflow at $R=4$: Comparison of Normal Velocity Profiles at $x/D=1.0$ and $y/D=0.5$: circle - measured data [80], broken line - coarse mesh, solid line - fine mesh

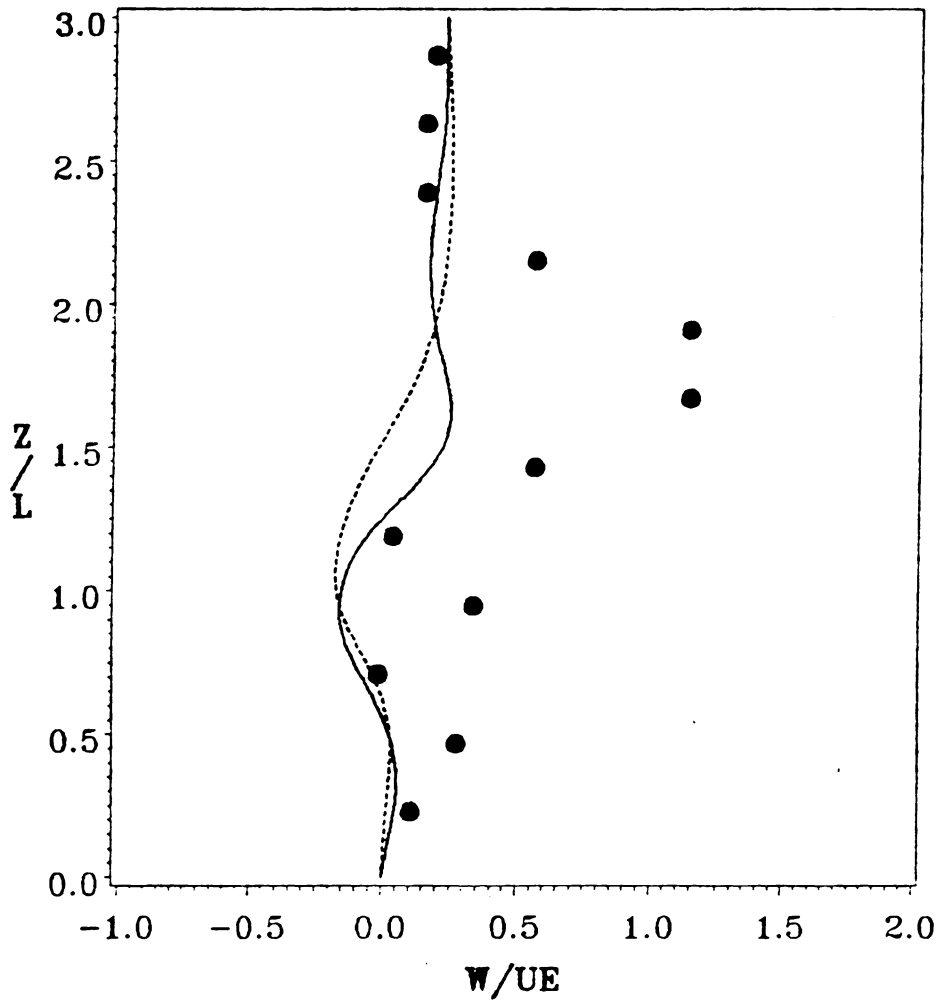


Figure 90. Dual Rectangular Jets in a Crossflow at $R=4$: Comparison of Normal Velocity Profiles at $x/D=1.0$ and $y/D=0.75$: circle - measured data [80], broken line - coarse mesh, solid line - fine mesh

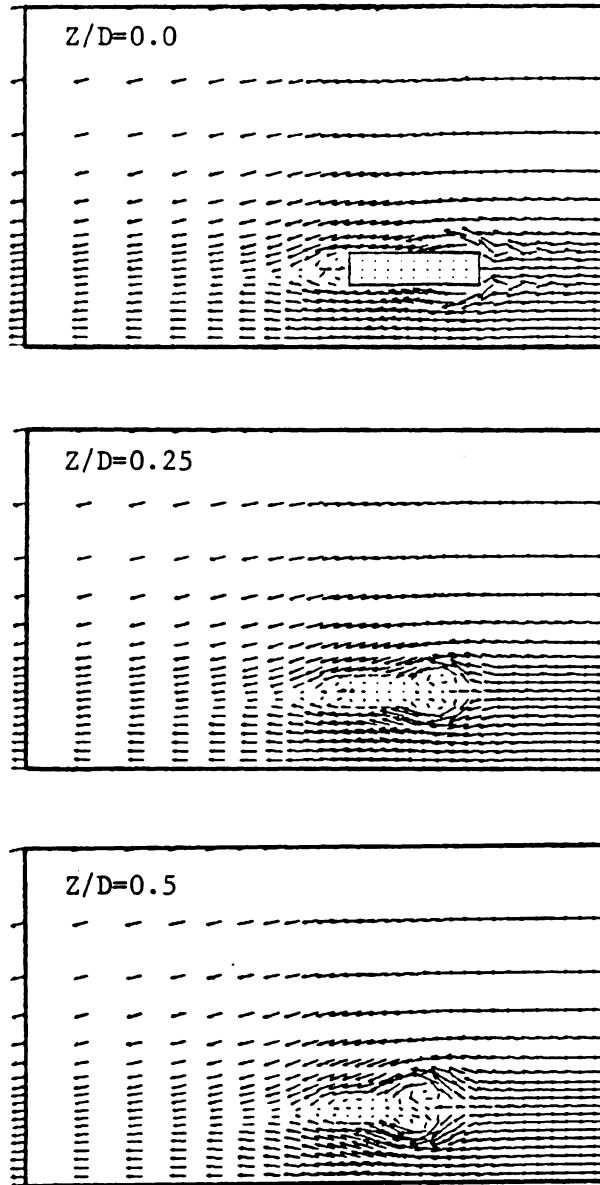


Figure 91. Dual Rectangular Jets in a Crossflow at $R=4$: Display of Velocity Vectors on the Plane $z/D=0.0, 0.25, 0.5$ from above

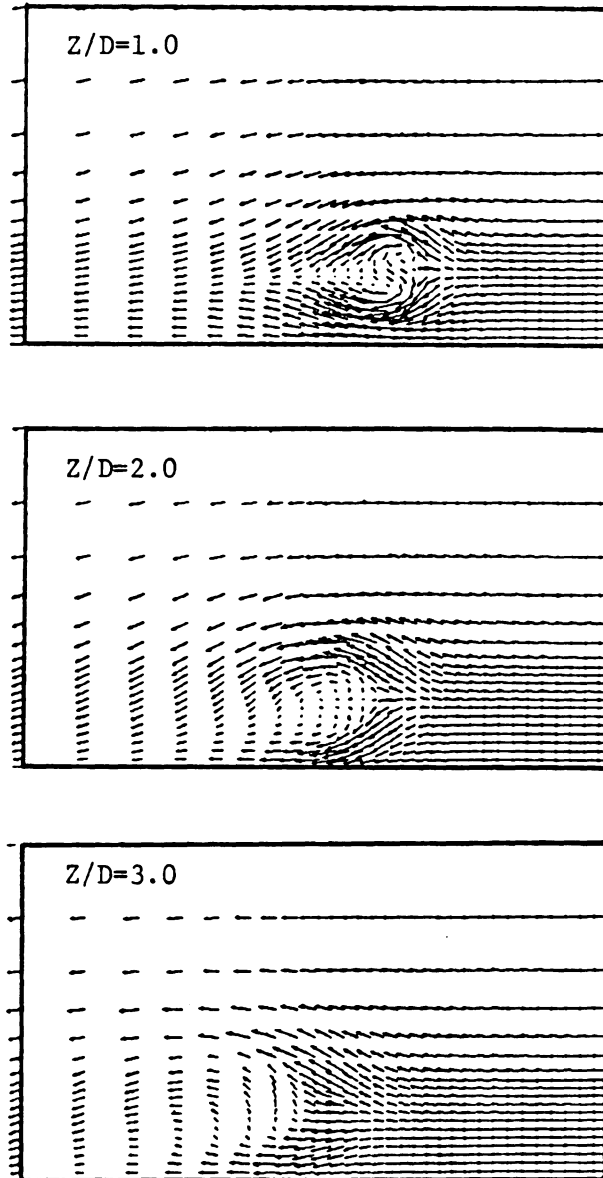


Figure 92. Dual Rectangular Jets in a Crossflow at $R=4$: Display of Velocity Vectors on the Plane $z/D=1.0, 2.0, 3.0$ from above

**The vita has been removed from
the scanned document**